Dielectric elastomer actuation performance enhancement, higher order modelling and self-sensing control

Zhang, Runan

Award date:
2017

Awarding institution:
University of Bath

Dielectric elastomer actuation performance enhancement, higher order modelling and self-sensing control

submitted by

Runan Zhang

for the degree of Doctor of Philosophy

of the

University of Bath

Department of Mechanical Engineering

October 2017

Abstract

There is a growing interest in the field of Dielectric Elastomer Actuators (DEAs). A DEA consists of a thin DE film coated with a compliant electrode. It expands in planar directions and contracts in thickness under a driving voltage. Because of the similar actuation capability compared with human muscles, it is often referred as artificial muscle. One possible application is to integrate the DEA in wearable devices for tremor suppression. In this thesis, the development of the DEA has been advanced towards this application in three aspects: performance enhancement, modelling accuracy and self-sensing control.

The results presented demonstrate that the combination of pre-strain and motion constraining enhances the force output of the DEA significantly but it also leads to the pre-mature electric breakdown that shortens the operational life. This drawback was suppressed by optimising the electrode configuration to avoid the electrically weak regions with low thickness across the DE film, together with the lead contact off the active electrode region. The durability of the enhanced DEA was therefore improved significantly.

Polyacrylate, a commonly used DE, was characterised for dynamic mechanical loading and electrical actuation. The conventional Kelvin-Voigt model was proved to be deficient in simulating the viscoelastic behaviour of polyacrylate in the frequency domain. The error in modelling was substantially reduced using a higher material model that contains multiple spring-damper combinations. It allows the system dynamics to be shaped over frequency ranges. A detailed procedure was given to guide the parameter identification in higher order material model.

A novel self-sensing mechanism that does not require superposition of driving voltage and excitation signal was also designed. It reconfigures the conventional DEA to have separate electrode regions for sensing and actuating. As the DE film deforms under driving voltage, the capacitive change in the electrode region for sensing was measured via a capacitor bridge and used as the feedback for actuation control. The self-sensing DEA can, therefore, be implemented with any high voltage power supply. Moreover, the sensing performance is demonstrated to have improved consistency without interference of the electrical field. It also has a unique feature of DE film wrinkling detection.

Acknowledgements

This work was supported by a GRS (Global Research Scholarship) from the University of Bath, UK and the research collaboration funding from the Open Foundation of the State Key Laboratory of Fluid Power Transmission and Control, Zhejiang University, China.

I am grateful for the support, enthusiasm and advice of my supervisors, Prof. Patrick Keogh and Dr. Pejman Iravani, for the inspiration from my former supervisors, Prof. Necip Sahinkaya and Dr. Matthew Cole, for the help of technicians, Gary Barter, Clare Ball and instrumentation specialists, Vijay Rajput, and John Bishop.

Lastly and most importantly, I would like to thank my beautiful and loving wife, Yan, for her unending support and distraction. Although the Ph.D. might have been quicker without her, it would certainly not have been as enjoyable.

Table of contents

List of Figures

List of Tables

Chapter 1

Introduction

This chapter elaborates the underlying motivation of this Ph.D. thesis. A brief introduction is given to involuntary movements in the human body, how it brings inconvenience to a patient's daily life. The effective treatment that has yet to be developed includes existing wearable devices, which could be used to regulate human motion. Soft actuation technologies, which address the limits of existing wearable devices, could be a solution for involuntary human movements. The DE actuation, which suits such application, is compared with other soft actuation technologies.

1.1 Involuntary movements in human body

Essential tremor (ET) is a common cause of significant disability. The "classic ET" is defined as a monosymptomatic disorder with bilateral, largely symmetric postural or kinetic tremor involving the hands and forearms that is visible and persistent. Isolated head tremor in the absence of dystonic posturing is another example [1]. Evidence also suggests that the phenotype of ET also includes subtle cerebellar abnormalities [2], cognitive dysfunction [3], hearing abnormalities [4], and dystonia [5]. It affects approximately 1% of the general population and 5% of the population over 65 years of age [6]. Though it is not life threatening, ET impacts heavily on a patient's daily life.

Despite this high prevalence, the understanding of ET is limited and ET research is hindered mainly due to the lack of stringent diagnostic criteria and the lack of biomarkers. ET shares similar phenotypes with Parkinson's disease (PD), dystonia and other disorders [7]. It brings diagnostic uncertainty regardless of how ET is defined. As a result, the clinical definition of ET has been inconsistent; the pathological findings have been debated; the underlying genes have been elusive; the mechanisms of neural network oscillation are unknown and no satisfactory pharmacological treatment exists.

There are several surgical treatments for ET, including thalamic deep brain stimulation, and thalamotomy via surgical or magnetic resonance guided focused ultrasound lesioning [8]. While these treatments are found to be effective, the cost is ineffective for curing the the less severe type of ET. In addition, interest has also grown in the use of portable motion transducers to objectively measure tremor amplitude. However, the sensitivity and precision of these sensors (e.g., accelerometers, gyroscopes and digitizing tablets) are limited by the large random variability in tremor amplitude [9]. Moreover, the capability of making the measurement continuously and autonomously throughout the day without requiring the presence of clinicians has yet to be achieved.

1.2 Existing wearable devices

In order to regulate such involuntary movements in the human body, novel active wearable technologies can provide accurate long-term tremor monitoring and effective motion regulation. They are still to be developed and validated. Existing active wearable devices fall into two categories, exoskeleton and smart prosthetic.

While typical powered prosthetics (e.g., Genium, Dynamic Arm, C leg and Helix 3D [10]) have been designed to replace missing limbs with different function modes, exoskeletons are commonly developed to assist humans to achieve enhanced motion and strength. Honda has developed "The Stride Management Assist System" to ease long-distance walking with improved speed [11]. It is worn with a belt around the thighs and the hips, the motors on both sides lift legs at the thighs to move forward and backward. XOS [12] and HULC [13]

are more advanced exoskeletons that enhance wider range of human motions for military use. The structures cover the entire human body in order to provide protection and boost lifting power. Portable powered ankle- foot orthoses (PPAFOs) [14] were developed to provide rehabilitation treatment to patients with ankle injuries. The typical structure of PPAFOs contains two frames which are worn on the lower limb and foot, and a motor with processor to control the relative motion between the two frames. The device generates force to constrain the movement of the ankle joint, thus helping to restore the gait cycle.

As being indicated in the name, the exoskeleton devices are "rigid" structures for power, transmission and control. Moreover, for achieving complex motions, because these devices are powered by linear actuators, they add additional complexity into the structure, weight and increase the size. The rigidity and relatively large size (compared with human body) of the structure makes them less friendly for users in the long-term throughout daily life. It is clear that an active wearable device must be more compliant for use in clothing and gloves. The actuation must be dexterous, soft, light and energy-efficient. The next section reasons the choice of the soft actuator as a dielectric elastomer actuator (DEA) for as the motivation for this research.

1.3 Artificial muscle actuators

Artificial muscles are biologically inspired linear actuators. Their design aims to share many of the features of human muscles such as the working principle, noise-free operation, lightness, high power to weight ratio, and the compliance. For a typical postural tremor of the hands, the motion is bilateral and has an amplitude up to 0.1 cm and frequency up to 10 Hz [15]. Hence in order to effectively suppress the tremor, the qualified soft actuator should be capable of providing the actuation forces up to 0.4 N and with a stroke no less than 1 mm. Furthermore, the development of such active wearable devices requires simplicity of the structure of the actuator to facilitate the combination of actuators for achieving complex and versatile motions. This section evaluates the three types of muscle-like actuation technologies that have been developed: McKibbon pneumatic actuators (PAM),

Shape Memory Alloy (SMA) actuators and Electro-Active Polymer Actuators (EAP).

McKibbon actuators (PAMs) work by pumping the air into the bladder wrapped under a mesh web. The bulging of the bladder produces contractive force in the axial direction to provide the actuation. The biggest feature of these actuators derives from the compliance as using compressible air for actuation, the light weight (typically around 100 g due to the use of a membrane) as well as high power to weight ratios up to 5 kW/kg [16]. The PAM is believed to be a suitable compliant power system for both mobile robotics and prosthetics, and it has been commercialized in robotics by Bridgestone Co. and Festo Ag. & Co. Although this technology was firstly developed in the 1950s, it has never been used widely to date. The main drawbacks of PAMs are the difficulty of achieving accurate position control due to their nonlinearity. They also have a relatively short service life since the combination of a flexible membrane and rigid ends in the structure leads to stress concentration. In addition, the noise associated with valve switching can be another issue as well as the inevitably frequent maintenance of sealing and all other components to prevent leakage. Finally, the multi-step actuation of PAM can lead to significant time delay in the actuation response.

SMAs change phase when subject to heat. The most commonly used material is a Nickel Titanium alloy. The SMA actuator is able to generate constant force and can undergo strains up to 10%. However, they suffer from fatigue significantly, especially when at maximum force capacities. The low bandwidth frequency response of approximately 1 Hz is another drawback.

Electro-Active Polymers (EAPs) generate expansion in a lateral direction and contraction in an axial direction of the electric field when subject to large voltage, in a similar way to piezoelectric actuators. The actuators consist of 2 layers of compliant electrodes with a thin sheet of EAP in the middle as a sandwich structure. There are two common types of EAPs, ionic EAPs which utilize ionic movement to generate the motion, and dielectric EAPs, namely Dielectric Elastomer Actuators (DEAs), which use Maxwell pressure and act as deformable capacitors. The latter have been developed and researched since the early 1990s. The common strain in DE actuation is between 5% and 15% with low correlated

forces around 1 N. The DEs commonly have time-dependent, strain-dependent and rate-dependent mechanical behaviour due to viscoelastic nature of the dielectric polymers [17]. The feasible frequency bandwidth of DE actuation is typically up to 10 Hz, which coincides with the specification for tremor suppression.

All these technologies have strengths and weakness. McKibbon Pneumatic Actuators are able of generating both high force and large range of motion, but require external components. SMA actuators generate constant force, linear actuation (ease the control) with both good force capacity and range of motion. However, the main drawbacks are the requirement of expensive materials, slow responses and problems from mechanical failure, particularly fatigue. By recalling the specifications for the tremor suppression, EAPs, DEAs in particular, are the best solution in comparison. Moreover, they are cheap, flexible, have a simple actuator mechanism and sufficient range of motion, despite the requirements of high voltage to drive a relatively low actuation force. The following sections give an overview of DE actuation. It begins with applications of DE-based devices, the fundamental theories, failure and durability and characteristics of dielectric elastomer. Research motivation is given at the end of chapter.

1.4 Applications of DE-based devices: actuators and others

This sub-section reviews the highlights of existing DEA applications, the potential and challenges, and other types of DE applications as sensors and energy harvesters.

Despite that there is currently no commercially available DE-based devices, research work has explored its potential over a broad range of applications. Single-layer DEAs are commonly configured in planar and tube form [18, 19, 20, 21]. Tube DE actuators are often combined with springs to generate contraction force [22, 23, 24]. Contractile actuation was also achieved in folded DEAs [25, 26, 27]. A strip DE actuator was folded into an elastomeric stack and the voltage-induced contraction in thickness was used for actuation. Alternative actuator designs have

been based on multi-layer [28, 29] and helical structures [30]. It is shown that with a specific AR configuration, a spring-roll actuator can have multiple degrees of freedom, and drives a starfish-like walking robot [31]. Small-sized DEA-based robots were developed to mimic worm motion [32, 33]. DEAs were also used directly with a passive spring as antagonistic partner. The pivot roll multi-segmented robot is another concept that combines the DEA with stiff skeletal segments to achieve large bending motion (up to 270°) [34]. Bistable DE actuators were developed to switch between two phases [35, 36]. Other highlights are: the planar actuator that can generate rotational motion up to 18° [37], the airship with fish-like propulsion [38], the mini-gripper that grips objects under applied voltage [39] and the touch-sensitive conveyor that detects and rails the payload [40]. Apart from these, DEAs have also been applied in loudspeakers [41, 42], tunable optics [43, 44, 45, 46, 47], tactile displays [48, 29, 49, 50] and valves [51, 52],

DE-based actuators have often been suggested for orthotic and prosthetic applications [53, 54, 55, 56]. The expectations arise from effective cost, muscle-like behaviour and lightness. The actual advancement towards these application are, however, hindered as the practical viability still remains questioned. DEs are vulnerable to electromechanical instability and electrical breakdown, which makes the useful frequency range of operation small [57]. Time-dependent failure such as fatigue has been rarely addressed for DEAs, and the existing results are rather inconsistent [54, 57]. Furthermore, DEs are also susceptible to contaminants [58], electrical and mechanical stress concentrations [20, 59] and even the electrode contact points [57]. They require a precisely controlled, highly repeatable manufacturing technique to produce consistent performance. Partially automatic facilities have been established [54, 60, 61, 62]. Nevertheless, the viscoelasticity of the DE material complicates control and reduces energy efficiency. DEs become stiffer at higher frequency, which limits actuation capacity [63, 64, 57]. The time dependences, the long-term creep, the slow disentanglement of polymer chains, and the resulting stress relaxation all need to be accounted for achieving precise motion [61, 65].

DE generators (DEGs) convert mechanical energy into electrical energy. In terms of energy density, DEGs surpass single crystal ceramics and electro-magnetics by

an order of magnitude [66]. It has been demonstrated that DEGs can harvest energy from natural sources such as ambient vibrations [67, 68], human movements [69, 70], ocean waves [71], wind [72], solar [73], and flowing water [74]. DE sensors (DESs) detect mechanical deformation, and numerous work has been directed towards the development of thin sensor skin for prosthetic applications [75, 76].

1.5 Fundamental theories of Dielectric Elastomer Actuators (DEAs)

The basic structure of a DE actuator consists of a DE film sandwiched by between two layers of electrodes. It converts energies reversibly between electrical and mechanical forms. When it changes electrical energy to mechanical energy, a DE operates in actuator mode. When it changes mechanical energy to electrical energy, a DE acts in generator or sensor mode. The basic physics of the DEs are derived with the assumption that a DE maintains constant volume in the deformation (Poisson's ratio approaches 0.5), which is common for typical DE materials (e.g. rubbers).

DEs, including the electrodes, can be regarded electrically similar to capacitors. The electrical energy arises from two separate aspects. In the first, energy change is due to attraction of *opposite* charges as the capacitor plates moving closer or further apart from each other. In the second part, energy change is due to the repellence of *like* charges as the capacitor plates expand or contract. As the result, the Maxwell stress of a DE under an applied voltage is twice the corresponding normal stress per unit area of a typical parallel plate capacitor. The compliance of a DE gives a second degree-of-freedom for energy conversion. Strictly speaking, the resultant Maxwell stress is not the true normal stress on the polymer (being twice the normal stress). However, since the planar tensile stresses are coupled directly to the thickness direction, the two aspects of energy change can be regarded as one. With the assumption of constant volume of the polymer, the Maxwell stress is simply referred to as the pressure that is exerted over the electro-active region (AR) of the DE.

When the Maxwell stress is applied on the DE, it compresses the film to become thinner. With the constant applied voltage, the resultant Maxwell stress grows simultaneously during the compression. When the voltage approaches a threshold value, the film becomes less stable relative to changes in the physical variables. When reaching the threshold value, the film becomes unstable and collapses until electric breakdown or other types of failure occur. In such a state, the field pressure increases faster than the elastic restoring forces can maintain static equilibrium. This phenomenon is known as the electromechanical instability, alternatively as the pull-in instability, which predominately contributes to failure of a DE under constant driven voltage. It can be avoided by making sure the elastic restoring force increases faster than the equivalent Maxwell force.

Also due to the capacitive nature, only half of the given electric energy input is converted to the work being done on deforming the structure, the other half is stored as electrical energy in the capacitor and recovered at the end of actuation. Therefore, with a constant driving voltage without energy recovery, the maximum theoretical efficiency of DEAs is 50% [34].

1.6 Failure and durability of DEAs

While a DEA may show promising actuation capability, its performance is limited by the dielectric and mechanical strengths of the elastomer. When a DEA is operated beyond these limits, it fails in various modes. The electromechanical instability, which has long been recognised as a failure mode of polymer insulators, is also a primary cause of the failure. This sub-section introduces failure and durability of a DEA, starting with electric breakdown, the electromechanical instability, then move to various mechanical failure modes and finally the approaches that being used to improve durability.

A typical DE film made from 1 mm thick VHB^{TM} 4910 is often driven by voltages of 5 kV and higher, resulting an applied electrical field of 50 MV/m and higher. With various types of voltage amplifiers, it is straightforward to build simple electrical circuit to deliver such high voltages. Therefore the limit for such a high voltage actuator is the electric breakdown field. It refers to the critical electrical

field at which the dielectric material becomes conductive. The consequences of reaching this limit is destructive as the actuator 'burns'. In the ideal case, the electrical field is applied uniformly across the AR, and electric breakdown occurs throughout the whole region. In reality, it occurs locally at the spot with the highest electric field. As the result, the burnt spot causes contact between electrode layers and (if the contact did not happen) provides a small gap, causing electric breakdown through the surrounding air. Either way once it happens, the actuator is completely disfunctioned and cannot be repaired. However, a DEA often fails before reaching the electric breakdown field due to the electromechanical instability.

Mechanical limits also play roles in the failure of DEAs. The loss of tension is one failure mode that occurs when the applied voltage to the DEA is sufficiently large, the AR buckles out of plane and makes the DE cease to be tensile. In this condition the DEA no longer generates the actuation force, which is problematic especially in the spring-roll actuators [22]. The loss of tension indicates a voltage limit which is lower than that of electromechanical instability and dependent on the properties of both the DE and the spring. Derivations from equations of state show that this failure mode always proceeds the electromechanical instability in spring-roll DE actuators [22], whereas other types of DEA tend to fail directly due to electromechanical instability [28, 77, 78]. Compressive limit of the spring is also vital to the functionality of spring-roll actuators. If the compressive force due to the pre-strain of the DEA and external sources is excessive, it deforms the spring plastically and the actuator can no longer generate actuation forces. Hence the compressive limit is also considered as a failure mode. Similarly, tensile rupture is the failure mode that occurs when the DE is stretched excessively.

Generally speaking, the failures due to the mechanical limit of a DEA are associated with the structure of the actuator itself. They are less relevant to the activation of the DEA and can often be eliminated in the design stage by choosing the appropriate components and loading conditions. Electrical breakdown and the electromechanical instability are the primary concerns as they limit actuation strains of DEAs. The electric breakdown field for the polymers is commonly found to increase as the film thickness decreases [79, 80]. Therefore, stretching the film is a common approach for achieving higher a electrical breakdown field,

therefore higher actuation capacity. It is reported that for isoprene rubber, a maximal increase of 40% in the dielectric strength can be achieved by stretching the film. For VHB^{TM} 4910, with the bi-axial pre-strain of 500% in each direction, the dielectric strength is increased by 1100% [81, 82], which is significantly higher compared with a increase in dielectric strength of 40% for isoprene rubber.

The bigger advantage of pre-straining is that it can be used to eliminate the electromechanical instability to achieve much larger deformation [83]. The reason is that pre-strain reshapes the elasticity of the polymer, which pushes the occurrence of the equilibrium between the Maxwell pressure and the compressive stress to a higher strain level. Therefore with the same induced electrical field, the pre-strained DEA actuates with significantly larger strains compared with the unstrained DEA. Noting that an elastomer consists of a network of polymer chains, entangled all together, when the elastomer is stretched, the stress-strain relationship is dominated by the stiffness of the entanglement until reaching the snap point, where all entanglements are fully stretched. This part of the correlation is almost linear. When as the elastomer is stretched further, the detanglement starts to occur until the polymer chains are fully detangled. This contributes to the second part of the stress-strain relationship of the elastomer, where the stress slowly decreases and increases again as the strain increases. As the elastomer is stretched further, the detangled polymer chains are loaded until rupture occurs. The final part of the stress-strain relationship is also approximately linear and much stiffer compared with the first two parts. The unstrained DEA actuates with small strain with the induced electric field and fails to electrical breakdown directly due to the relatively high stiffness of the entanglement. As the elastomer is stretched to approach the snap point (moderate pre-strain), the elastomer actuates with moderate strain under the same induced electric field and fails due to electromechanical instability because the Maxwell pressure increases. This occurs while the material becomes softer as it passes the snap point, the compression accelerates until the film collapses. For a highly pre-strained elastomer, the new stress-strain relationship has no snap point and consequential 'softening'. In this case, the elastomer does not experience the electromechanical instability; it continues to deform until electric breakdown occurs. Such an effect is well-

observed in VHB^{TM} 4910 and significant actuation strain has been demonstrated at pre-strains of 200% and higher [83].

1.7 Characteristics of DEs

Dielectric elastomers are used in many applications, ranging from extreme soft gel-like materials to hard and brittle rubbers with very distinctive material behaviours. The choice of DE is therefore vital for the performance DE actuation. This section introduces the basic characteristics of DEs.

An elastomer is defined as a cross-linked polymer material above its glass transition temperature. Empirically, it is also known as a macromolecular material that deforms substantially when exposed to small mechanical loads, and recovers its original shape shortly after being released. There are three common types of of elastomers, namely, chemically cross-linked (vulcanized) rubbers; physically cross-linked thermoplastic elastomers; and polymers of sufficiently high chain length, where entanglements serve as physical cross-links.

There are several key material properties of DEs that are of interest, including the viscoelasticity that describes how it behaves mechanically; the dielectric constants that describe how well it converts energy in different forms; and the electric breakdown strength that indicates the highest electrical field that can be applied without causing electric breakdown. For polymers, it is generally true that polar groups increase the dielectric constant and the ionic conductance. At the same time, it lowers the chain mobility (e.g. it makes elastomer require larger force to deform) and raises the glass transition temperature. Polydimethylsiloxane (PDMS) is a example of polymer with low dielectric constant (typically between 2.5 and 3), high dielectric breakdown strength and high chain mobility. Polyurethanes (PUs), which contain more polar groups compared to PDMS, have relatively higher dielectric constant (typically 3-10), lower electric breakdown strength, much higher ionic conductivity and glass transition temperature. The polyacrylate elastomer (VHB^{TM} from 3M) deviates from general trends by having extremely high electric breakdown strength when stretched and relatively high dielectric constant, which is generally independent of stretching [82]. Such

features makes it the most commonly used DE in the research field and is the material candidate for this Ph.D. research.

The stretched polymer relaxes as the polymer chains reorientate under stress or in an electric field. The so-called dangling ends, the free ends of the cross-linked polymer chains, and the substructures that are attached to them, are not fixed through cross-links. They relax through a breathing-like motion and act as the sources of relaxation. This motion requires strong deformation of the chain and happens slowly (typically from milliseconds to seconds) [84]. The relaxation of dangling ends contributes primarily to the viscoelastic response of the most elastomers that occurs from seconds to days in duration.

The permanent, chemical, physical, or topological cross-links contribute to the elastic behaviour. In the model of the phantom limit of the elastomer, it assumes in a such phantom network that the chains are devoid of material properties, the chains move freely through one another, the elasticity only arises from the network connectivity [85]. In the model of affine networks of an elastomer, the end-to-end chain vectors are assumed to transform affinely with the macroscopic deformation. The phantom and affine limits are the two extreme cases to describe the properties of the most elastomers. The network is predicted to be more affine-like at small deformations and more phantom-like at larger deformations. Nevertheless, the topological constraints of the polymer chains, namely entanglements [86, 87] serve as the third factor that contributes to the elasticity of the elastomer.

The time-dependence, or the viscoelasticity of the elastomer, is usually measured in terms of the storage modulus and the loss modulus [88]. For completely cross-linked rubbers, the material store all the energy like a ideal spring. In reality, the elastomers always have some extent of viscous dissipation since ideal cross-linking is very hard to obtain. However, it may be favourable for the material to be viscous at a given frequency and to be elastic at another frequency, in applications where conformability and stability are required. This can be obtained either by choosing network reactants with certain chemical structures and lengths, or to swell the elastomer in a compatible solvent. The latter is an easy method to obtain a fast-responding soft material. A new trend has also emerged, the so-called interpenetrating networks (IPNs). They hold physically the mixture of

two or more cross-linked networks altogether via entanglements, which provides a convenient route to modify properties to meet the specific needs [89, 90].

With the same reactants, one can obtain elastomers ranging from extremely soft and fragile to hard and durable, as the cross-linking reaction, also known as vulcanization of polymers into elastomers, can be performed in several ways. The traditional way of producing hard rubbers is radical vulcanization where the cross-links are introduced randomly along the chain. End-linked addition curing systems control the distance between cross-links without byproducts, which allows the controlled alteration of the material properties and formation of soft elastomer. The resulting elastomer can be further optimised by adding volatile or non-volatile solvent, chain extenders, resins, or other polymers physically or mechanically to the network [91]. Because the elastic modulus of the elastomer depends on the degree of cross-linking, it can also be altered as a function of reaction time of vulcanization. The longer vulcanization proceeds, the more cross-links are developed and the stiffer and less viscous the elastomer becomes. Vulcanization can be slowed down by adding a non-volatile solvent. For example, adding high viscosity silicone oil to a silicone network will increase the distance between reactive groups and the overall viscosity of the reaction mixture, and hence decrease the reaction speed [92]. Alternatively, vulcanization can be stopped by cooling down the reaction mixture to inhibit the catalyst, which stops the network formation at a given time to give certain properties.

Swelling, as another common approach, softens an elastomer by reducing the contribution of the entanglement to the elastic modulus. It can be applied both before or after vulcanization. Mixing the reactants with swelling agent before vulcanization (pre-swelling) is the most applicable method, but it may lead to soft and fragile networks due to the dilution of trapped entanglements [93]. The post-swelling method has the issue of causing uneven elastomers due to small imperfections within the initial 'dry' elastomer. Swelling also affects the dynamics of the swollen resulting elastomers. It brings the so-called dangling material, which refers to the large fraction of material chemically attached to the network but not elastically active except on short timescales, to contribute to the relaxation of the elastomer. The relaxation time of the elastically active network fraction is also decreased due to dynamic dilution effects [94] as well as the so-called stran-

gulation or tight-mesh effect [95]. Another method to soften the elastomer is to pre-swell the elastomer reactants by a volatile solvent and then remove solvent after vulcanization. It therefore reduces the entanglement contribution to elastic modulus without changing the dynamic properties of the elastomer significantly.

1.8 Research motivation and focus

The research interest of this thesis has arisen from the potential use of DEAs to make active wearable devices for regulating involuntary movements in the human body. As the existing treatments are far from satisfactory, active wearable devices with soft actuation technologies may be a feasible solution for long-term tremor monitoring and motion regulation. The overview presented identifies promising opportunities for DE actuation and also explains the complexity of failure modes and material behaviour. The research motivation is the potential use of DE actuation for applications such as tremor suppression. This research therefore focuses on the three specific areas of DE actuation: performance enhancement; modelling accuracy; and self-sensing control.

1.9 Outline of thesis

This thesis describes experimental and theory/simulation work for the advancement of DE actuation. The motivation is for the field of soft robotics.

Chapter 1 introduces the current progress in tremor suppression, wearable robotics, soft actuation and fundementals of the DEA. This provides the research motivation.

Chapter 2 provides a thorough literature review of the relevant research associated with DEAs, identifying the research gaps and defining the research objectives.

Chapter 3 presents work to enhance the actuation performance of a DE actuator. A novel rod-prestrained dielectric elastomer actuator (RP-DEA) was developed, showing the improved force output, but degraded durability. The latter was then

suppressed via electrode optimisation. This covers theory, experimental design and setup, the experiment and simulation results and discussions.

Chapter 4 presents the research in improving the modelling accuracy of a viscoelastic DE-based actuator. The effectiveness of higher order material model was verified against experimental results from polyacrylate and compared with the conventional model and spring-like silicone. The experiments and simulations are different from previous research.

Chapter 5 presents the work in the self-sensing control of DE actuation. A novel self-sensing mechanism of the DE actuation was developed and demonstrated in a dielectric elastomer self-sensed actuator (DESA) and compared with a conventional self-sensing mechanism.

Chapter 6 summarizes the conclusions drawn from Chapters 3, 4 and 5, and identifies potential future work. A list of publications and references follow.

Chapter 2

Literature review

This chapter outlines the state-of-the-art as well as justification for the research of the thesis. It begins with performance enhancement, describing two common techniques, pre-straining and motion constraining, and identifies the possibility of combining them for further enhancement. The following section, modelling and simulation, therefore reviews the existing models of DEAs for different purposes, including accurate modelling of the dynamic characteristics in the frequency domain. The third section depicts advantages and disadvantages of existing self-sensing mechanisms of DEAs. Finally, identification of research gaps, the research question and objectives follow.

2.1 Performance enhancement

Performance enhancements are referred to as the techniques applied on DEAs in the pre-actuation state to increase the actuation capability. Two common enhancement techniques are pre-straining and motion constraining.

2.1.1 Pre-straining

Pre-straining improves DE actuation in several ways. It reshapes the stress-strain relationship of the DE and makes the structure thinner [96]. To induce the same electrical field, a lower driving voltage is required for pre-strained DEAs compared with that for unstrained DEAs. Moreover, as mentioned before, pre-straining increases the dielectric strength with decreased thickness, experimental results show a 1100% increase in electric breakdown field of polyacrylate, VHB$^{\text{TM}}$ 4910 with 500% bi-axial pre-strain in planar directions [82]. The same study also showed an approximately 5% drop in the dielectric constant with the same bi-axial pre-strain condition, indicating the presence of a small electrostrictive effect in DE actuation.

Pre-straining eliminates electromechanical instability. It has been shown that pre-straining along the axis of a tubular DE balloon can suppress the snap-through instability during inflation and regulate the reaction force along the axial direction [97]. More optimised electromechanical performance of DE actuators can be achieved by controlling the form and distribution of pre-stress [98, 99].

The level of pre-strain is not the sole factor that may eliminate the electromechanical instability and enhance DE actuation; studies show that the voltage-induced deformation is also strongly affected by how the mechanical loads are preset [100, 96, 101, 102]. In fact, DEAs have different electromechanical responses under uniaxial, biaxial, and shear forces [103, 96, 104, 105]. Larger actuation strain has been demonstrated for a membrane under a equal-biaxial loading compared with that under a uniaxial force. Pure shear loading was shown to cause decreased tensile force as the voltage increases [105, 106, 107]. These results show that the actuation performance of DEAs can be tuned by altering mechanical loading conditions before the application of driving voltage [108].

Theoretical analyses provide insight and guidance in designing such DE structures and devices. Huang *et al.* [109] demonstrated that voltage-induced expansion could reach 488% of strain in area when a DE membrane is subjected to biaxial dead loads. Keplinger *et al.* [110] and Li *et al.* [111] achieved a large

voltage-triggered expansion of area by 1692% in a DE membrane by harnessing the electromechanical instability with air pressure control.

2.1.2 Motion constraining

When a DEA is loaded differently in two planar directions, the elastomer is stiffened in the direction with higher load. When the voltage is applied, the deformation occurs favourably in the direction where the elastomer is softer, hence results in rather small actuation strain under the uniaxial force. Such phenomenon was explained theoretically and exploited as the enhancement technique of motion constraining. Especially in the uniaxial actuation condition, larger actuation strain can be achieved by constraining the elastomer in the lateral direction to the actuation.

One approach is to sandwich nylon fibers between two layers of elastomer. The results show that the enhanced silicone-based DEAs generate up to 35% linear strain [61]. Lu *et al.* [96] report that unidirectional constraints by carbon and nylon fibres in the cross-direction polyacrylate-based DEAs generate 28% and 25% linear actuation strain, respectively. The study also shows that the enhancement is lower than predicted because such a method does not fully constrain the DEA and fibres buckle due to the compressive stress. Moreover, the fibre-constrained tube DEAs generate up to 36% strain [109]. In general, enhanced actuation strains were in the range from 25% to 30% compared with 10% to 15% from an unenhanced DEA. The force output of a DEA was also reported to improve when the fibre is aligned laterally to the direction of actuation. The other approach is to embed fibres directly in the DE film. Subramani *et al.* [112] show that by adding high-dielectric-constant fibres as fillers to the elastomer matrix, the performance of DEAs is enhanced further by having both motion-constraning and an improved dielectric constant.

Typically, fibres only constrain the film partially. It indicates with better fibre coverage, even larger actuation strain can be achieved. It has been demonstrated that with the electrode made of highly aligned carbon nano-tubes (CNTs), the actuation strains can be pushed further to over 40% in a relatively low electri-

cal field of 100 Vμm^{-1} [113]. The electrode-induced anisotropy in this study is obtained by having CNTs aligned in the horizontal direction to enhance the actuation in the vertical direction. The CNTs were applied to the elastomer using a stencil mask adhered to the sticky surface. However, despite the initial actuation strain being high, it does reduce over strain cycles as the CNTs tend to lose the orientation and become bundled.

2.1.3 Combining pre-straining and motion constraining

Because pre-straining and motion constraining are different enhancement approaches, they can be combined so that the DEA has improved dielectric strength, mechanical properties (due to pre-strain) and favourable actuation direction at the same time. Such combination can theoretically further boost the actuation capacity, but this has rarely been studied.

Bolzmacher *et al.* [61] used nylon fishing line as the fibre material to pre-strain a silicone elastomer by 100% on the upper surface of the elastomer so that the whole structure remains compliant for application on a human arm. Their results showed promising improvements in actuation strain, electromechanical properties and breakdown strength. However, this would also make the DEA relax naturally into a curved form. If subjected to higher pre-strain, such as over 200%, curvature would become excessively large and because the structure is no longer aligned in-plane, it may degrade the uniaxial force output in the actuation direction. In order to maximise the force output of a DEA, the pre-strained structure may be kept flat to ensure that the expansion of the elastomer occurs in the actuation direction.

2.2 Modelling and Simulation

This sub-section reviews existing modelling approaches in simulating hyperelasticity, viscoelasticity and failure of DEAs. These approaches are based mainly on a spring-damper rheological model, which is often used to represent the dielectric elastomer. The representation contains a spring and a spring-damper

combination that are connected in parallel. The spring indicates the stiffness of the elastomer in static loading condition, and the spring-damper combination gives rise to dynamic characteristics.

2.2.1 Modelling in hyperelasticity

Because the elastomer has strain-dependent elastic modulus, the nonlinear stress-strain behaviour has been simulated using the Ogden model [114], the Gent model [115], the Mooney-Rivlin model [116] and the neo-Hookean model [117]. Among them, the neo-Hookean model is more suitable for simulating small strain variations, the Mooney-Rivlin model is better over a broader range of strain, the Ogden model is more sophisticated over higher strain, and the Gent model accounts for the extensibility, the stretch limit of the material.

Numerous DE models have been developed based on these hyperelastic material models. Kofod [118] applied both Ogden and Mooney-Rivlin models to fit force-strain experimental data up to 500 % strain values for a commercially available acrylic elastomer, VHB^{TM} 4910. It was reported that the Ogden model showed superior fit compared to the Mooney-Rivlin due to more free parameters as well as the presence of exponent terms. Lochmatter *et al.* [103] proposed a hyperelastic model corresponding to the Ogden form to predict the uniaxial tensile deformation behaviour of VHB^{TM} 4910 acrylic elastomer up to a tensile stretch ratio of 8. The same model was then applied to characterise electromechanical coupling of a planar DE actuator made with this acrylic material. Furthermore, Goulbourne [119] proposed a modified Ogden strain energy function to describe the mechanical behaviour of new synthesised interpenetrating polymer networks (IPNs) of acrylic elastomer up to the stretch ratio of 8. Li *et al.* [111] applied the Gent model to characterise the large voltage induced deformation of VHB^{TM} 4910 elastomer.

In the field of DE-based energy harvesting, Xiaofeng *et al.* [120] studied a DE energy harvester with the Gent and neo-Hookean models for an understanding of how viscoelasticity affects the energy conversion and dissipation. Li *et al.* [121]

modelled DE energy harvesting in an inhomogeneous field using the neo-Hookean model.

In the field of DE-based oscillators, Fox and Goulbourne [122] examined the dynamic behaviour of an axisymmetric DE membrane resonator based on the Ogden model, while Zhou *et al.* [123] studied viscoelastic and hyperelastic models of the DE. The latter work showed that neglecting the viscoelastic behaviour of the DE may lead to significant errors in the dynamic response of the oscillator. The resonant behaviour of a DE membrane mounted on a rigid ring was studied by Zhu *et al.* [124] with the neo-Hookean model. Apart from these, a novel approach was also taken to model hyperelastic material based on a bond graph formalization [125].

2.2.2 Modelling in viscoelasticity

In contrast, much less attention has been paid to the modelling of the viscous aspects of material behaviour. Yang *et al.* [126] adopted linear theories to investigate the material viscoelasticity of DEs under small deformations. Hong [127] developed a general field theory for the coupled electro-viscoelastic behaviour of dielectric elastomers, by integrating a formulated theory of deformable dielectrics into a framework of non-equilibrium thermodynamics for continuum. The theory has great adaptiveness for various viscoelastic materials. The similar model framework was also employed by Foo *et al.* [128] for investigating dissipative performance of DEs at different stretch rates and stretch ratios up to 7. Hossain *et al.* [129] proposed a modified Bergstrom-Boyce viscoelastic model with a finite strain linear evolution law to simulate the response of VHB$^{\text{TM}}$ 4910 in various step-based standard testing. They combined a micromechanical eight-chain model [130] and diffusion based transient network model [131] to predict the elastic and the viscoelastic responses, respectively.

Wissler *et al.* [132] presented a quasi-linear viscoelastic model in which the basic behaviour of a DE were characterised as a hyperelastic strain energy potential (e.g., Ogden and Mooney-Rivlin forms), and a time function such as the Prony series was introduced into the strain energy function to depict the materials

time-dependent properties. Wang *et al.* [133] developed a finite element analysis approach to investigate the role of viscoelasticity in the instability of the soft dielectrics such as pull-in, wrinkling, electrocreasing and electrocavitation. Lochmatter *et al.* [103] used a hyper-viscoelastic model to demonstrate the unstable actuation behaviour in long-term actuation of planner DEA. Wang *et al.* [105] developed a constitutive relation which was derived from Kelvin-Voigt rheological model to characterise energy dissipation of the DE under uniaxial stretching and loading-unloading hysteresis loops at different stretch rates up to the maximum of 5.

2.2.3 Modelling in failure

Modelling work has also focused on understanding and simulation of failure of DEAs. Premature failure analysis of the DEA was undertaken using linear stress-strain relationships to investigate the failure mode of the electromechanical instability [28, 134, 135].

These studies initially considered the DEA entirely covered by AR without any surrounding inactive region. The DE was assumed to be purely elastic with the constant elasticity and free boundary condition are assumed. As derived directly from the electromechanical correlation, the analysis revealed the mechanism of the electromechanical instability. A numerical model was then developed to take the actual boundary condition into account. However, the predicted threshold values of stretch for the electromechanical instability by these linear-model-based studies were only half of the actual values obtained from experimental results [136, 21].

Nonlinear model have been developed to include large deformations, nonlinear elastic properties and the viscoelastic behaviour of DEAs. With the simplifications of neglecting localised effects such as defects, voids, inclusions, electrical and mechanical stress concentrations and time-dependent failure (e.g. creep and fatigue), the model showed good agreement in failure prediction with the experimental results. The model also showed for a hyperelastic material that viscoelasticity has positive impact on the reliability, as it stiffens the DE against

electromechanical instability. The rate of stretch during the pre-strain process affects significantly failure modes. A high stretch rate leads to dielectric strength failure and low stretch rates lead to electromechanical instability.

For applications, nonlinear analysis has been adopted for failure predictions and stability studies in folded DEAs [137], pre-strained DEAs [98], dielectric gels [138], tube DEAs [139] and dielectric elastomer generators [140, 141].

2.3 Self-sensing DE actuation

Achieving precise motion in the DEAs is vital towards the actual commercialisations, especially regarding the nonlinearity in the material property of the elastomer and susceptibility to the failure. One option is to apply closed loop control that monitors and adjusts the status of the DE throughout the operation. This sub-section reviews the state-of-the-art on closed loop control of DEAs with external sensors and existing self-sensing mechanisms via capacitive and resistive sensing.

2.3.1 Closed loop control in DE actuation

Much work has been devoted to the closed loop operation of DE actuation [142, 143, 144, 145]. These show that with the feedback provided by external sensors, precise motion control can be achieved with linear proportional-integral-derivative (PID) controllers.

The highlights of early work in this area are evidenced by Xie *et al.* [146] who demonstrated a PID closed loop quasi-digital voltage control system for controlling the actuation voltage to compensate for nonlinear material behaviour of DEs. Randazzo *et al.* [144] showed closed loop control of a rotational joint driven by two antagonistic dielectric elastomer actuators. Demonstrations were also made in active vibration control using DE actuators [147, 145] and PWM-based motion control of DEA arrays with multiple degrees of freedom using single power supply [148]. Controlling a DEA-based tunable grating is another typical example [46].

A compliant grating is placed on the DEA so that it deforms with the DE as the voltage is applied. It uses the first-order diffraction angle of the grating that is measured by a photo-diode to drive the DEA to the desired deformation.

More recent work is due to Hodgins *et al.* [149] who applied closed loop operation in a DEA, simulating biasing systems with force and displacement as feedback. Jones *et al.* [150] proposed a model-based design procedure for PID controllers for tube DE actuator. Compared with their previous work in open-loop model-based control [151], the study suggested that closed loop control is advantageous compared with open-loop inverse model-based control, especially because it fully compensates the strong time-dependency of the DE, which is difficult to model accurately.

2.3.2 Capacitive self-sensing

Having external sensors complicates the system complexity and raises the cost of the system, especially when considering the intention of utilising a low-cost polymeric actuation approach. The alternative is to use a DEA itself as a motion sensor, to form a self-sensing DEA. Among the two common self-sensing approaches, capacitive self-sensing show high popularity over resistive self-sensing.

As the capacitive change of a DEA can not be measured directly, it is commonly evaluated based on voltage-current relationship from the input and outputs of the capacitor. One approach is to use a high frequency AC signal that is superimposed on the high voltage that actuates the DEA [76, 152]. It is achieved by connecting the DEA to an external resistor in series to form a RC circuit. The variation in the voltage across the DEA due to actuation has been used to estimate to the capacitive change for self-sensing feedback. Other approaches use pulse width modulation to measure the capacitive discharge rate [148], and step voltage application to measure charge [153].

In order to approximate state of DE actuation from the estimated capacitive change, algorithms have been developed. Rizzello *et al.* [154] implemented an algorithm based on robust control theory and linear matrix inequalities with a self-sensed DEA to show improved robustness and actuation performance with

respect to model nonlinearities. The same group also demonstrated a self-sensing approach based on on-line estimation algorithm [155]. Hoffstadt *et al.* [156] proposed an self-sensing algorithm based on the recursive extended least squares method to reduce measurement noises and improve sensing resolution. Ye *et al.* [157] implemented artificial neural network in nonlinear data fitting to estimate capacitive change in a self-sensed strip DE actuator.

Capacitive self-sensing for DE actuation has proved compromising in many applications. In the case of controlling the grating, the voltage-induced expansions in the ARs are measured in terms of capacitance. Due to the linear relationship between the capacitive change and the first-order diffraction angle, the control of the grating was achieved by self-sensing the capacitive change [158]. Gisby *et al.* [159] employed capacitive self-sensing to control multiple independent DEAs using a single high voltage power supply. Their more recent study demonstrated that capacitive self-sensing in a DEA-based manipulator can both detect the contact when reaching the object and gather information on the object's stiffness [160]. Shintake *et al.* [161] adopted capacitive self-sensing for controlling a multifunctional soft griper. Branz *et al.* [162] adopted capacitive self-sensing for controlling a redundant robotic arm based on DEAs.

While the concept of capacitive self-sensing has proved promising, it is also shown that large deformations of DEAs (e.g. >10% strain) and the coupled high electric fields (of the order of MV/m) during the actuation may cause complex changes in the electrode resistance and dielectric resistance, which leads to unexpected capacitive response in DE actuation [163, 164, 165, 128].

2.3.3 Resistive self-sensing

Very few researches have focused on resistive self-sensing. O'Brien *et al.* [166] considered this approach for DE actuation in micro-electromechanical systems. In their work, electrically isolated circuits were used to measure electrode resistance and driving voltage of the DEA. These feedback signals were used with a model to predict the state of actuation. The proposed self-sensing mechanism showed initial inaccuracy of 20% of the full sensor range, which then reduced down to

5% within the first 5 seconds of operation. A good qualitative match was found between the sensor-estimated state and the actual state of actuation. Apart from the modelling errors against simulating long-term creep of DEs, the study also showed the conductivity of the electrode highly depends on many factors, including the electrode material, the electrode configuration and the deformation of the DE. Capacitive self-sensing is therefore considered to be more reliable because the capacitance of the DEA solely depends on the geometry of the capacitor and the electrode coverage [160, 159].

2.4 Literature review summary and research gaps

Dielectric elastomers are in a special class of electro-active polymers with excellent electromechanical properties for various potential applications. With electrode coated on the surface of a DE, it forms a compliant capacitor that can be used to convert energy between the electrical and mechanical forms, which leads to the development of actuators, energy generators and sensors.

The elastomeric characteristics allow DE devices to undergo large deformations, which outclasses most of other soft actuation technologies. In addition, DE devices feature light weight, noise-free, effective costing and high energy density. In actuator form, they offer actuation capability that is similar to that of human muscles. The promising performance of DEAs has been demonstrated over a broad range of applications, from micro-electromechanical systems to larger scale bio-inspired airships.

However, there are research gaps in DE actuation to be filled to address the challenges for eventual commercial applications. Firstly, the operation of a DEA requires high voltage input and generates relatively small force. Reducing driving voltage and improving actuation capability requires advanced materials with better electromechanical properties and optimised structures to exploit the full potential of DE actuation. Secondly, elastomeric material properties give a DE not only softness that allows large deformation, but also nonlinearity in elastic modulus and viscoelasticity. Strong strain-dependent, rate-dependent and

time-dependent behaviour of DEs requires sophisticated modelling and control to achieve consistent and precise motions.

Moreover, DEAs are susceptible to various modes of failure even in their simplest form, and such vulnerability scales up as the structure becomes more complicated. In particular, when a DEA is combined with rigid frames, the design must be rigorous to avoid any stress-concentration, that weakens its durability, leading to catastrophic failure and causing the complete malfunction of the actuator. Finally, DEAs are easy and cheap to fabricate, such advantages should not be compromised while achieving precise motion control of actuation. For further advancement of DE actuation and control, attention is drawn to three specific areas of DE actuation: performance enhancement; accurate modelling; and self-sensing control.

The literature review of performance enhancement shows the great potential in amplifying actuation capability of DE actuators via enhancement techniques of pre-straining and motion constraining. Pre-straining reshapes the stress-strain curve of a DE material and reduces the thickness of DEAs. This makes the enhanced DEAs generate larger actuation strains and forces. Moreover, pre-straining improves the dielectric strength and suppresses electromechanical instability. It allows the enhanced DEAs to operate at higher driving voltage for further improvement in actuation. Motion constraining introduces anisotropy to the structure and makes the deformation of DEs occur favourably in the actuation direction. Each enhancement technique has been investigated extensively, however, the combination and the corresponding effects on actuation output and durability of DE actuators has been studied only rarely.

The literature review in modelling and simulation shows a broad coverage in the understanding of hyperelasticity, viscoelasticity and failure mehanisms of DE materials. Models for hyperelasticity have been developed to simulate the stress-strain relationships of DEs under mechanical loading and predicting the maximum stretch before fracture. Models for viscoelasticity have been developed to determine the time-dependent behaviour of DE elastomer. Models for failure have been developed to identify and predict different failure modes in various DEA configurations, therefore guiding actuator design. Despite of the high de-

mand for accurate models to implement precise motion control, a model that describes the characteristics of DE materials and DE-based actuators in the frequency domain has yet to be developed.

The literature review in self-sensing control shows that different approaches have been taken for closed loop operation of DE actuation. Capacitive sensing estimates capacitive change of DEAs during the actuation, which indicates the state of actuation and may be used in feedback for control. This approach has been shown to be more reliable than resistive sensing and its effectiveness has been demonstrated through numerous applications. There are two main issues associated with a capacitive self-sensing mechanism, namely, drift in the capacitance-deformation relationship and difficulty in implementation. The former is due to presence of a high electrical field (of the order of MV/m), which interferes with measurements; the latter that, capacitive self-sensing requires superposition of high voltage for actuation and excitation signals for sensing, which can only be achieved using particular power supplies. A novel capacitive self-sensing mechanism that addresses these issues is therefore desired.

In this thesis, the author strives to tackle some of these challenges, from combining enhancement techniques, characterising and modelling the nonlinear behaviour, and designing a robust and reliable self-sensing mechanism. The effort has been devoted to seeking novel opportunities and constructing cornerstones for more advanced and applicable DEA applications.

2.5 Research questions and objectives

There are three fundamental research questions to be answered:

- Can a DE actuator have sufficient actuation capability (e.g. actuation force in N)?
- How accurate can a DE actuator be controlled in the frequency domain?
- How reliable can a self-sensing DE actuator be fabricated?

Three objectives of the current study are defined respectively as:

1. To investigate the actuation capability of DE actuation.
2. To characterise and model the dynamics of DE actuation.
3. To achieve robust and reliable self-sensing DE actuation.

Chapter 3

A durable and high-performance DEA

This chapter addresses the research gap in performance enhancement as identified from Section 2.1. It presents the design of Rod Pre-strained Dielectric Elastomer Actuators (RP-DEAs) in their capability to generate comparatively large static actuation forces with increased lifetime via optimised electrode arrangements. RP-DEAs utilize thin stiff rods to constrain the expansion of the elastomer and maintain the in-plane pre-strain in the rod longitudinal direction. The aim is to study both the force output and the durability of the RP-DEA. Initial design of the RP-DEA had poor durability, however, it generated significantly larger force compared with the conventional DEA due to the effects of pre-strain and rod constraints. The durability study identifies the in-electro-active-region (in-AR) lead contact and the non-uniform deformation of the structure as causes of premature failure of the RP-DEA. An optimised AR configuration is proposed to avoid actuating undesired areas in the structure. The results show that with the optimised AR, the RP-DEA can be effectively stabilized and survive operation at least four times longer than with a conventional electrode arrangement. Finally, a Finite Element simulation was also performed to demonstrate that such AR design and optimization can be guided by analyzing the DEA structure in the state of pre-activation.

3.1 Motivation

The demand for soft active wearable devices, either in exoskeletons or rehabilitation robotics requires novel actuation solutions that can be closely, harmlessly and comfortably embedded to assist, enhance and regulate typical human motions. Dielectric Elastomers (DEs) are in a specific class of Electro-Active Polymers (EAPs) that are of particular research interest due to their simplicity of structure, low mass/inertia, robustness, noise-free operation, and actuation force density that is similar to that of human muscles [34, 167, 168, 169, 97, 170, 17, 171, 121, 172]. A Dielectric Elastomer Actuator (DEA) may be fabricated from a single layer of DE that is coated with a compliant conductive material on both sides. Functionality arises from a shortening in thickness and expansion in-plane when a voltage is applied across the conductive layers. Its electro-mechanical properties have been studied extensively in numerous applications such as soft robotics [173, 174, 175, 176, 177, 178], sensors [75, 76], artificial muscles [179, 180, 181] and energy harvesting [141, 182].

3.1.1 DEA failure and durability

While a DEA may show promising actuation capability, its actual application is limited by the poor durability of the structure. Previous studies suggest that a typical DEA fails due to:

A1. Dielectric strength limitation (the most common failure mode)

A2. Mechanical strength limitation

A3. Pull-in instability

The dielectric strength limits the maximum electrical field that can be applied to a DE film, while the mechanical strength limits its maximum deformation. Pull-in instability occurs when the film thickness falls below a critical value and the developed Maxwell Pressure becomes bigger than the compressive stress of the DE film. This positive feedback effect makes the compression unstable and ultimately leads to electric breakdown [111, 28]. The pull-in instability also limits

the performance of an actuator under low applied voltage, hence methods have been proposed to suppress such instability and improve the actuation performance [111, 83]. Other factors such as defects, visco-elastic behavior of the elastomer, fabrication process and electrode deposition have the impact on the durability of a DEA [183, 77]. Neoprene^{TM} glue has been used to cover the defects and single-walled carbon nanotubes have been developed to improve DEA durability [183, 184]. While intensive studies have focused on understanding and improving the durability of typical DEAs, the failure and durability from the perspective of structural analysis have received limited attention.

3.1.2 Pre-strain and motion constraining

The force and displacement outputs of a polyacrylate-based DEA can be improved mainly through two approaches: (i) pre-strain; and (ii) motion constraining. Each has been reported to improve the actuation capacity of DEAs significantly [97, 96, 109, 185]. Pre-strain improves the performance by:

B1. Reducing the thickness of the film

B2. Making the structure extend preferably in the actuation direction

B3. Shifting the stress-strain curve of the elastomer

to eliminate the peak in the stressstrain curve, hence improving electromechanical responses by suppressing the pull-in instability. In addition, pre-strain improves the dielectric breakdown. Non-uniform pre-strain also enables the film to expand in the less-strained direction when activated.

Motion constraining is a technique to improve the DEAs movement in the desired direction by constraining its movement in other directions. To do so, one approach is to combine the DEA with rigid frames. One example is the diaphragm actuator in an electrostrictive polymer film loudspeaker [186]. A common approach is to use fibre-reinforcement. Tube-form DEAs with nylon fibres applied in the radial direction have been investigated [96, 109]. A more complex fibre matrix has also been applied to the electrode as a carbon nanotube electrode sheet [113]. The selection of the fibre was investigated to improve the electrome-

chanical properties of the DE [112]. In general, enhanced actuation strains were in the range from 25% to 40% compared with 10% to 15% from an unenhanced DEA. The force output of the DEA was also reported to improve when the fibre is aligned laterally to the direction of actuation.

Fibre pre-strained DEAs were proposed to hold pre-strain in the transverse direction to the uni-actuation. Bolzmacher et al. [61] used nylon fishing line as the fibre material to pre-strain a silicone elastomer by 100% on the upper surface of the elastomer so that the whole structure remains compliant for application on a human arm. Their results showed promising improvements in actuation strain, electromechanical properties and breakdown strength. However, this would also make the DEA relax naturally into a curved form. If subjected to higher pre-strain, such as over 200%, curvature would become excessively large and because the structure is no longer aligned in-plane, it may degrade the uniaxial force output in the actuation direction. In order to maximize the force output of a DEA, the pre-strained structure may be kept flat to ensure that the expansion of the elastomer occurs in the actuation direction.

3.1.3 Motivation and approach

The aim is to study the force output and the durability of a RP-DEA structure, which incorporates rigid metallic rods to maintain the pre-strain and constrain the expansion in the lateral direction. The force output of a conventional DEA under bi-axial pre-strain is compared with the RP-DEA. It is shown how the RP-DEA outperforms the conventional DEA in force output by gaining the advantages from both pre-strain and motion constraint. The durability of the RP-DEA is evaluated. Through Finite Element simulation it is shown that the non-uniform deformation of the DE is a primary source of premature failure of the RP-DEA. Finally, by optimising the active region (AR) configuration, the durability of the RP-DEA can be significantly improved without requiring any other modifications to the structure.

3.2 Theory

The RP-DEA utilizes both pre-strain and motion constraint to improve the force output. This section derives the correlation between the bi-axial pre-strains and the force output of a DEA, to be compared with experimental data.

The force outputs of a DEA are parameters of importance. In an in-plane direction denoted by the subscript i, let f_i be the difference between the force in the pre-strain state, F_{pi}, and the force in the activated state, F_{ai}, as denoted by:

$$f_i = F_{pi}(\lambda_{1,pre}, \lambda_{2,pre}) - F_{ai}(E, \lambda_{1,pre}, \lambda_{2,pre}) \tag{3.1}$$

where $\lambda_{1,pre}$ and $\lambda_{2,pre}$ are the in-plane pre-strains, and E is the electric field across the thickness. When external mechanical stresses σ_1, σ_2 and the electric field E are applied to the DE, the equations of state are [122]:

$$\begin{aligned} \lambda_1 + \varepsilon E^2 &= \lambda_{1,pre} \frac{\partial W(\lambda_{1,pre}, \lambda_{2,pre})}{\partial \lambda_{1,pre}} \\ \lambda_2 + \varepsilon E^2 &= \lambda_{2,pre} \frac{\partial W(\lambda_{1,pre}, \lambda_{2,pre})}{\partial \lambda_{2,pre}} \end{aligned} \tag{3.2}$$

where $W(\lambda_{1,pre}, \lambda_{2,pre})$ is the elastic free energy density function of the elastomer and ε is the dielectric permittivity of the elastomer. When the DE is under pre-strain only, the resultant mechanical stresses, σ_1 and σ_2, can be solved by setting $E = 0$, which gives:

$$\begin{aligned} \lambda_1 &= \lambda_{1,pre} \frac{\partial W(\lambda_{1,pre}, \lambda_{2,pre})}{\partial \lambda_{1,pre}} \\ \lambda_2 &= \lambda_{2,pre} \frac{\partial W(\lambda_{1,pre}, \lambda_{2,pre})}{\partial \lambda_{2,pre}} \end{aligned} \tag{3.3}$$

The stress differences between the actuated and pre-strained states are:

$$\Delta\sigma_1 = \Delta\sigma_2 = -\varepsilon E^2 \tag{3.4}$$

By assuming that the pre-strains will not significantly affect the dielectric property of the material, the net stresses are functions of the applied electric field and permittivity of the DE. With the assumption of the incompressibility: $\lambda_1\lambda_2\lambda_3 = 1$, the resultant net forces are related to σ_1 and σ_2 by:

$$\begin{aligned} f_1 &= \frac{\sigma_1 L_2 H}{\lambda_{1,pre}} \\ f_2 &= \frac{\sigma_2 L_1 H}{\lambda_{2,pre}} \end{aligned} \tag{3.5}$$

where L_1, L_2 and H are the in-plane dimensions and thickness, respectively, of the DE film in the undeformed state. The applied electric field is related to the applied voltage V by:

$$E = \frac{\lambda_{1,pre}\lambda_{2,pre}V}{H} \tag{3.6}$$

It now follows that:

$$\begin{aligned} f_1 &= -\frac{\varepsilon V^2 L_2}{H}(\lambda_{1,pre}{\lambda_{2,pre}}^2) \\ f_2 &= -\frac{\varepsilon V^2 L_1}{H}(\lambda_{2,pre}{\lambda_{1,pre}}^2) \end{aligned} \tag{3.7}$$

3.3 Experimental methodology

3.3.1 DEA configurations

Two experimental assessment phases consisted of: (a) Force Measurement; and (b) Life Assessment. Different DEA configurations were used for each experimental set as shown in figure 3-1. In force measurement, the samples were configured to have the total AR area of 30 mm $\times$ 30 mm to fit in the bi-axial stretch system shown in figure 3-1c. The corners near the AR were rounded to avoid stress

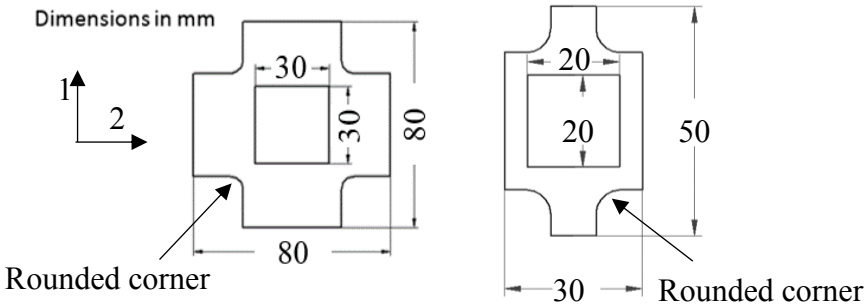

(a) (b)

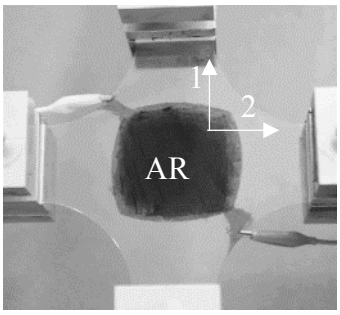

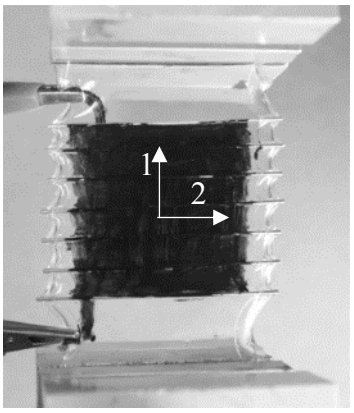

(c) (d)

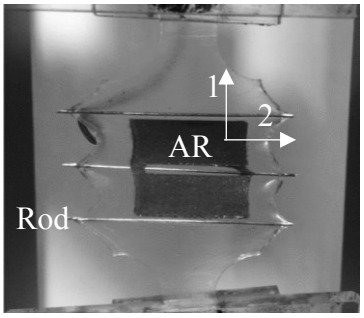

(e)

Figure 3-1: Sample configurations for: experiment sets (a, b); and the actual samples (c, d, e). (AR refers to the active electrode region for DE actuation)

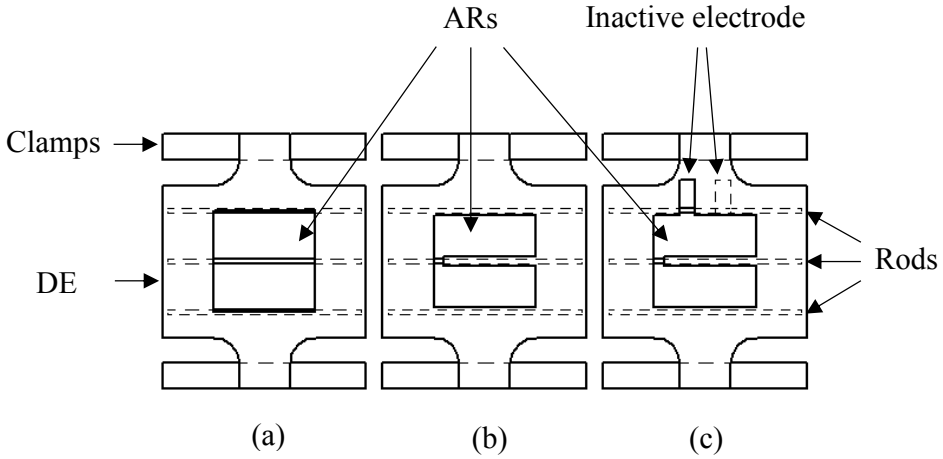

Figure 3-2: Configured Rod Pre-strained Dielectric Elastomer Actuators (RP-DEAs) in life assessment: (a) single AR; (b) two separate ARs connected via bridge; and (c) two separate ARs with bridge and extended electrode region for connection.

concentration, hence no mechanical failure for the pre-strain up to 200% in both directions 1 and 2. Subsequently, a RP-DEA with the same configuration was fabricated to compare the force outputs (figure 3-1d). In this case, 7 rods were placed with a spacing of 5 mm on the DE film.

For life assessment, the sample size was scaled down with the total AR area of 20 mm $\times$ 20 mm as shown in (figures 3-1b and d). The RP-DEA had only three rods in order to simplify the fabrication process and yield more consistent samples. In addition, 3 AR configurations were used for the durability study. Figure 3-2a shows the conventional single AR configuration. Figure 3-2b shows multiple ARs with a gap of 1 mm from the rods. Figure 3-2b has the lead contact point inside the AR. Figure 3-2c is similar to figure 3-2a, but with an additional inactive electrode.

3.3.2 DEA fabrication

The dielectric elastomer used in this work was the adhesive acrylic film, VHB^{TM} 4910, from 3M (Maplewood, MN., USA). The electrode material was graphite

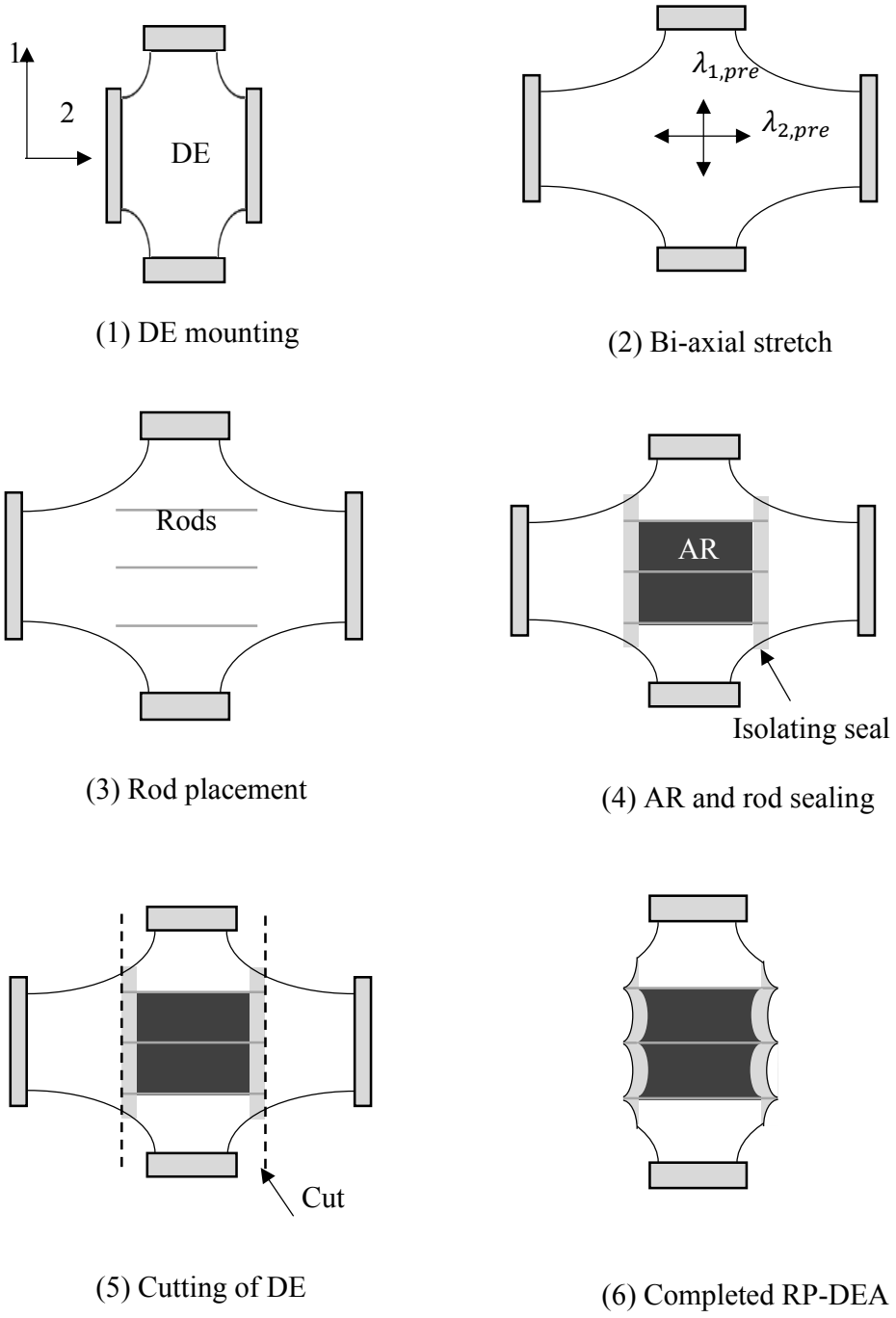

Figure 3-3: RP-DEA fabrication sequence.

powder. The powder-type electrode was used to ease the screen-printing electrode deposition. The graphite powder was mixed with ethanol prior to the deposition and brush-painted on the DE. The use of ethanol, which vaporized shortly after application, was to improve the coverage of the electrode on the DE. The tested samples were laser cut into the configured shapes. The fabrication sequence of the RP-DEA is presented in figure 3-3. The rods used had a diameter of 0.75 mm. They were bonded to the DE film on one side, and sealed by two slices on the other side after the electrode deposition. Such sealing prevented slip between the film and the rods; it also improved the isolation of the electrodes and prevented arcing around the edge. Moreover, because the rods were conductive, it was better to keep their ends sealed in the DE material.

3.3.3 Experimental setup and measurements

For the force measurements, the conventional DEA samples were configured as in figure 3-1. This layout was used to investigate the effect of bi-axial pre-loading conditions on the actuation force output. The samples were stretched with $\lambda_{1,pre} = 1.2$ fixed, and $\lambda_{2,pre}$ varied from 1.5 to 3 in steps of 0.05. A voltage of 7 kV was applied across each sample and 5 force measurements were taken at each point in both directions via the force sensors in the stretch system. The force output of the RP-DEAs was measured with the same setup, pre-strain and applied voltage, but only in direction 1.

For life assessment, the RP-DEAs under different AR configurations as in figure 3-2 were assessed. The assessed lifetime was defined as the time period from the voltage application to the detection of a breakdown failure. The AR configuration was optimised by firstly identifying the failure areas in a conventional RP-DEA and then dividing the AR into multiple regions to avoid weak areas in the structure, as shown in figure 3-2a, the experiments were undertaken over three different AR configurations:

Case 1 The RP-DEA with a single AR as in figure 3-2a, over 20 samples

Case 2 The RP-DEA with multiple ARs, which exclude the regions associated with rods and have in-AR lead contact as in figure 3-2b, over 20 samples

Case 3 The RP-DEA with multiple ARs and an off-AR lead contact as shown in figure 3-2c, over 10 samples

The DE samples were stretched as $\lambda_{1,pre} = 1.2$ and $\lambda_{2,pre} = 3$. The input voltage for all testing was set to be 7.5 kV, the critical voltage that the RP-DEA started to fail. For each sample, its lifetime was recorded.

A high voltage (HV) generator was used to amplify the input voltage (0-10 V) from a programmed system. The actual voltage output (0-15 kV) from the generator was monitored and fed back to detect any rapid voltage drop, which would be the result of short−circuiting hence failure of the DEA (figure 3-4b). The experimental layout is shown in figure 3-4a. The lead contacts to the electrodes were as shown in figure 3-5.

3.4 Results and discussion

3.4.1 Force measurement results

The force measurement results for the conventional DEA without any rods are shown in figure 3-6. The large force outputs and the quicker rising trend were found in direction 1 compared with direction 2. The maximum force outputs were $f_2 = 0.17$ N ($\pm$ 0.01 N) in direction 2 and $f_1 = 0.35$ N ($\pm$ 0.01 N) in direction 1 at the maximum pre-strain condition. The results indicate that large pre-strains in direction 2 increased the force outputs in both directions. Pre-strains in direction 2 were observed to be more effective in amplifying the force output in direction 1. An approximate linear relationship is seen between the force outputs and pre-strains in direction 2. The force output from the RP-DEA, which has pre-strain $\lambda_{2,pre} = 3$ only, is also shown in figure 3-6 for comparison.

It is recalled that equation (3.7) was derived from the equation of state for the DE material to describe the effect of bi-axial pre-strain on the actuation force outputs. Figure 3-6 indicates a good correlation between equation (3.7) and the measured actuation forces in both directions. Offsets between the theory and experimental data may be due to the migration of the electrodes on the DEA.

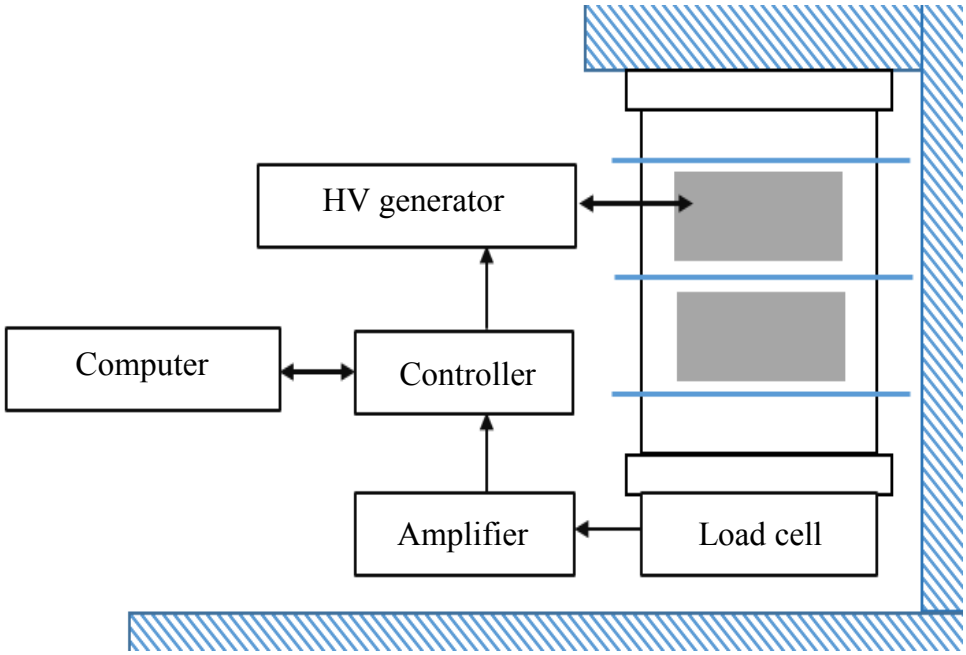

(a)

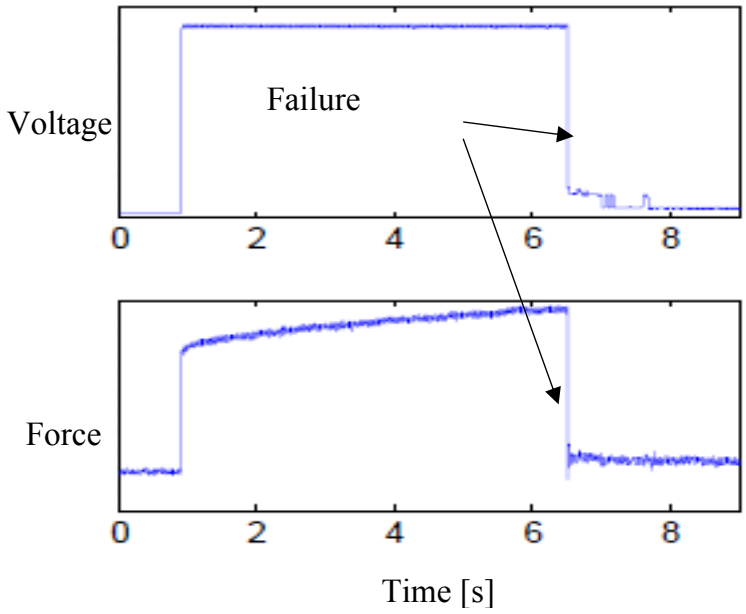

(b)

Figure 3-4: Experimental system: (a) test rig set-up; and (b) failure detection through voltage monitoring and force measurement.

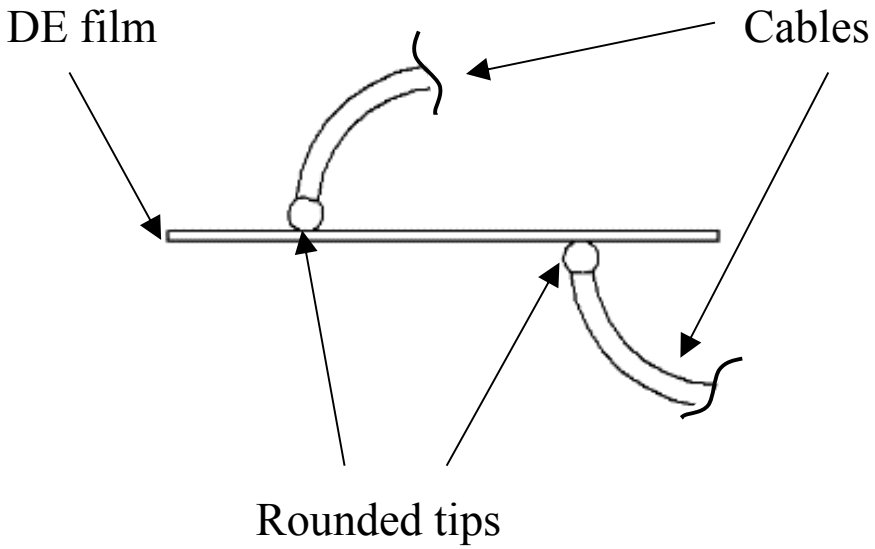

Figure 3-5: The lead contact method.

Although the electrode material was carefully repainted to both surfaces at each step before the activation, the quality of the re-application could be ensured only on the upper surface of the DEA. It was difficult to access and check the electrode conditions on the lower surface since the mounting condition was maintained for consistency of measurement. Furthermore, in equation (3.7), the permittivity of the material is assumed to be constant. Large deformation of the elastomer changes the geometries and arrangements of the polymeric molecule chains, which may potentially vary the electromechanical coupling behaviour of the material. In general, the derived correlation shows the potential for it to predict the actuation force output of the DEA structure in a biaxial loading condition. It can also be used to guide the prestrain configurations in a DEA design.

With the same pre-strains, $\lambda_{1,pre} = 1.2$ and $\lambda_{2,pre} = 3$, the force output of the RP-DEA with the rod configuration was measured to be $f_1 = 0.45$ N ($\pm$ 0.01 N) in direction 1. It is a higher force output compared with that of the conventional DEA with the same pre-strain, 0.32 N ($\pm$ 0.01 N). The extra force output is due to the motion constraint, as the rods play the role of both maintaining pre-strain and constraining electrode movement in the RP-DEA.

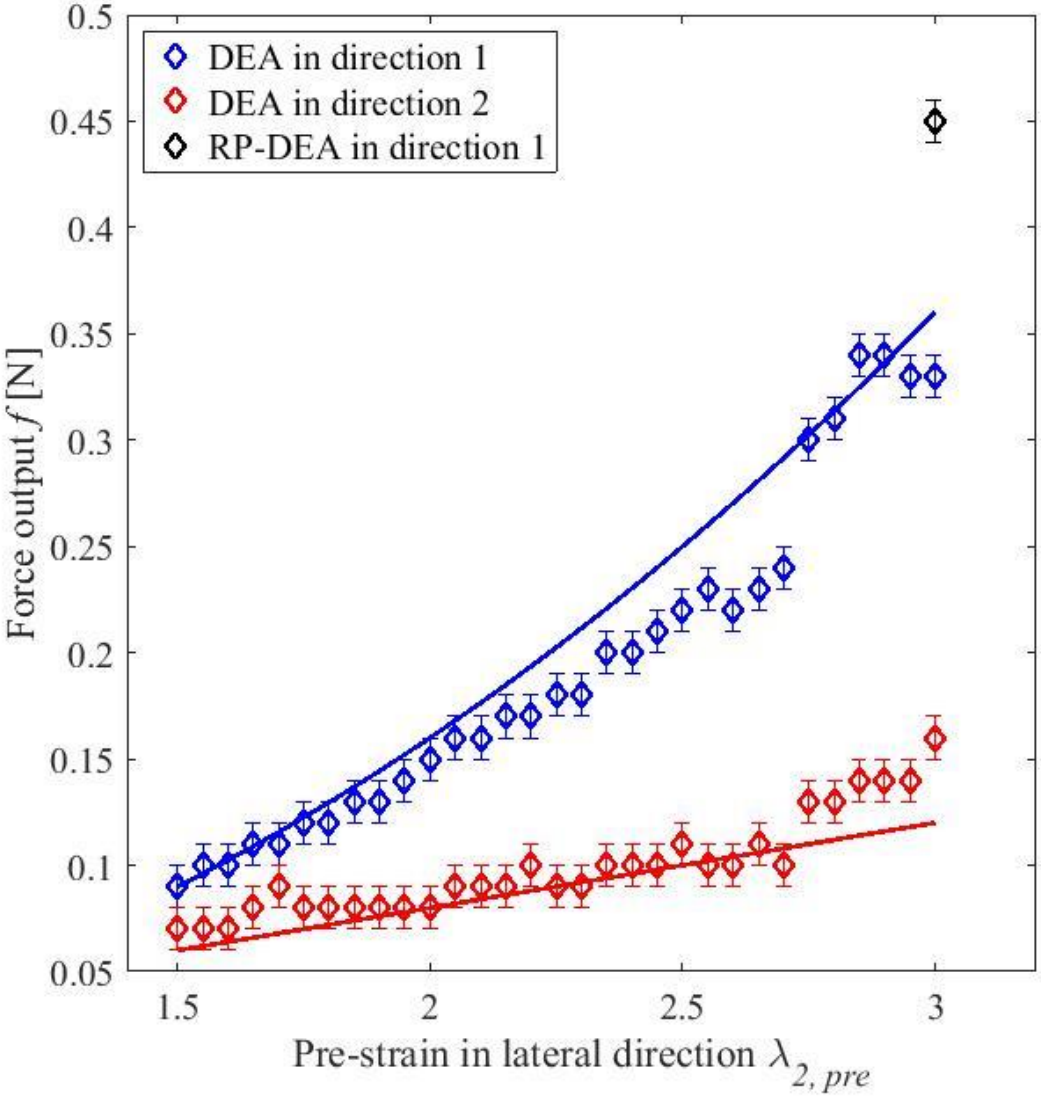

Figure 3-6: Force measurement results (diamonds) against correlation according to equation (3.7) (lines) in direction 1 (blue) and direction 2 (red).

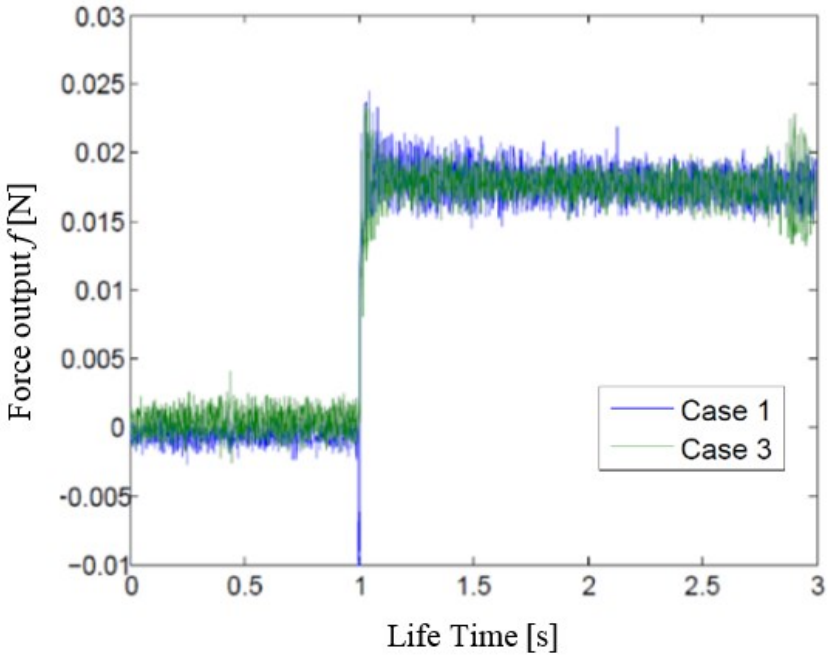

Figure 3-7: Comparing static force output in isometric loading with that from a step input voltage: RP-DEA with single AR and RP-DEA with multiple ARs.

In the durability study of the RP-DEA, the static force responses of the structure as in figure 3-1b were also measured to compare between Case 1 and Case 3. Five samples were measured for each case and the results are shown in figure 3-7. The force output of the RP-DEA with multi-ARs was found to be 6% less than the force output of the RP-DEA with a single AR. The reason is due to the decrease in the total area of the AR. However, the reduction in force output is considered to be small compared with the 20% reduction in the area of the AR. The narrow gaps between ARs may also slow down the spreading of charge over the AR during the charging phase, hence lead to the change in the dynamics of the RP-DEA. It would require further study to fully identify this effect.

3.4.2 Lifetime assessment results

The lifetime results for all samples are summarized in figure 3-8. For Case 1, the operating lifetimes varied significantly from 5 s to 120 s. Overall, 80% of the samples failed within 60 s and the average lifetime was 39 s. The standard deviation was evaluated as 33 s. For Case 2, the average operating lifetime of the structures was increased significantly to 202 s. However, the measured lifetime had broad range of variation, between 103 s and 240 s. The standard deviation was calculated as 51 s. For RP-DEAs in Case 3, all samples survived to the full test duration of 240 s. The applied voltage was then increased gradually until the structures failed. The failing input voltages were found to be consistently around 9.5 kV.

The failures in all three cases were recorded as shown in figure 3-9. In Case 1, 95% of failures (19 out of 20) occurred close to the rods (figure 3-9a), while 5% of the failures (1 out of 20) occurred around the lead contact point. This indicates the regions close to rods primarily cause the premature failure of the RP-DEA. The electrode deposition should avoid these weak regions for the sake of improving the durability. For the RP-DEAs in Case 2), the failures were found to be associated with the center of the AR (figure 3-9b), where the tip of the cable contacts the DE in order to connect to the power supply. In this case, because the weak regions were no longer activated, the average lifetime increased significantly compared with those in Case 1. The in-AR lead contact was found

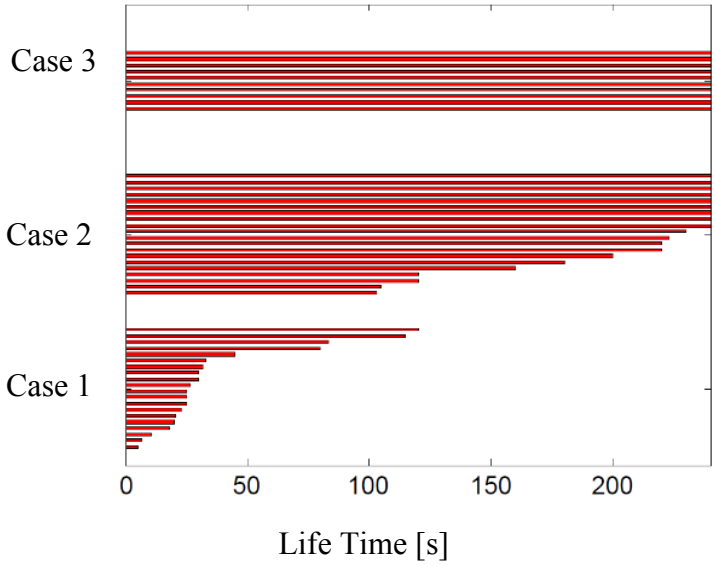

(a)

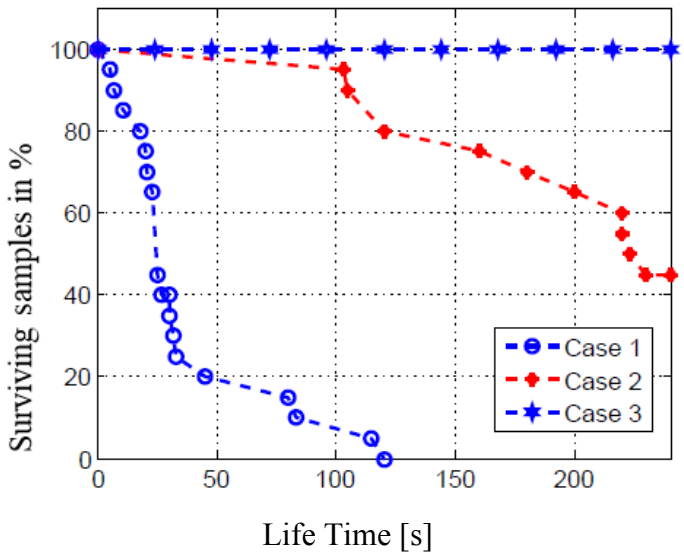

(b)

Figure 3-8: (a) Recorded lifetimes up to 240 s for RP-DEA with single AR (20 samples), with separate ARs (20 samples) and with separate ARs and off-AR contact (10 samples); and (b) accumulated surviving samples as a percentage.

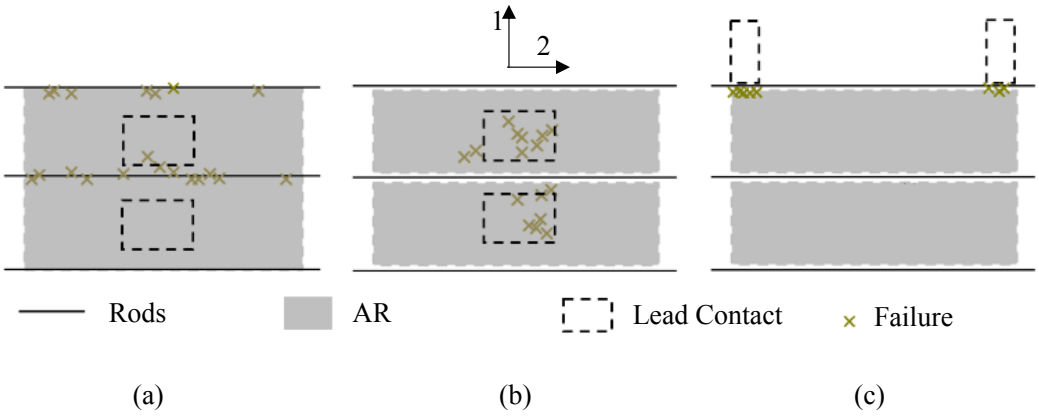

Figure 3-9: Recorded failure occurrence in RP-DEAs: (a) with single AR over 20 samples (Case 1); (b) with separate ARs over 16 samples (Case 2); and (c) with separate ARs and optimised connection over 10 samples (Case 3).

to be the secondary cause that also causes the premature failure. For the RP-DEAs in Case 3, as both sources of failure were removed from the structure, all samples survived through the full duration of the life-assessment (4 min).

3.4.3 Finite Element (FE) simulation configuration

In order to better understand the primary source of failure, the weak regions in the structure, the deformation of the RP-DEA was evaluated by 2D FE simulation. This was implemented using the four-noded rectangular element, Q4, in MATLAB. The elastomer is hyperelastic and if subjected to large deformations ($\lambda_1 = 3$, $\lambda_2 = 1.2$), the FE analysis is nonlinear due to:

C1. The solid is anisotropic due to bi-axial loading

C2. The elastic moduli, $E_i(\lambda_1, \lambda_2)$ and $E_2(\lambda_1, \lambda_2)$, of the DE in the in-plane directions become functions of strains instead of remaining at constant Y

The nonlinear analysis was achieved by setting $\lambda_2 = 1$ as the initial boundary condition, and splitting the large deformation, $\lambda_1 = 3$, into 10 small deformation steps, $\Delta\lambda_1 = 0.2$, from $\lambda_1 = 1$ to $\lambda_1 = 3$. The 11^{th} step is applied to strain the

DE with $\lambda_2 = 1.2$. Hence, the FE analysis for the j^{th} $(j = 1, 2, \ldots, 11)$ step can be considered to be linear with respect to the elastic moduli, E_{1-j} and E_{2-j}, as:

$$\{\boldsymbol{d}_j, \boldsymbol{\sigma}_j, \boldsymbol{\epsilon}_j\} = f_{FEA}(E_{1-j}(\lambda_{1-j}, \lambda_{2-j}), E_{2-j}(\lambda_{1-j}, \lambda_{2-j}), \boldsymbol{p}_j) \tag{3.8}$$

$$\lambda_{1-j} = 1 + \Delta\lambda_1(j-1) \tag{3.9}$$

$$\lambda_{2-j} = 1 \tag{3.10}$$

where $\boldsymbol{d}_j$ is the vector of nodal displacements after current step, j, $\boldsymbol{\sigma}_j$,$\boldsymbol{\epsilon}_j$ are the corresponding vectors of the nodal stress and strain components, and $\boldsymbol{p}_j$ is the vector of nodal coordinates that describes the shape of object before the current step. It is defined as:

$$\boldsymbol{p}_i = \boldsymbol{p}_0 + \textstyle\sum_{n=1}^{i-1} \boldsymbol{d}_n \tag{3.11}$$

where $\boldsymbol{p}_0$ is the vector of nodal coordinates for the object in the undeformed state, and $\sum_{n=1}^{i-1} d_n$ is the summation of all nodal displacements from previously simulated steps. The final stress and strain distributions of the object, σ_{final} and $\boldsymbol{\epsilon}_{final}$, are evaluated in the same way as for total deformation in equation (3.11):

$$\begin{aligned} \boldsymbol{\sigma}_{final} &= \sum_{n=1}^{10} \boldsymbol{\sigma}_n \\ \boldsymbol{\epsilon}_{final} &= \sum_{n=1}^{10} \boldsymbol{\epsilon}_n \end{aligned} \tag{3.12}$$

For the large deformation up to $\lambda = 3$, the predictive stressstrain models of elastomer that is proposed by Carpi and Gei [187] was used to describe such nonlinear material behaviour:

$$W = \frac{2}{3}^3 Y({\lambda_1}^{3/2} + {\lambda_2}^{3/2} + {\lambda_3}^{3/2} - 3) \tag{3.13}$$

The model is based on the one-term Ogden energy density function, depending uniquely on the Youngs modulus, Y, which is appropriate for analysis up to the inflection (flex) point of the elastomer in nominal stressstrain correlation. For the VHB$^{\text{TM}}$ 4910 DE acrylic film, $\lambda_{flex} = 3.3$. The nominal stresses can be obtained by differentiating equation (3.13) to yield the expressions:

$$\begin{aligned} \sigma_1 &= \frac{4}{9} Y(\lambda_1^{1/2} - \lambda_1^{-5/2}\lambda_2^{-3/2}) \\ \sigma_2 &= \frac{4}{9} Y(\lambda_2^{1/2} - \lambda_2^{-5/2}\lambda_1^{-3/2}) \end{aligned} \tag{3.14}$$

The elastic moduli can be solved by evaluating $\partial\sigma_i/\partial\lambda_i$ to give:

$$\begin{aligned} E_1(\lambda_1, \lambda_2) &= \frac{2}{9} Y\lambda_1^{-1/2} + \frac{10}{9} Y\lambda_1^{-7/2}\lambda_2^{-3/2} \\ E_2(\lambda_1, \lambda_2) &= \frac{2}{9} Y\lambda_2^{-1/2} + \frac{10}{9} Y\lambda_2^{-7/2}\lambda_1^{-3/2} \end{aligned} \tag{3.15}$$

This then gives the complete stress-strain relation. The incompressibility gives the shear modulus as $G = Y/3$, the modified Hookes law for this 2D finite element simulation can be expressed in matrix form as:

$$\begin{bmatrix} \epsilon_{11} \\ \epsilon_{22} \\ 2\epsilon_{12} \end{bmatrix} = \begin{bmatrix} \dfrac{1}{E_1(\lambda_1, \lambda_2)} & \dfrac{-v}{E_2(\lambda_1, \lambda_2)} & 0 \\ \dfrac{-v}{E_1(\lambda_1, \lambda_2)} & \dfrac{1}{E_2(\lambda_1, \lambda_2)} & 0 \\ 0 & 0 & \dfrac{3}{Y} \end{bmatrix} \begin{bmatrix} \sigma_{11} \\ \sigma_{22} \\ \sigma_{12} \end{bmatrix} \tag{3.16}$$

where v is the Poisson ratio. Figure 3-10 presents the pre-inflection stress-strain relationship of the elastomer when subjected to large deformation, as appropriate to equation (3.15). The elastomer becomes softer as it is stretched further in both

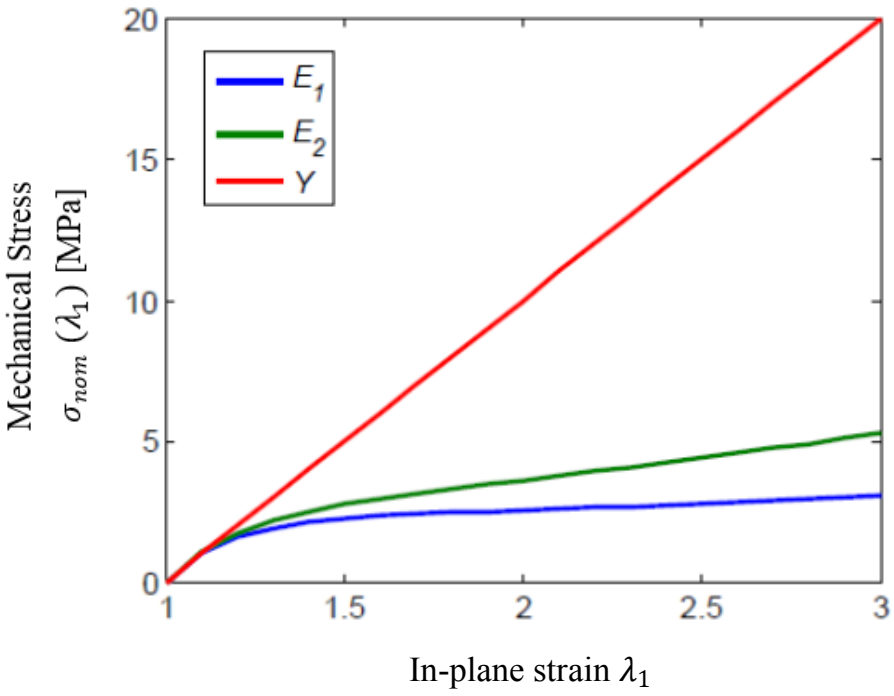

Figure 3-10: Comparison between the Youngs Modulus of the elastomer ($Y = 0.1$ GPa) and the evaluated elastic modulii E_1, E_2 from equation (3.15) (taking $\lambda_2 = 1$) for both in-plane directions. The actual elastic moduli in both directions decrease as the elastomer undergoes large deformation. The elastomer becomes anisotropic under bi-axial loading.

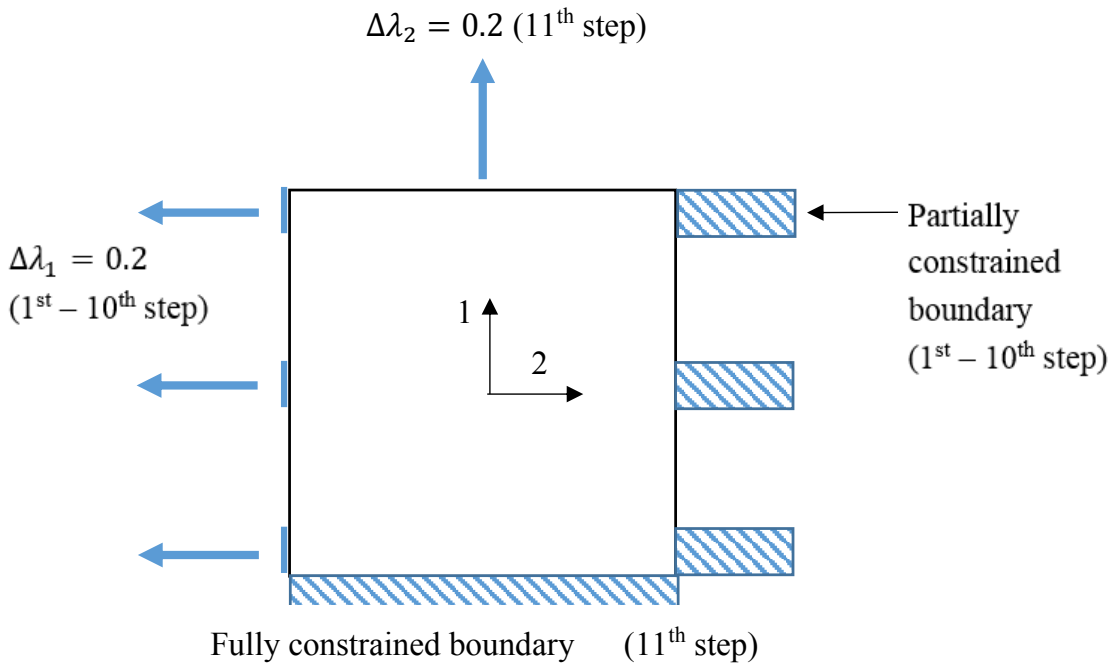

Figure 3-11: Boundary condition configurations for finite element simulations over 11 steps.

directions. The relaxations in both elastic moduli are taken over the discrete steps in the simulation.

Because the simulation is in 2D, it does not generate the compressive strain distribution in the direction of thickness directly. It is reasonable to represent the thickness strain ϵ_{33} as:

$$\epsilon_{33} = \frac{1}{(1+\epsilon_{11})(1+\epsilon_{22})} \tag{3.17}$$

The applied boundary conditions were configured as shown in figure 3-11. The simulated DE was set in a square, which corresponds to the AR as in figure 3-2. The sub-strain $\Delta\lambda_1$ was applied on the three nodal sets in the left hand side edge of the square from the 1st to 10th steps of the simulation. The three corresponding nodal sets in the right hand side edge were fully constrained. This simulates the applied pre-strain that is held by the rod in direction 2, which was 200% in the

experiment. The sub-strain $\Delta\lambda_2$ was applied to the upper edge of the square, and the lower edge was fully constrained for the 11th step of the simulation. This simulates the 20% pre-strain from the experiment in direction 1.

The quasi-static linear FE simulation used here is to only demonstrate the potential non-uniform thickness distribution of the DE in the RP-DEA. The employed material model does not include the full viscoelasticity of hyperelastic elastomers, and the result only indicates the relative thick and thin regions across the structure. It is insufficient to provide the exact estimation on the deformation.

3.4.4 FE simulation results

The simulated results for RP-DEA are presented in figure 3-12. It shows the DE to be deformed non-uniformly in the RP-DEA. In general, the thickness of the film decreases as it moves from the edge to the centre in direction 2. The three thinnest regions with $\epsilon_{33} = -17\%$ are found around the rods, which correlate to the weak region that causes the premature failure shown in figure 3-8. When the RP-DEA has the single AR as in Figure 3-12a, the AR covers all these thinnest regions. When the RP-DEA is configured with multi-ARs, the ARs only cover the relatively thin regions with $\epsilon_{33} > -15\%$. It hence avoids the resultant premature failure. In figure 3-13, the AR of the RP-DEA, as in figure 3-9, were evenly divided into the left, centre and right regions in direction 2. This evaluation suggests that in Case 1, 35% of the failures occurred in the left region; 50% of the failures occurred in the centre; 15% of the failures occurred in the right region. It is in agreement with the simulation, where the weak regions around the rods cover a larger area in the centre region compared with the side regions. More failures would therefore be expected to occur in the centre region of the AR.

Considering the three potential sources of failure of the DEA: (I) dielectric strength; (II) mechanical strength; and (III) pull-in instability, the most likely failure mode in the RP-DEA is the dielectric strength as explained below:

I Dielectric strength failure: The failure occurs because the resultant local electrical field exceeds the dielectric strength of the film. A 7.5 kV actuation voltage was found to be close to the breakdown voltage of VHB$^{\text{TM}}$ 4910 in

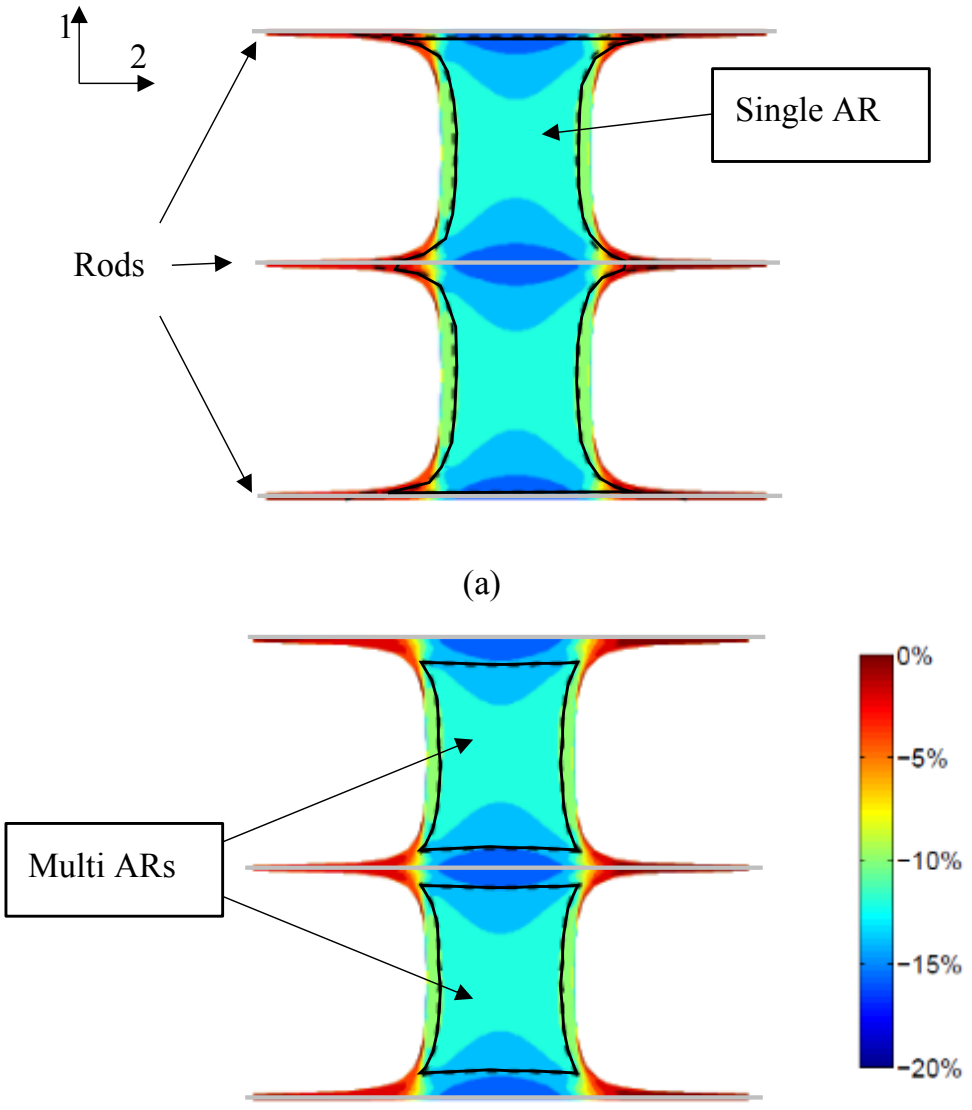

Figure 3-12: Thickness strain distribution of a deformed RP-DEA from 2D finite element simulation. The thickness is evaluated from in-plane residual strains ϵ_{11}, ϵ_{22} according to equation (3.17) (h=0.1 mm).

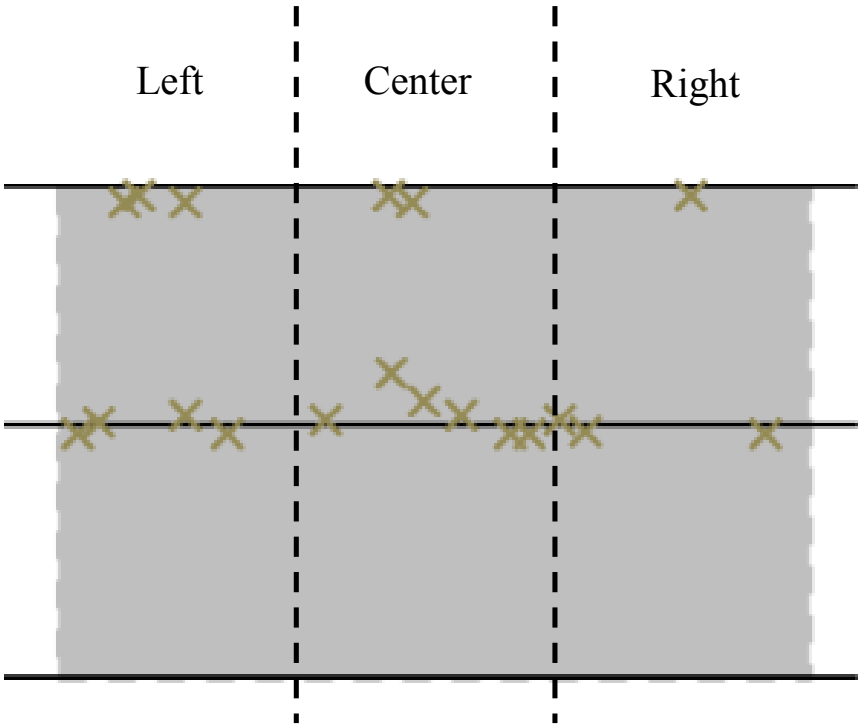

Figure 3-13: Boundary condition configurations for finite element simulations over 11 steps.

agreement with Plantes work at the same pre-strain condition ($\lambda_{1,pre} = 1.2$, $\lambda_{2,pre} = 3$) [57]. Because the DE in the RP-DEA is deformed non-uniformly, the thinnest regions in the film or weak regions are close to the dielectric limit. All other relatively thicker regions have the smaller values of local pre-strain and higher breakdown voltages.

II Mechanical strength failure: For VHB^{TM} 4910, it has been shown that the film can be stretched up to the pre-strain of 600% [57], which is well beyond the pre-strain configuration in this work. Therefore the mechanical strength is unlikely to be a source of failure.

III Pull-in instability failure: This failure mode of the RP-DEA is less likely because: (1) no wrinkling was observed prior to the failure; and (2) the RP-DEAs were pre-strained with high stretch rate (0.01 s^{-1}). In this case, the viscosity stiffens the elastomer and makes it resistant against the pull-in instability [57].

3.5 Conclusions

This chapter concludes that significant performance enhancement can be achieved using a RP-DEA. An investigation has been undertaken to study the effect of bi-axial pre-loading on the force output of a conventional DEA, compared with that from the new RP-DEA. The derived correlation between the pre-strain and the force output of the DEA was found to fit the experimental data well, covering pre-strain variations up to 200%. The RP-DEA generated larger force by gaining advantages from both pre-strain and motion constraint.

The first RP-DEA design was found to have a short operating lifetime with failure due to its limited dielectric strength. Two sources of failure are identified in this work. The primary failure source is the non-uniform deformation of the DE in the RP-DEA. It creates weak regions having low thickness close to the rods, which locally are vulnerable to breakdown voltages. The secondary cause is the in-AR lead contact. The tips that contact the DE have better conductivity than the electrode material, which may concentrate charge and lead to excessive

local electrical fields. The in-AR contact is found to have lower impact on the durability of the RP-DEA compared with the primary weak region. Both sources of failure were suppressed by optimising the AR configuration. The results show that this approach stabilizes the RP-DEA to avoid failure due to limited dielectric strength and dramatically improves the durability of the RP-DEA. The results also show that the AR optimization led only to a minor reduction in force output.

Further work is suggested in the life assessment of the RP-DEA with non-conductive rods to assess fully the influence of rod conductivity. The simulation model could be further improved by performing a single continuous simulation, rather than the discrete steps in this chapter. A locally defined DE elastic modulus that varies with non-uniform deformation would also be more representative in the model. Moreover, since the current model only simulates the mechanical deformation, electro-mechanical coupling effects should be included to show the non-uniform distribution of electric fields across the ARs.

Chapter 4

Dielectric elastomer actuator modelling using higher order material characteristics

This chapter addresses the research gap in dynamic modelling of DEs and DE actuators as identified from Section 2.2. It demonstrates that the accuracy of modelling the viscoelastic characteristics of the commonly used dielectric elastomer (DE), polyacrylate VHB^{TM} 4910, can be improved significantly by adding additional spring-damper combinations into a conventional Kelvin-Voigt model. The effect of the key parameters on the higher order system dynamics is elaborated, which is used to guide the parameter identification of the model. The increased effectiveness of such higher order models is demonstrated using three experiments; (a) mechanical loading of a stacked sample over 0.01-5 Hz with strain variations up to 50%; (b) mechanical loading of a single-layer sample over 1-100 Hz with strain variations up to 10%; and (c) electrical actuation of a single-layer sample over 1-100 Hz using driving voltages up to 7 kV. An elastic silicone sample was also tested and compared with the polyacrylate sample to show that viscoelastic properties have higher elastic modulus and give rise to a significantly slower dynamic deformation response in the frequency domain. The proposed higher order model will have potential in the model-based control of DE actua-

tion as it provides better accuracy in modelling the characteristics of a viscoelastic DE.

4.1 Existing elastomer models

The actual deformation and dynamic force output of a DEA depend on the viscoelastic properties of the elastomer, which are often based on spring-damper rheological models. The material model has been developed into the Gent model [115], the Ogden model [114] and the neo-Hookean model [117] to include nonlinearity in both elastic and viscous parameterisation of the elastomer. Hong [127] developed a general eld theory for the coupled electro-viscoelastic behaviour of dielectric elastomers, by integrating a formulated theory of deformable dielectrics into a framework of non-equilibrium thermodynamics for continua. The theory has significant flexibility for various materials. Plante et al. [77] include a rate-dependent effect in the material model for use in failure analysis. Hackel et al. [188] present a fully integrated DEA model that includes the electrostatic properties of electrical circuits. In the energy harvesting field, Xiaofeng et al. [120] analyse the DE-based energy harvester with the Gent and neo-Hookean models for an understanding of how viscoelasticity affects the energy conversion and dissipation. Li et al. [121] modelled the energy harvesting of a DEA in an inhomogeneous field using the neo-Hookean model. In the field of tuneable oscillators, Fox and Goulbourne [122] examined the dynamic behaviour of an axisymmetric DE membrane resonator based on the Ogden model, while Zhou et al. [123] studied viscoelastic and hyperelastic models of the DE. The latter work showed that neglecting the viscoelastic behaviour of the DE may lead to significant errors in the dynamic response of the oscillator. The resonant behaviour of a DE membrane mounted on a rigid ring was studied by Zhu et al. [124] with the neo-Hookean model. Yang et al. [126] adopted linear theories to investigate the material viscoelasticity of DEs under small deformations.

Further, Berselli et al. [125] simulated a constant-force dielectric elastomer actuator with a hyperelastic model that is based on a bond graph formalisation. Hossain et al. [129] proposed a modified Bergstrom-Boyce viscoelastic model

with a finite strain linear evolution law to simulate the response of VHB^{TM} 4910 polymer in various step-based standard testing. Wissler et al. [132] developed a finite element analysis approach for describing VHB^{TM} 4910-based circular actuator that undergoes large strain strains. Wang et al. [133] developed a finite element analysis approach to investigate the role of viscoelasticity in the instability of the soft dielectrics through effects such as pull-in, wrinkling, electrocreasing and electrocavitation. Lochmatter et al. [103] used a hyper-viscoelastic model to demonstrate the unstable actuation behaviour in long-term actuation of a planar DEA. Zhang et al. [189] used a proposed constitutive model of the DEA to modify the input voltage in order to eliminate the creeping behaviour in a circular DEA. Choi et al. [32] developed a biomimetic DEA, modelled as a series of lumped masses and with control based on the model.

While most DEA models have been developed to describe the nonlinear viscoelastic behaviour of the elastomer, typically based on first-order parameterisation that contains one spring and one spring-damper, few simulate DEA actuation with complete accuracy over useful frequency ranges. Physically, the elastomer contains numerous molecular segments oriented in different directions, which have dissipation properties. The relaxation of each segment may not occur simultaneously, hence the first-order material model is an obvious approximation. While the viscoelasticity of a DE has a significant influence on the performance of actuators, sensors and energy harvesters, the dynamics of these DEA models have received only limited attention in the literature.

This chapter studies higher order material models which contain multiple spring-damper combinations for more accurate representation of the dynamics of a highly viscous polymer such as polyacrylate. The system dynamics of the model and its correlation to the system parameters are studied and the advantages of having higher order in the material model are elucidated. Three experiments are considered to measure the dynamics of polyacrylate in mechanical loading and electric actuation. The validation of the proposed models is presented and compared with a conventional Kelvin-Voigt model. An elastic silicone was also tested to show how the viscoelastic polyacrylate characteristics differ in terms of dynamic response.

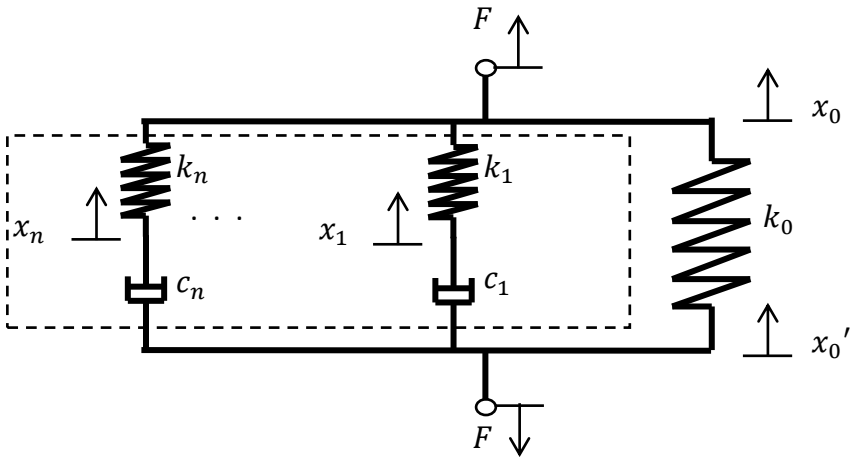

Figure 4-1: nth−order viscoelastic solid model of DE that contains n sets of spring−damper combinations and a main spring of stiffness k_0.

4.2 Theory

4.2.1 Higher order spring-damper rheological model under mechanical loading

Consider a Maxwell-Wiechert model for viscoelastic DE as shown in 4-1. It generalizes the spring-damper rheological model by having multiple sets of spring-damper combinations, which defines the model order. Hence the commonly used Kelvin−Voigt model that contains only one spring-damper combination is referred as a first-order model ($n = 1$). When an external force F is applied to the DE, the system deforms and the equations of motion for the nth-order model are and associated parameters are explained in table 4.1.

$$\begin{cases} k_0(x_0 - x_0') + \sum_{i=1}^{n} k_i(x_0 - x_i) = F \\ c_1(\dot{x}_1 - \dot{x}_0') + k_1(x_1 - x_0) = 0 \\ \vdots \\ c_n(\dot{x}_n - \dot{x}_0') + k_n(x_n - x_0) = 0 \end{cases} \tag{4.1}$$

Table 4.1: Parameters for the system as in figure 4-1 and equation (4.1).

Parameters	Descriptions
n	Number of spring-damper subsystems ($n > 0$)
x_0,x_0'	Displacements of both ends of the system
x_n	Displacement in the spring-damper combination
k_0	Stiffness of the main spring
k_n, c_n	Stiffness of the main spring
F	Applied force

The generic model is simplified ($\dot{x}_0' = x_0' = 0$) to match an experimental setup of mechanical loading, where the DE is loaded on the top end and clamped onto a load cell for force measurement on the bottom end. Equation (4.1) therefore becomes

$$\begin{cases} k_0 x_0 + \sum_{i=1}^{n} k_i (x_0 - x_i) = F \\ c_1 \dot{x}_1 + k_1 (x_1 - x_0) = 0 \\ \vdots \\ c_n \dot{x}_n + k_n (x_n - x_0) = 0 \end{cases} \tag{4.2}$$

Assuming an input displacement x_0 and force F as the output, equation (4.2) can be expressed in state-space form as

$$\begin{cases} \dot{\boldsymbol{x}} = \boldsymbol{A}\boldsymbol{x} + \boldsymbol{B}x_0 \\ \boldsymbol{F} = \boldsymbol{C}\boldsymbol{x} + \boldsymbol{D}x_0 \end{cases} \tag{4.3}$$

$$\boldsymbol{x} = [x_1 \quad x_2 \quad \dots \quad x_n]^T$$

$$\boldsymbol{A} = diag[-\frac{k_1}{c_1}, \quad -\frac{k_2}{c_2}, \quad \dots, \quad -\frac{k_n}{c_n}]$$

$$\boldsymbol{B} = [\frac{k_1}{c_1}, \quad \frac{k_2}{c_2}, \quad \dots, \quad \frac{k_n}{c_n}]^T, \boldsymbol{C} = [-k_1 \quad -k_2 \quad \dots \quad -k_n], \boldsymbol{D} = \sum_{i=1}^{n} k_i$$

4.2.2 Higher order spring-damper rheological model under electrical actuation

Actuation of a DE requires electrodes to cover an Active Region (AR) on the DE surface. This enables a voltage to be applied across the DE material causing it to expand under Maxwell pressure. In the system model, the actuation force generated is denoted by F_A. The set of equations (4.2) are modified to

$$\begin{cases} c_1(\dot{x}_1 - \dot{x}_0') + k_1(x_1 - x_0) = 0 \\ \vdots \\ c_n(\dot{x}_n - \dot{x}_0') + k_n(x_n - x_0) = 0 \\ \sum_{i=1}^{n} c_i(\dot{x}_0' - \dot{x}_i) + k_0(x_0' - x_0) + F + F_A = 0 \end{cases} \tag{4.4}$$

Taking the constraint in the experimental setup as $\dot{x}_0' = x_0' = 0$, equation (4) simplifies to

$$\begin{cases} c_1\dot{x}_1 + k_1(x_1 - x_0) = 0 \\ \vdots \\ c_n\dot{x}_n + k_n(x_n - x_0) = 0 \\ \sum_{i=1}^{n} c_i\dot{x}_i + k_0x_0 + F_A = F \end{cases} \tag{4.5}$$

Equation (4.5) can be therefore presented in the state space form as

$$\begin{cases} \dot{\boldsymbol{x}} = \boldsymbol{A}\boldsymbol{x} + \boldsymbol{B}F_A \\ \boldsymbol{F} = \boldsymbol{C}\boldsymbol{x} + \boldsymbol{D}F_A \end{cases} \tag{4.6}$$

$$\boldsymbol{A} = \begin{bmatrix} 1 & -\dfrac{k_1}{c_1} & 0 & \dots & 0 \\ \vdots & & & \ddots & \\ 1 & 0 & \dots & 0 & -\dfrac{k_n}{c_n} \end{bmatrix}$$

$$\boldsymbol{B} = [0 \qquad 0]^T$$

$$\boldsymbol{C} = [\textstyle\sum_{i=1}^{n} k_i \quad -k_1 \qquad -k_n],\ D = 1,\ \boldsymbol{x} = [x_0 \quad x_1 \qquad x_n)]^T$$

Under uniaxial loading, when an external stress θ_1 and electric field E are applied to the DE, the equation of the state gives the stress in direction 1 as ([122])

$$\theta_1 + \varepsilon_r \varepsilon_0 E^2 = \lambda_1 \frac{\partial W(\lambda_1, \lambda_2, \lambda_3)}{\partial \lambda_1} \tag{4.7}$$

where $W(\lambda_1, \lambda_2, \lambda_3)$ is the free-energy density function, λ_1, λ_2 and λ_3 are the pre-strains in the three orthogonal directions. Taking $E = \dfrac{V}{z}$, the actuation force F_A is derived as

$$F_A = \theta_1 w_{AR} z = \frac{w_{AR}}{z} \varepsilon_r \varepsilon_0 V^2 \tag{4.8}$$

where V is the applied voltage, ε_0 is the dielectric permittivity in a vacuum, ε_r is the relative dielectric permittivity of the DE, w_{AR} is the width of the AR region and z is the thickness of the DE.

4.2.3 Dynamics of the first-order model

To understand fully the benefits of having a higher order model, it is important to know the influence of the springs and dampers on the system dynamics in the first order case. Given a sinusoidal displacement input as

$$x_0(t) = X_0 \sin \omega t \tag{4.9}$$

the steady state dynamic force will have the form

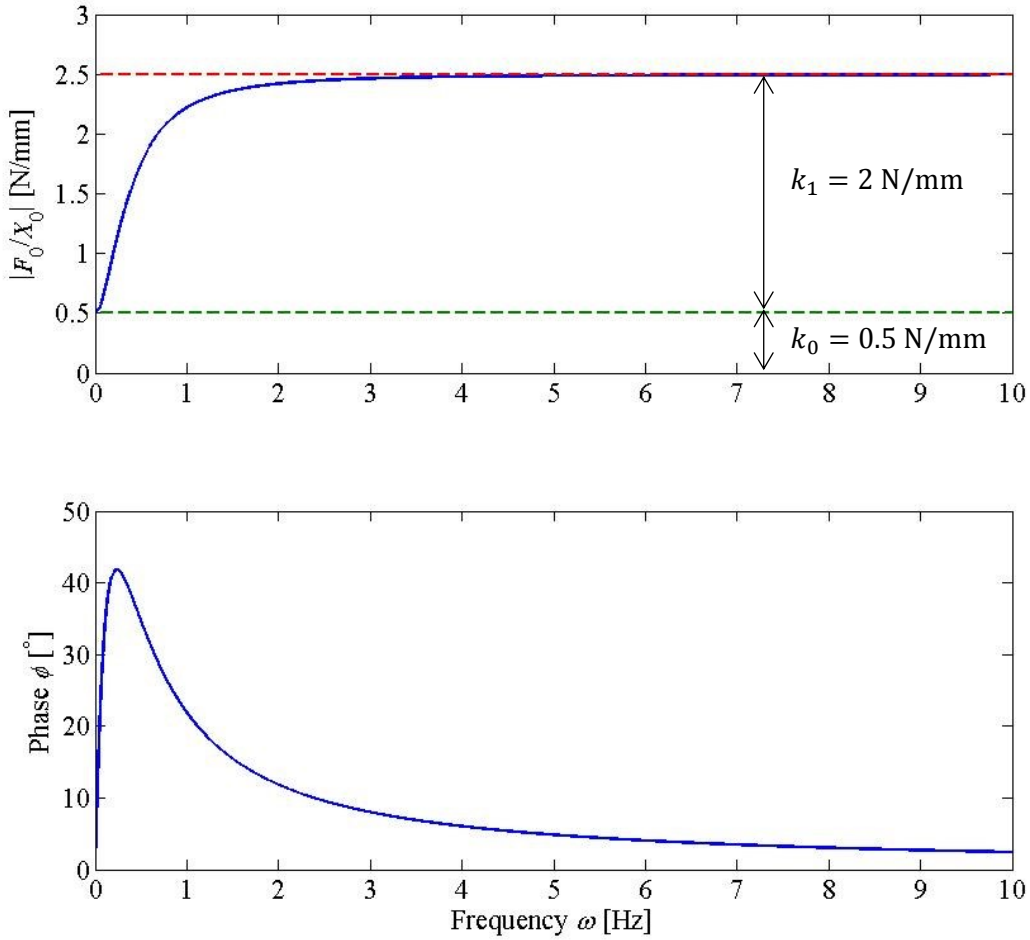

Figure 4-2: Schematic system dynamics of an example first-order model with $k_0 = 0.5$ N/mm, $k_1 = 2$ N/mm and $c_1 = 0.6$ N·s/mm.

$$F(t) = F_0 \sin(\omega t + \phi) \tag{4.10}$$

where ω is the operating frequency and ϕ is the phase. The dynamic response of a typical first-order model ($n = 1$) is shown in figure 4-2. At very low operating frequencies ($\omega \to 0$), the damper c_1 isolates the spring k_1 and the system is approximated by the spring k_0. At relatively high operating frequencies ($\omega \to 45$ rad/s), the damper acts as a strut. The system is therefore approximated by two springs in parallel, $k_0 + k_1$, defining the high frequency asymptotic characteristic. Over the frequency range between these two points, the dynamic stiffness of the system changes from k_0 to $k_0 + k_1$ and the frequency rate of transition depends on the damper c_1. Figure 4-2 also shows the phase of the first-order model. The curve rises rapidly and reaches the peak at the frequency where the dynamic stiffness curve has the highest rate of change. It then decreases gradually to zero.

4.2.4 Effect of having higher order

Now consider a second-order model that contains one main spring and two sets of spring-damper parallel combinations ($n = 2$). Given the same sinusoidal displacement input as in equation (4.9), the dynamic stiffness and phase are shown in figure 3. The dynamic stiffness starts at k_0 and high frequency asymptote is $k_0 + k_1 + k_2$. The transition depends on c_1 and c_2. The phase curve has monotonic rise and a two-stage decrement. In comparison with the first-order model of figure 4-3, the second-order model allows more versatile definition of the dynamic stiffness and phase over the frequency range. Given equations (4.9) and (4.10), in the Laplace transform domain, the dynamic stiffness is given by

$$k(s) = \frac{F_0}{X_0} = k_0 + (k_1 - \frac{1}{c_1 s + k_1}) + (k_2 - \frac{1}{c_2 s + k_2}) \tag{4.11}$$

Setting $s = j\omega$ gives the frequency dependence of the stiffness in complex form. It is therefore evident that

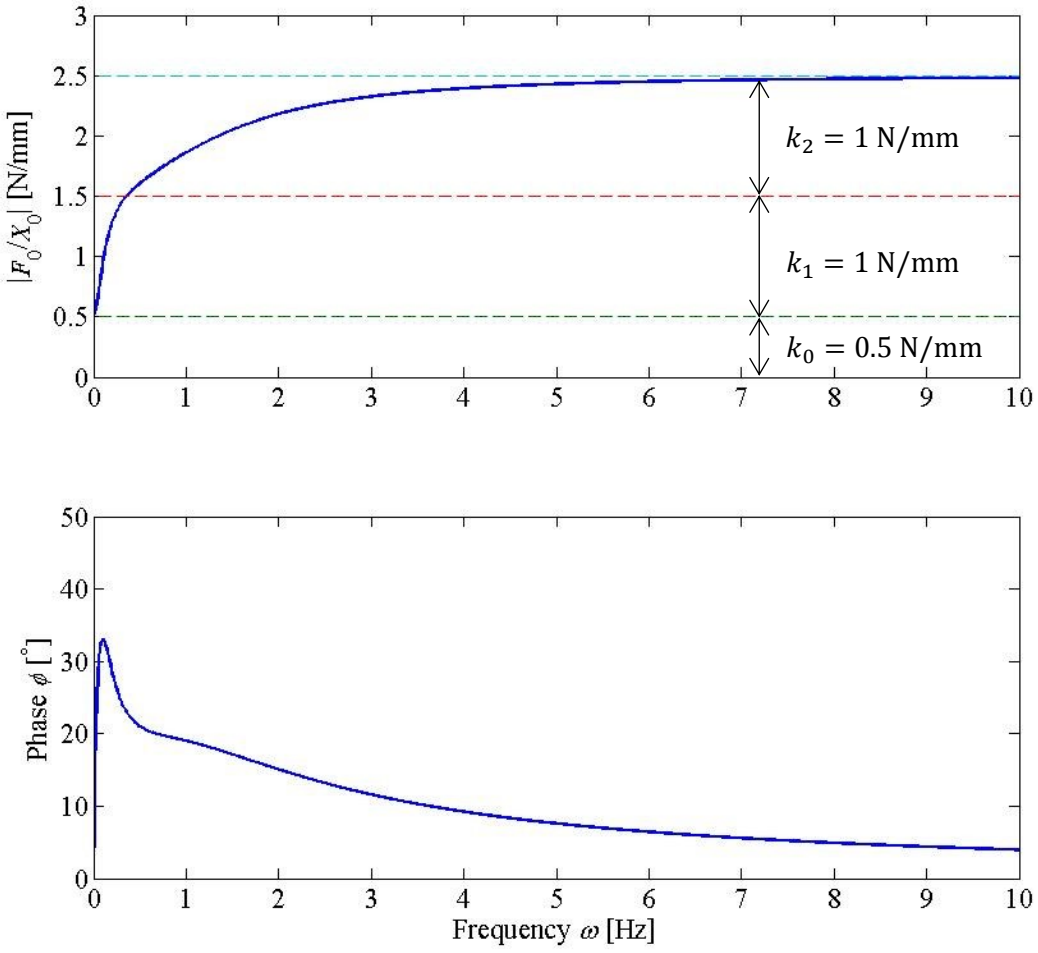

Figure 4-3: Schematic system dynamics of an example second-order model with ($k_0 = 0.5$ N/mm, $k_1 = k_2 = 1$ N/mm, $c_1 = 1$ N·s/mm and $c_2 = 0.1$ N·s/mm).

$$\begin{cases} |k(j\omega)| \neq |A_1| + |A_2| + |A_3| \\ \arg(k(j\omega)) \neq \arg(A_1) + \arg(A_2) + \arg(A_3) \end{cases} \tag{4.12}$$

where

$$A_1 = k_0, A_2 = k_1 - \frac{1}{(jc_1\omega + k_1)}, A_3 = k_2 - \frac{1}{(jc_2\omega + k_2)} \tag{4.13}$$

The inequalities of equation (4.12) show that the dynamics of a second-order model are not simply a superposition of the individual parallel elements in equation (4.13), therefore having important implications when identifying parameters for the model.

4.2.5 Parameter identification

The process of parameter identification for a first-order model could be relatively straightforward. Given a measured dynamic stiffness characteristic, the lower and higher frequency values could be set to k_0 and $k_0 + k_1$, respectively. The damper rate, c_1, then be adjusted to give the best fit for the transition between the lower and higher frequency values.

In higher order models ($n \geq 2$), the parameter identification is more difficult because the spring-damper combinations are not simple superpositions (see equation (4.12)), hence the fitting cannot be a sequential process for each parameter. Hence the scheme of figure 4 was formulated to include an iterative procedure to establish the higher order system parameters. The errors of the fitted model compared with an experimental characteristic are defined in terms of magnitude and phase by

$$\begin{cases} \epsilon_{mag} = \overset{mean}{\omega} \; ||k_{sim}| - |k_{exp}|| \\ \epsilon_{phase} = \overset{mean}{\omega} \; |\phi_{sim} - \phi_{exp}| \end{cases} \tag{4.14}$$

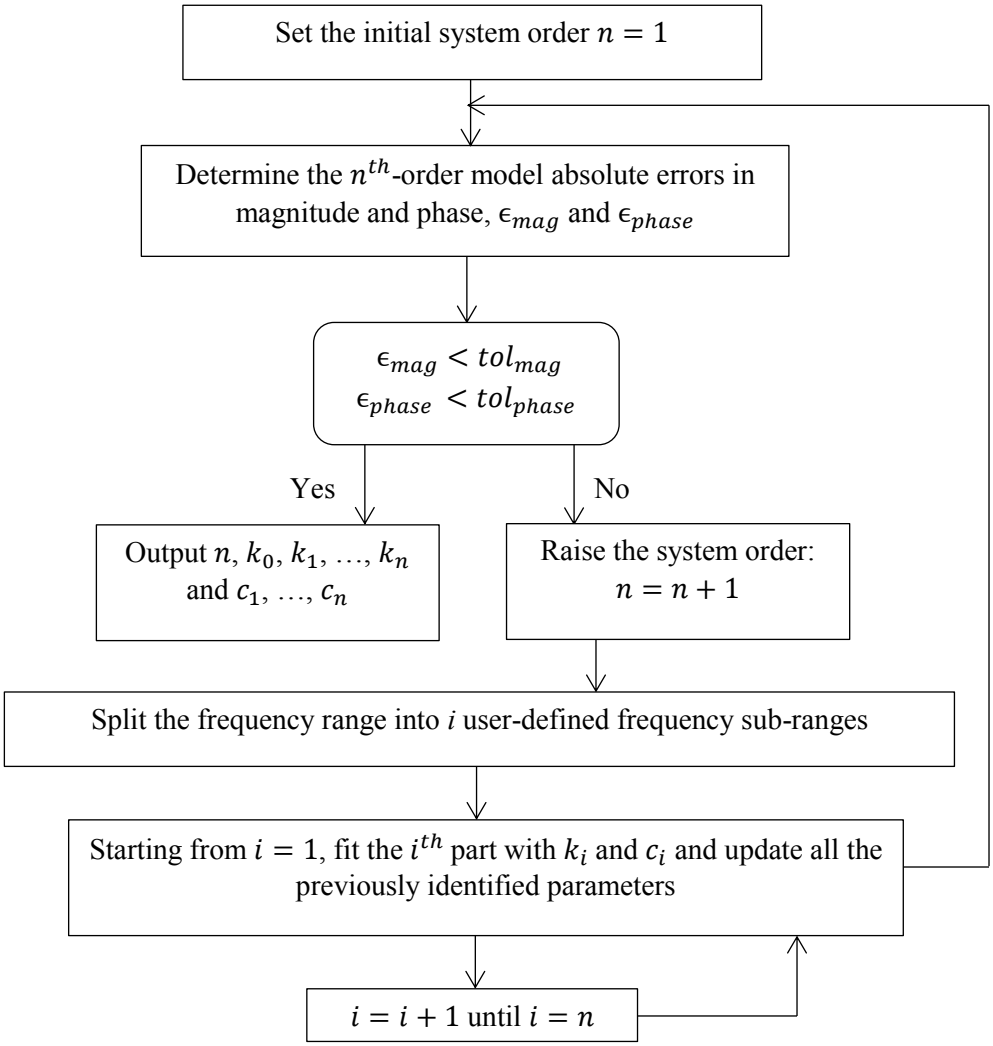

Figure 4-4: The iterative scheme higher order system parameter identification.

The parameter identification is to be performed for DE samples under direct mechanical loading.

4.3 Experimental procedures

4.3.1 DE fabrication and configuration

To demonstrate the validity of the model, two types of DE having distinct viscoelastic properties were selected to be subjected to force measurements, polyacrylate- and silicone-based.

The polyacrylate was VHB^{TM} 4910 in a basic 1 mm thick film format from 3M^{TM}. For mechanical loading experiments, the following samples were fabricated:

C1. A single-layer sample of area 50 mm$\times$50 mm for experiments having lower mechanical strains that would not induce buckling of the sample under cyclic loading (see figures 4-5(a) and 4-5(b)).

C2. A stacked sample of area 10 mm$\times$10 mm consisting of 10 layers giving a total thickness of 10 mm for experiments having higher mechanical strains without buckling under cyclic loading (which would otherwise cause buckling in the format of case C1) (see figure 4-5(c)).

For electrical actuation experiments, the single-layer sample included an AR of area 40 mm40 mm. Cables were wired onto the clamps and the AR was extended to the clamp for the lead contact. The electrode material used was graphite powder, which was chosen to facilitate the electrode deposition using the screen printing technique. Figure 4-5 shows the sample configurations.

The silicone was PlatSil 7315, a clear Room Temperature Vulcanization (RTV) silicone rubber. It has a Pour Time of 20 minutes at room temperature, which gave sufficient time to mix the agents, degas and pour into the mould for curing. The degassing was performed under 90 Pa for 10 minutes in a vacuum oven. This silicone elastomer was also selected because of its low mixing viscosity at 2,500 cP that eases degassing. The mould for curing the mixture into the film was made

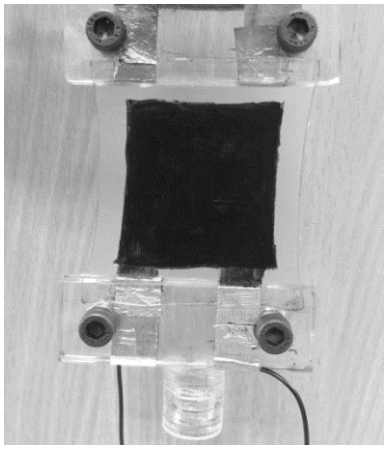

(a)

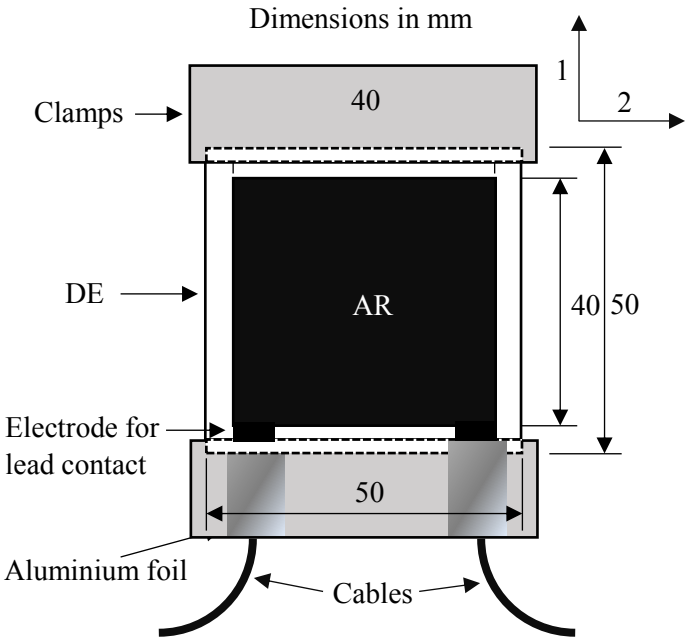

(b)

10-layer sample configured as:

50 mm × 10 mm × 10mm

(c)

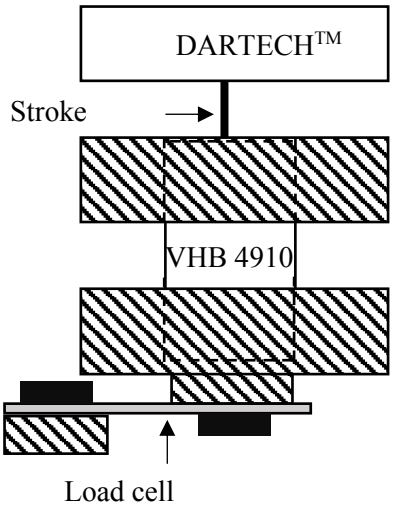

(d)

Figure 4-5: DE configurations (a) single-layer sample for DE force actuation and mechanical loading having low mechanical strains, polyacrylate and silicone (b) schematic view, (c) stacked sample for mechanical loading having high mechanical strains, polyacrylate only, and (d) schematic view. (AR refers to the active electrode region for DE actuation.)

from flat glass plate. Insulating tape of thickness 150 μm was used to form the inner walls of the glass. Four layers of tape were used, hence producing a 600 μm thick silicone film for the walls of the mould. Using the glass-based mould ensured that the film had a low surface roughness compared with a metallic mould that would have required precision machining. The drawback is that the tape is very flexible and may distort and have variable thickness when building up the walls. It may lead to slight errors in the thickness of the cured film. After the degassed mixture was poured into the mould, it took approximately 5 hours to cure.

4.3.2 Measurement system setup

For mechanical loading at low frequencies, the stacked multi-layer sample of polyacrylate was clamped to a hydraulic loading machine, HCIO from DARTECH^{TM} and to a load cell, LCBP-5 from OMEGA^{TM} . The load cell was capable of measuring forces up to 50 N. The stacked sample was clamped to give exposed length of 10 mm, then it was pre-strained by 100% to have the effective length of 20 mm. Cyclic loading was then applied under closed loop control to give peak-peak sinusoidal displacements as 2 mm (0 to 10% strain), 4 mm (0 to 20%), 6 mm (0 to 30%), 8 mm (0 to 40%), 10 mm (0 to 50%). At each level of cyclic strain, force measurements were recorded over 10 cycles at frequencies in the range of 0.01 Hz to 5 Hz. The setup is shown in figure 4-5(d).

For mechanical loading at higher frequencies, the single layer samples (polyacrylate and silicone) were pre-strained, $\lambda_{1,pre} = 1.2$ for silicone, and $\lambda_{1,pre} = 1.4$ for polyacrylate, to achieve better force resolution. The samples were clamped to an electromagnetic shaker (Model 455 from LDS^{TM}). The displacements of cyclic testing were measured by a laser vibrometer (PSV-400 from Polytec^{TM}). A load cell connected to the sample at the bottom of the rig was used to take force measurements. The cell was purpose-made of aluminium and designed to measure forces up to 2 N. A command chirp signal that had a frequency range from 1 Hz to 100 Hz was used to induce the cyclic loading of the DE samples. The setup is shown in figure 4-6(a). For electrical actuation, the single-layer DE samples were pre-strained in similar manner as for higher frequency mechanical loading and clamped to the test rig and the load cell as shown in figure 4-6(b). The height of

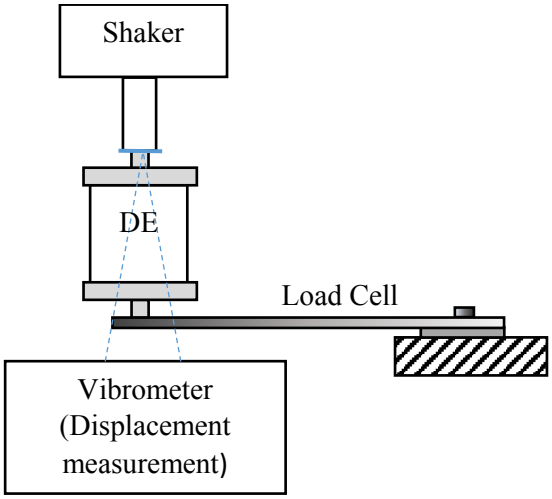

(a)

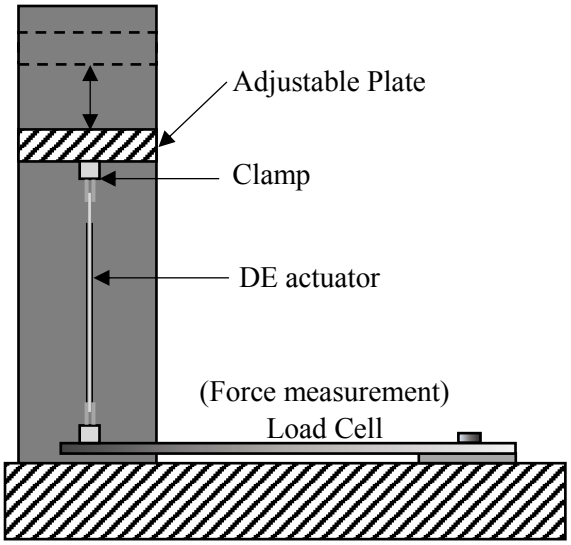

(b)

Figure 4-6: Test rig setups for the experiments: (a) mechanical loading at higher frequencies (b) electrical actuation.

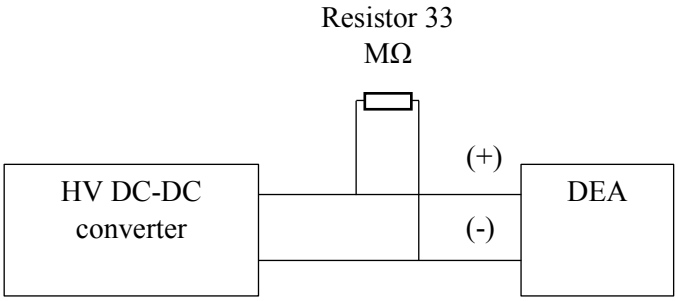

(a)

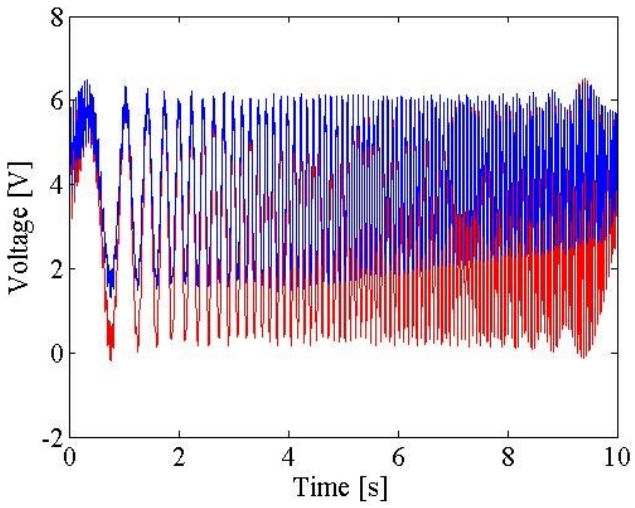

(b)

Figure 4-7: (a) Connecting a resistor in parallel to single-layer DE actuator sample to reduce the effect of current discharge. (b) Command signal (red) and actual voltage profile (blue) of a SPHS signal as the driving voltage for electrical actuation.

the top plate was adjustable for setting the samples with configured pre-strain. A high voltage (HV) generator, based on a HV DC-DC converter (module 15A24 from PPM^{TM}), was used to amplify the input voltage (0-10 V) to the voltage output (0-15 kV). A resistor of 33 MΩ was connected in parallel with the sample to reduce the lag from the HV generator due to the associated current discharge (figure 4-7(a)). The frequency responses of the samples were obtained using a Schroeder Phased Harmonic Sequence (SPHS) signal [190] as the input voltage that covered a frequency range from 1 Hz to 100 Hz as shown in figure 4-7(b).

4.3.3 Data correction to remove resonance effects

Depending on the mass of the clamp used to connect the DE samples to the load cell, and the stiffness of the load cell itself, resonance effects can occur. In our particular setting, resonance occurred between 40-60 Hz. Because the mass of the DE samples is negligible compared with that of the clamp, the resonance effects are not attributable to the characteristics of the DE samples. In order to obtain the true characteristics of the DE samples, a correction procedure was applied to remove the influence of the clamp-load cell resonance.

The dynamic stiffness characteristics of a DE sample under mechanical loading should be evaluated from

$$k = \frac{F_{DE}}{Z_{DE}} \tag{4.15}$$

where F_{DE} is the force exerted on the DE and Z_{DE} is the deformation of the DE sample. Due to resonance, the deflection of the load cell becomes significant when compared with the displacement input and DE deformation, hence the simplification of $\dot{x}_0' = x_0' = 0$ is no longer applicable. Given the force measured by the load cell, F, and the stiffness of the load cell, k_L, x_0' is given by

$$x_0' = \frac{F}{k_L} \tag{4.16}$$

If the displacement input due to mechanical loading is x_0, the deformation of the DE, Z_{DE}, is given by

$$Z_{DE} = x_0 - \frac{F}{k_L} \tag{4.17}$$

The force exerted on the DE is obtained by removing the inertia force:

$$F_{DE} = F - M\ddot{x}_0' \tag{4.18}$$

where M is the mass of the clamp. Combining equations (4.16-4.18), the dynamics of the DE under mechanical loading are represented by the corrected expression

$$\frac{F_{DE}}{Z_{DE}} = \frac{F - M\ddot{x}_0'}{x_0 - \dfrac{F}{k_L}} \tag{4.19}$$

The correction formula of equation (4.19) may be implemented in the frequency domain. Given

$$\begin{aligned} x_0'(t) &= X_0' \sin(\omega t + \phi) \\ \ddot{x}_0'(t) &= -\omega^2 X_0' \sin(\omega t + \phi) \end{aligned} \tag{4.20}$$

where ϕ is the same phase as in F (equation (4.10)), it follows in the complex form that

$$\frac{F_{DE}}{Z_{DE}} = \frac{(F_0 + M\omega^2 X_0')e^{i\phi}}{X_0 - \dfrac{F_0 e^{i\phi}}{k_L}} \tag{4.21}$$

Similarly, in the case of electrical actuation, $F_A = F_{A0} \sin \omega t$, the dynamics are represented by the complex form

$$\frac{F_{DE}}{F_A} = \frac{(F_0 + M\omega^2 X_0')e^{i\phi}}{F_{A0} - M\omega^2 X_0' e^{i\phi}} \tag{4.22}$$

The values of k_L and M should be adjusted to suit the experimental setup. Under mechanical loading up to 5 Hz, a relatively stiff load cell was used to measure the force output of the stacked DE samples compared to that used for the single-layer samples up to 100 Hz. The clamps used were different in each case, but had similar masses. Resonance was experienced around 50 Hz for the single-layer tests, which is within the test range, hence the correction formulas were applied. However, for the stacked sample tests, the resonant frequency greatly exceeded 5 Hz, hence the corrections were not applied.

4.4 Results

4.4.1 Mechanical loading over 0.01-5 Hz for the stacked polyacrylate sample

Figure 4-8 shows the mechanical loading results for the stacked polyacrylate sample under 100% pre-strain and peak-peak strain variations of 0 to (10%, 20%, 30%, 40%, 50%) over the frequencies up to 5 Hz. It is evident that the phase variations depend only weakly on the dynamic loading. However, the magnitudes vary between 2.3 N/mm and 3 N/mm at 5 Hz, higher strain variations giving reduced magnitudes.

Figure 4-9 shows the magnitude and phase variations averaged over the strain variations. These averaged curves were then used to fit first-, second- and third-order models following the flow chart in figure 4-4. Table 4.2 shows the identified parameters for models and the evaluated errors in magnitude and phase. It shows that by having a second-order model, the errors are reduced by approximately 40%; by having a third- order model, the errors are reduced by approximately 80%. Moreover, given the cross-sectional area of the sample as $A = 100$ mm^2, the pre-strain $\lambda_{1,pre} = 2$ and the effective length of the sample as $l = 20$ mm, the

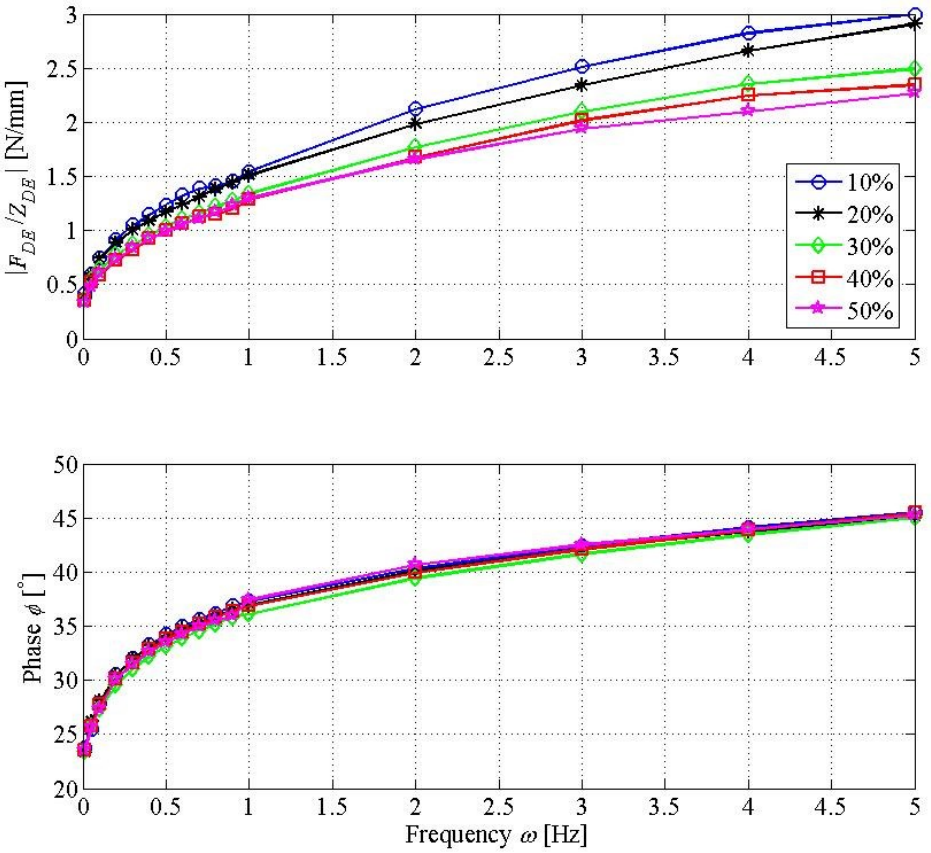

Figure 4-8: The measured characteristics of the stacked polyacrylate samples under 100% pre-strain and peak-peak strain variations 0 to (10%, 20%, 30%, 40%, 50%).

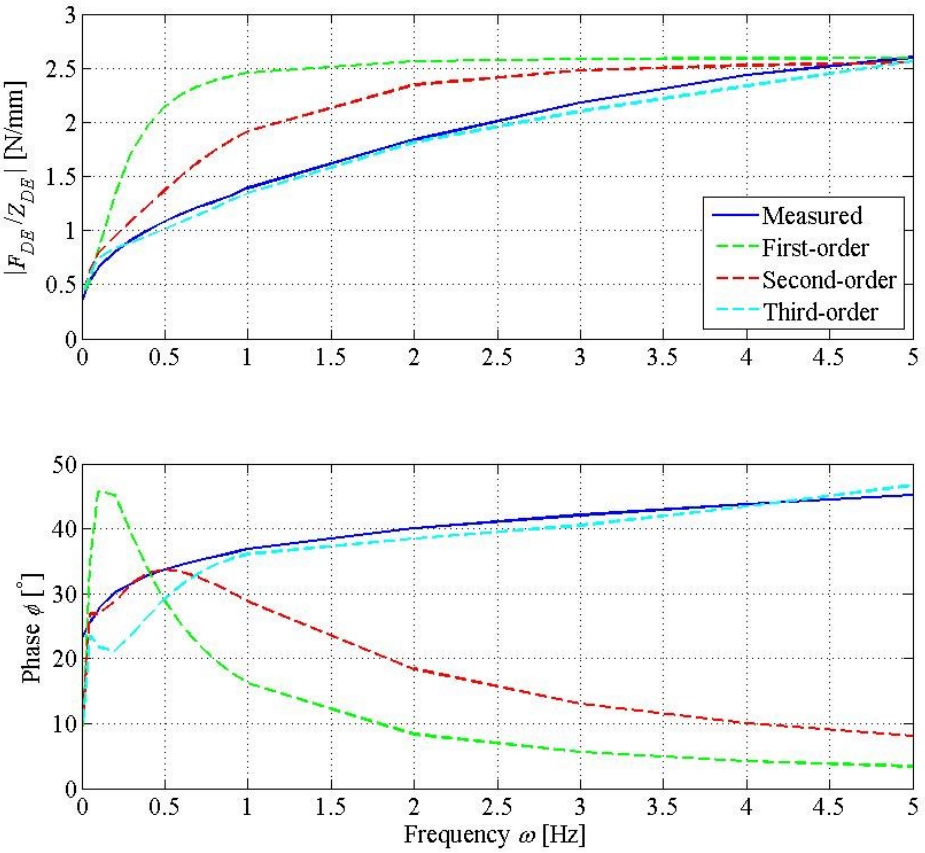

Figure 4-9: Comparing the averaged dynamics with first-, second- and third-order models. The identified parameters are listed in table 4.2.

Table 4.2: The stiffness and damping coefficients of springs and dampers in DE models for the stacked polyacrylate sample under mechanical loading up to 5 Hz.

Order	k_i [N/mm]				c_i [N$\cdots$s/mm]			ϵ_{mag}	ϵ_{phase}
	0	1	2	3	1	2	3	[N/mm]	[$^\circ$]
1	0.40	2.20	-	-	1.00	-	-	0.64	18.58
2	0.40	0.40	1.80	-	1.00	0.28	-	0.26	10.05
3	0.40	0.40	1.00	50	1.00	0.1	0.05	0.06	3.96

identified k_0 indicates the estimated elastic modulus of the polyacrylate as 0.16 MPa, which is close to the expected value.

4.4.2 Mechanical loading over 1-100 Hz for single-layer silicone and polyacrylate samples

Figures 4-10 and 4-11 present the original and corrected results for the single-layer silicone and polyacrylate samples under mechanical loading up to 100 Hz. The pre-strains were $\lambda_{1,pre} = 1.2$ for silicone, and $\lambda_{1,pre} = 1.4$ for polyacrylate, and the loading strains were less than 10% in peak-peak variation. The original results show the resonances are approximately at 50 Hz, with higher damping evidence in polyacrylate. In the corrected results, the silicone has a near constant stiffness and zero phase, while the polyacrylate has increasing stiffness and positive phase throughout the frequency range.

Figure 4-12 shows the corrected measured characteristics with the fitted first-order model for the silicone sample with the identified parameters listed in table 4.3. It shows that the first-order model fit is sufficient to predict the dynamics of the spring-like silicone. The model is accurate up to 70 Hz, however, measurement noise above 70 Hz is significant, which gives rise to the larger than expected (apparent) errors listed in table 4.4. Figure 4-13 compares the corrected measured characteristics with models for first-, second- and third-order for the single-layer polyacrylate and the identified parameters are listed in table 4.3. It shows the third-order model is clearly superior to the first-order model. As indicated in table 4.4, the errors of the third-order model are only 8% of those of the first-order model.

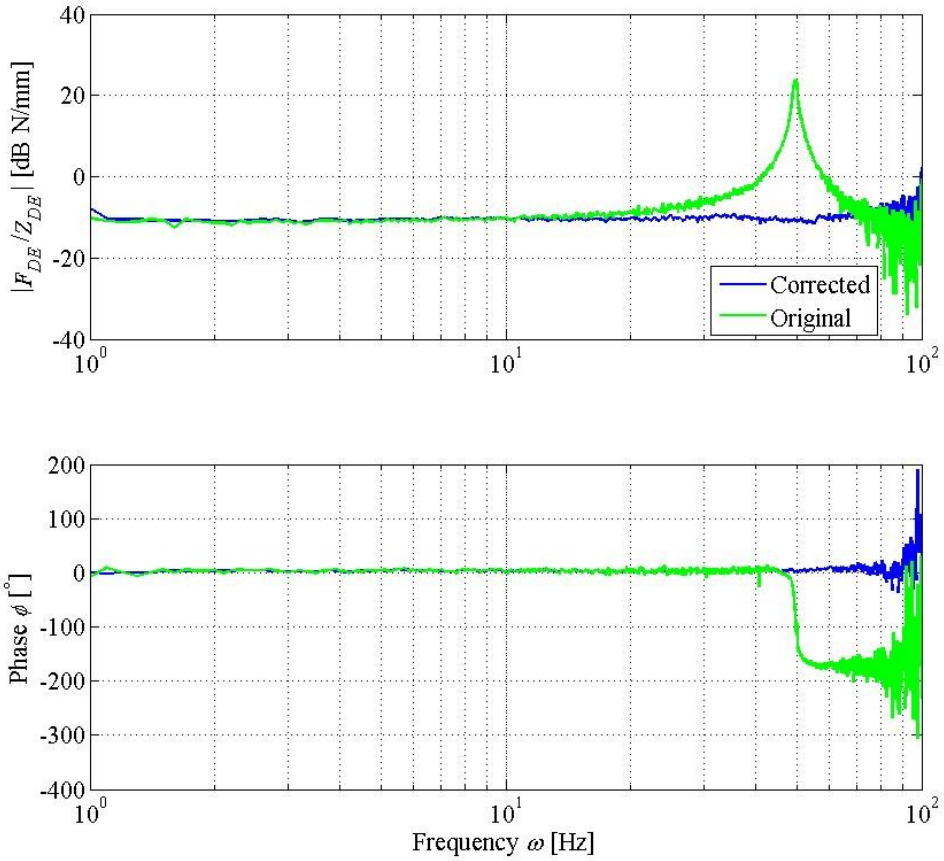

Figure 4-10: The original and corrected (taking the resonance of the load cell into account) characteristics of the single-layer silicone sample under mechanical loading up to 100 Hz.

Table 4.3: The stiffness and damping coefficients of springs and dampers in DE models for the single-layer silicone and polyacrylate samples under mechanical loading up to 100 Hz.

Order		k_i [N/mm]				c_i [N·s/mm]		
		0	1	2	3	1	2	3
Silicone	1	0.29	0.3	-	-	1.4×10^{-4}	-	-
	1	1.00	4.00	-	-	0.1	-	-
Polyacrylate	2	1.00	4.00	4.00	-	0.1	0.02	-
	3	1.00	1.50	2.00	30.00	0.05	0.02	0.02

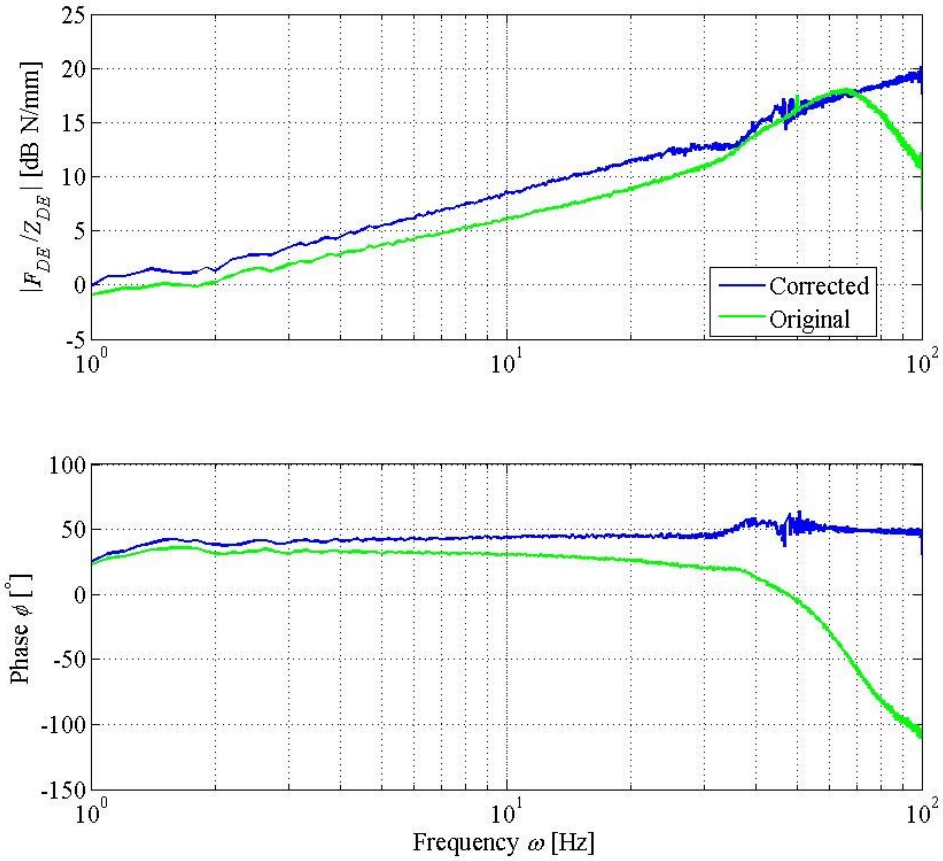

Figure 4-11: The original and corrected measured characteristics of the single-layer polyacrylate sample under mechanical loading up to 100 Hz.

Table 4.4: Errors for the single-layer silicone and polyacrylate models under mechanical loading up to 100 Hz.

	Order	ϵ_{mag} [N/mm]	ϵ_{phase} [°]
Silicone	1	1.11	8.66
Polyacrylate	1	1.73	37.52
	2	1.29	28.58
	3	1.05	2.64

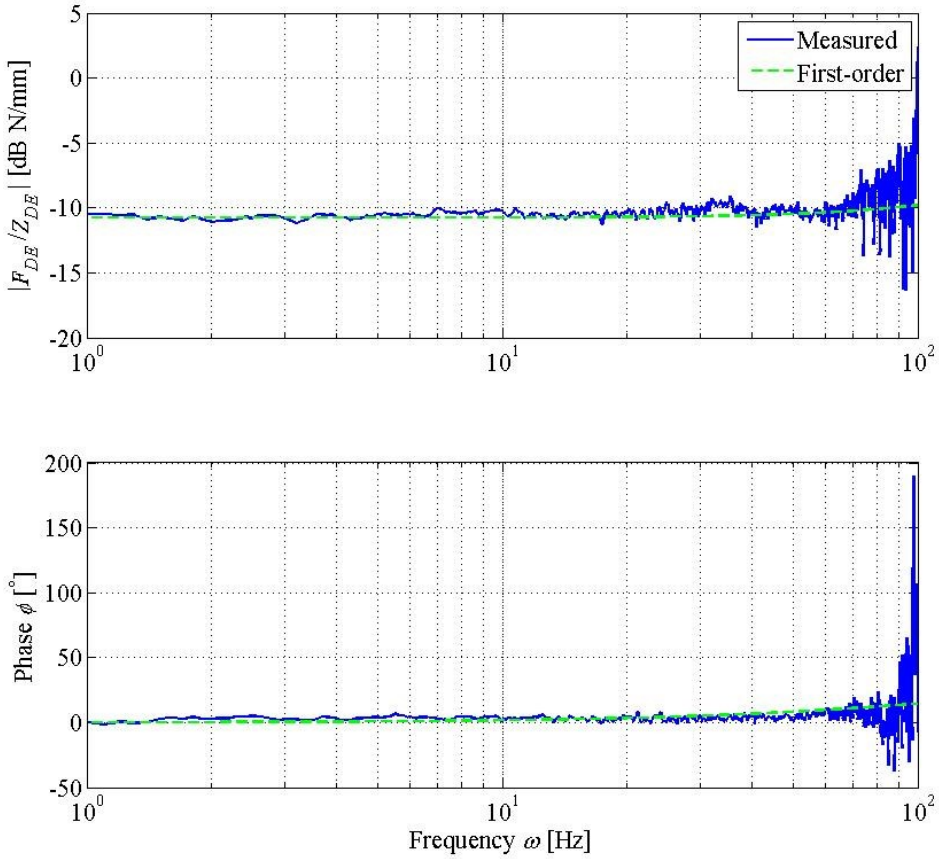

Figure 4-12: The corrected measured characteristics of the single-layer silicone sample compared with the first-order model under mechanical loading, the identified parameters are listed in table 4.3.

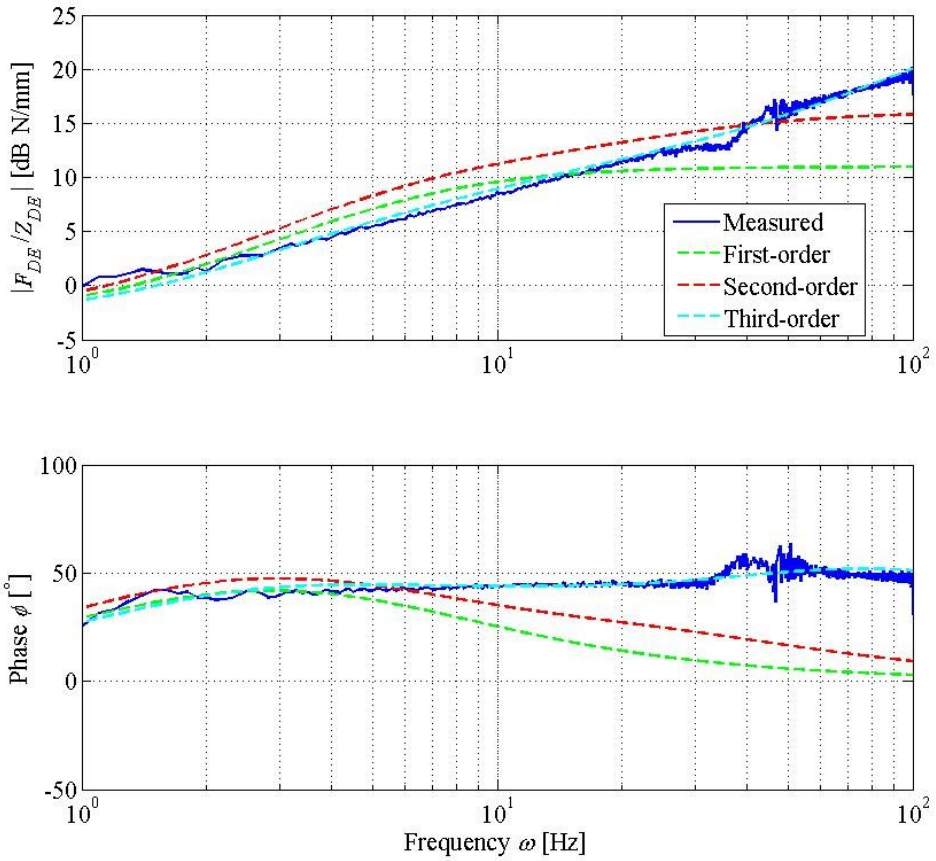

Figure 4-13: The corrected measured characteristics of the single-layer polyacrylate sample compared with the first-, second- and third-order models under mechanical loading, the identified parameters are listed in table 4.3.

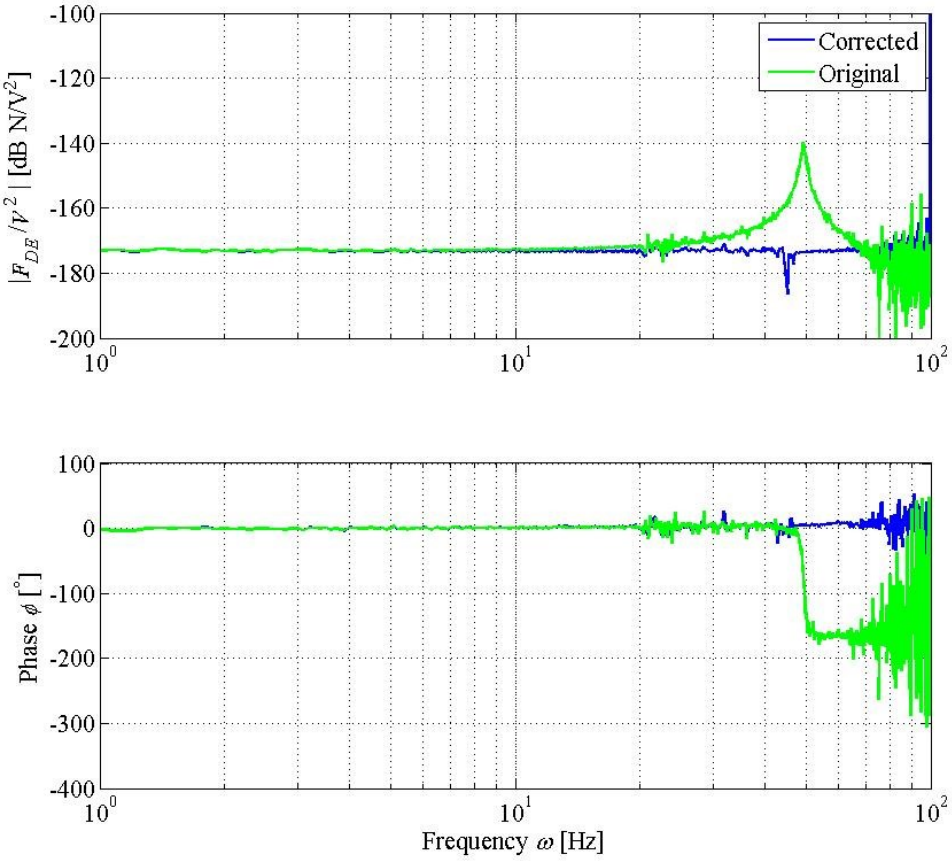

Figure 4-14: The original and corrected measured characteristics of the single-layer silicone sample under electrical actuation up to 100 Hz.

4.4.3 Electrical actuation over 1-100 Hz for single-layer silicone and polyacrylate samples

Figures 4-14 and 4-15 present the original and corrected measured characteristics for the single-layer silicone and the polyacrylate samples under electrical actuation up to 100 Hz. The pre-strains were $\lambda_{1,pre} = 1.2$ for silicone, and $\lambda_{1,pre} = 1.4$ for polyacrylate, and the driving voltage was up to 7 kV. According to equation (4.8), the driving force F_A is proportional to V^2, hence the results are presented in terms of F_{DE}/V^2. The original measured characteristics show resonance between 50-55 Hz. In the corrected measured characteristics, the silicone has a near constant dynamics and zero phase while the polyacrylate has decreasing magnitude

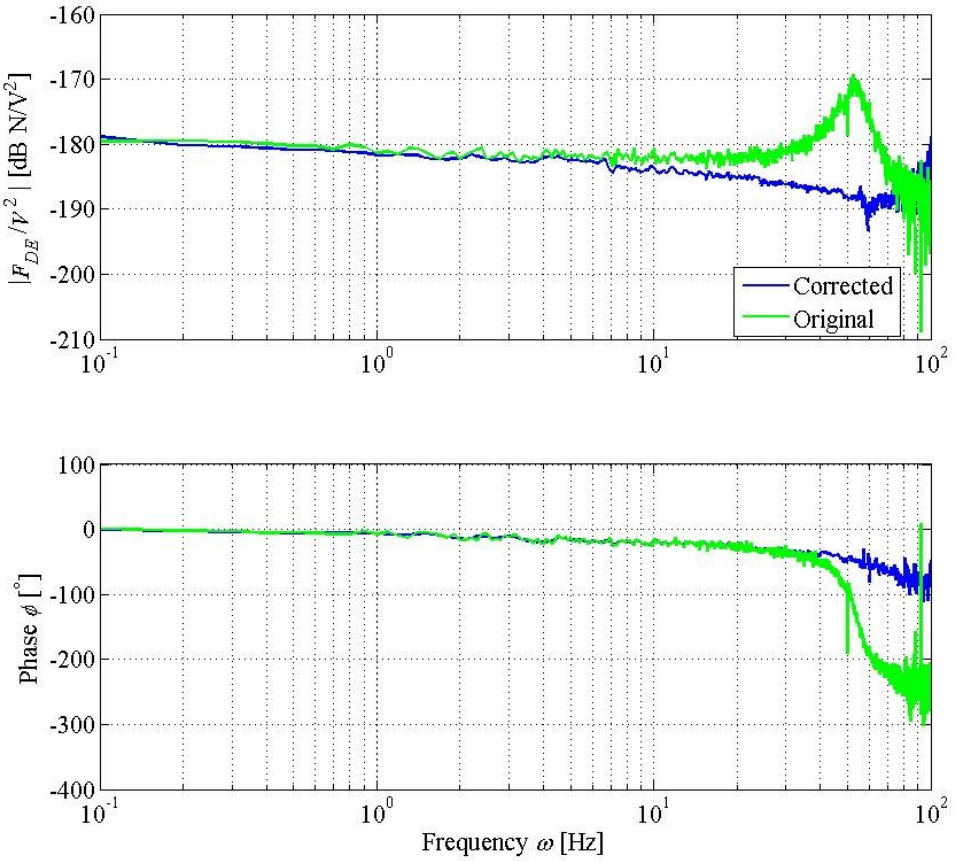

Figure 4-15: The original and corrected measured characteristics of the single-layer polyacrylate sample under electrical actuation up to 100 Hz.

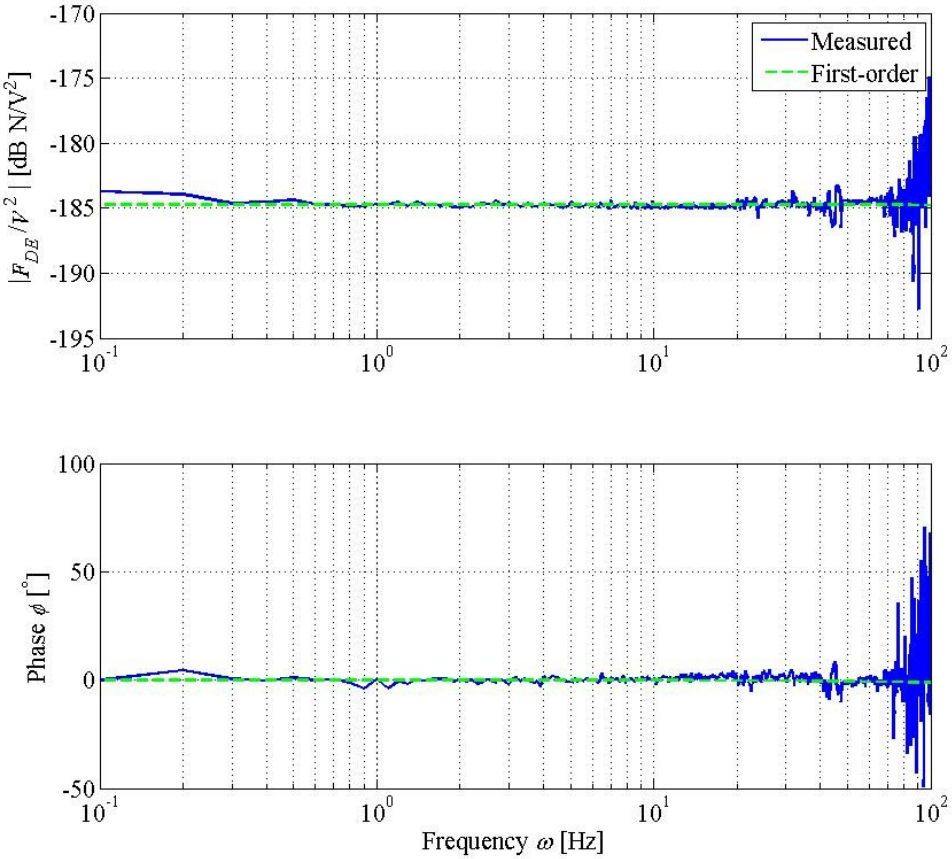

Figure 4-16: The corrected measured characteristics of the single-layer silicone sample compared with first-order model under electrical actuation, the identified parameters are listed in table 4.3.

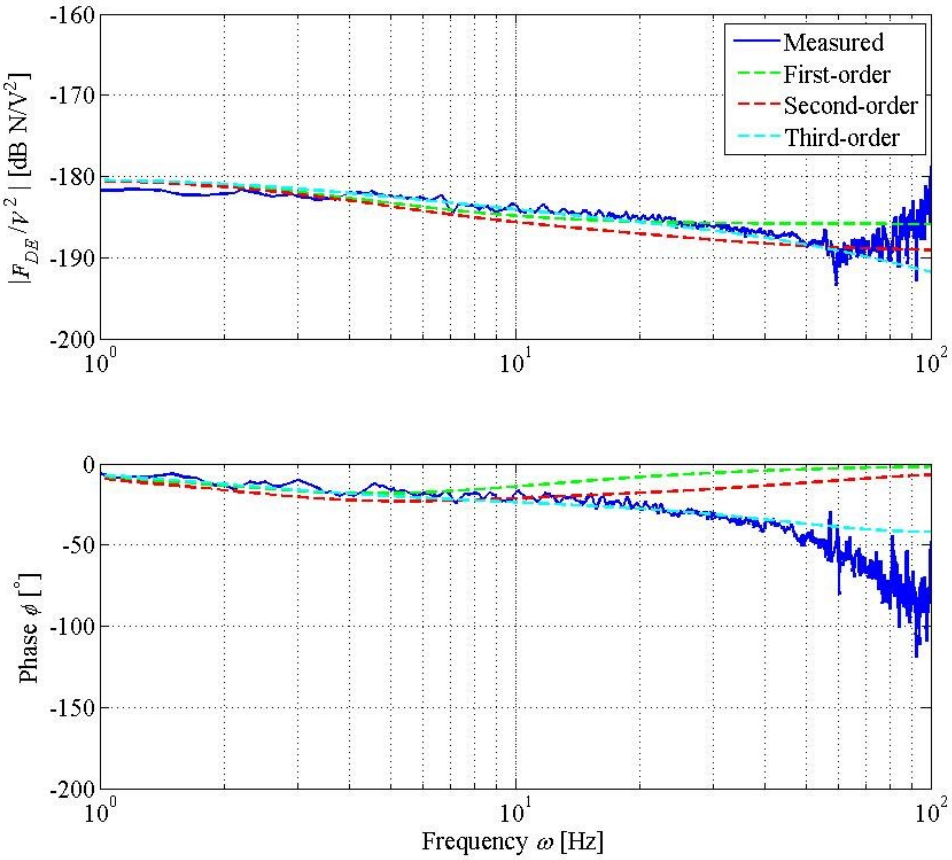

Figure 4-17: The corrected measured characteristics of the single-layer polyacrylate sample compared with the first-, second- and third-order models under electrical actuation, the identified parameters are listed in table 4.3.

and negative phase throughout the frequency range. A higher driving voltage is required for the polyacrylate to generate the same actuation force.

Figures 4-16 and 4-17 compare the corrected measured characteristics with the fitted models, parameters identified from mechanical loading tests (table 4.3). It shows that the first-order model fits well with the dynamics of the spring-like silicone. It also shows that the third-order model fits well for the dynamics of the polyacrylate, compared with the first-order model. The simulated dynamics deviate from the measured characteristics above 70 Hz because the actuation force is reduced and affected by measurement noise (e.g. low signal to noise ratio).

4.5 Conclusions

This chapter concludes that accurate modelling of the dynamic characteristics of DEs and DE actuators is achievable in the frequency domain. The use of higher order Maxwell-Wiechert material models that contain multiple spring-damper combinations has been considered for more accurate representation of the viscoelastic characteristics of the dielectric polymers. Compared with a conventional first-order model, the higher order representation allows the system dynamics to be shaped over frequency ranges. They offer more degrees of freedom in the parameter identification process, which leads to more accurate determination of the frequency response. An iterative procedure has been devised to guide the parameter identification such that magnitude and phase error bounds are within specified tolerances.

To demonstrate the model identification, two dielectric polymers, silicone and polyacrylate, were used. They were configured in a single-layer sheet format for higher frequency testing during which the mechanical strain variations were less than 10%, thus avoiding buckling of the sheet during the cyclic loading. Lower frequency testing with strain variations above 10% were performed using stacked layers of the polyacrylate, to eliminate the occurrence of buckling during the cyclic loading. The polymer samples were subjected cyclic loading and forces were measured using load cells. The combination of low level forces and the low stiffness

of the load cell used during the higher frequency testing led to resonance being experienced within the frequency range. A correction procedure was therefore implemented in which the inertia forces and load cell deflections were accounted for and eliminated from the dynamic frequency response measurements to reveal the characteristics of the polymer samples alone.

The experimental results and parameter identification for the silicone sample under mechanical loading indicated that a first-order model is appropriate, which is due to the spring-like behaviour of the polymer material. However, the polyacrylate samples required third-order models to achieve suitable accuracy to represent the viscoelastic characteristics. For the polyacrylate, third-order models improved the accuracy in modelling by 80% compared with the conventional first-order model.

The proposed higher order modelling and parameter identification of this chapter should prove useful in the model-based control for polymer-based soft robotic systems.

Chapter 5

A novel dielectric elastomer self-sensed actuator (DESA)

This chapter addresses the research gap in self-sensing DEAs as identified from Section 2.3. It presents a novel self-sensing mechanism that uses capacitive sensing to detect the actuation of force in a dielectric elastomer sensing actuator (DESA) is proposed. In contrast to a conventional self-sensing DEA, it consists of an electro-active region (AR) for the actuation together with an independent electro-sensing region (SR). By doing so, the self-sensing mechanism does not exhibit long-term drift in the correlation between the structural deformation and the capacitive change, which is commonly found in conventional self-sensing DEAs. The results show that the proportional-integral (PI) controlled DESA performs effectively under uniaxial actuation. The DESA can suppress the relaxation of the viscoelastic DE and thus enable a constant force output. It also shows that the sensing capacity of the DESA can be enhanced further with appropriate electrode arrangement and motion constraining. Furthermore, the results show that the DESA senses the off-plane expansion distinctly compared with the in-plane deformation, which helps to detect any wrinkling of the structure.

5.1 Conventional self-sensed DEA

As a next generation soft actuation technology, dielectric elastomer actuation is of particular interest because of its similar capability to human muscle [34, 167, 168, 97, 170, 111, 121]. It consists of a dielectric elastomer (DE) film that is sandwiched between compliant electrodes. When a high voltage is applied across the electrodes, the structure responds in planar expansion with contraction in thickness. The outstanding material properties in the electro-mechanical coupling make the DE ideal for displacement/strain sensing [75, 76], energy harvesting [141, 120, 121], as well as actuation [179, 180, 181, 191]. A dielectric elastomer actuator (DEA) has demonstrable muscle-like capability in bio-inspired robots [192, 193, 194, 40], tuneable optics [43, 44, 46, 47], flexible robotic legs [136], and lighter-than-air vehicles [195]. However, the advancement in other applications is hindered by the viscoelasticity of the DE. For a typical elastomer such as VHB^{TM} 4910 from 3M, the time-dependent stress-strain relationship causes long-term relaxation upon loading and sluggish responses, which limit high-frequency actuation. The force and displacement control of the DEA require feedback to achieve the required performance.

Closed loop operation has been applied to adjust actuation force and strain [142, 143, 144, 145]. These works show that with external sensors, motion control can be achieved with proportional-integral-derivative (PID) controllers. The DEA-based tuneable grating is a typical example [46]. A compliant grating is placed on the DEA so that it deforms with the DE as the voltage is applied. It uses the first-order diffraction angle of the grating that is measured by a photo-diode to drive the DEA to the desired deformation. However, the main drawbacks are the complexity and high cost of the system. Furthermore, it contradicts the intention in utilizing a low-cost polymeric actuation approach.

Another alternative is to use a DEA as a motion sensor, to form a self-sensing DEA. Past work has focused on use a single electro-active region (AR) to perform both the actuation and the sensing. Resistive sensing is commonly avoided as the conductivity of the electrode depends on many factors, including the electrode material, the electrode configuration and the deformation of the DE [166]. Capacitive sensing is better because the capacitance depends only on the geom-

etry of the capacitor and the electrode coverage [160, 159]. The capacitance is measured typically by using a high frequency AC signal that is superimposed on the actuation voltage [76, 152, 155, 196, 197]. Other approaches use pulse width modulation to measure the capacitive discharge rate [148], and step voltage application to measure charge [153]. However, these publications show also that large deformations of the DE and coupled high electric fields during the operation cause complex changes in the electrode resistance and dielectric resistance, which leads to the unexpected capacitive response in the actuation [163, 164, 165, 128].

This chapter presents the concept of a dielectric elastomer sensing actuator (DESA), a self-sensing DE actuator that utilizes separate electrode regions for sensing and actuating. By doing so, it demonstrates that the capacitive sensing mechanism in the DESA performs effectively and does not suffer from the previously mentioned deficiencies. Moreover, the performance of the structure with alternative electrode arrangements and motion constraining are also assessed. Finally, the challenges in implementing the DESA structure, the effects of electrode coverage and off-plane actuation on sensing resolution of the DESA are studied.

5.2 Theory

5.2.1 Capacitive sensing in the DESA

In the structure of a DESA, the high voltage application across the AR deforms the entire elastomer. The electro-sensing region (SR) detects such deformation, and its capacitance changes correspondingly. For an understanding of the self-sensing mechanism, the correlation of $\lambda_{AR} = f(C)$ is derived, where C is the capacitance in the SR and λ_{AR} is the voltage induced mechanical deformation in the AR. Figure 1 shows the geometric correlation of the DESA with and without the voltage application. The DESA is pre-strained and constrained in direction 1, serving as a linear actuator. It is assumed that the SR only detects the deformation of the AR in direction 1 (e.g. the sensing is independent of the lateral expansion of the AR and the resulting inhomogeneous thickness due to the actuation). This assumption was validated from the experimental results

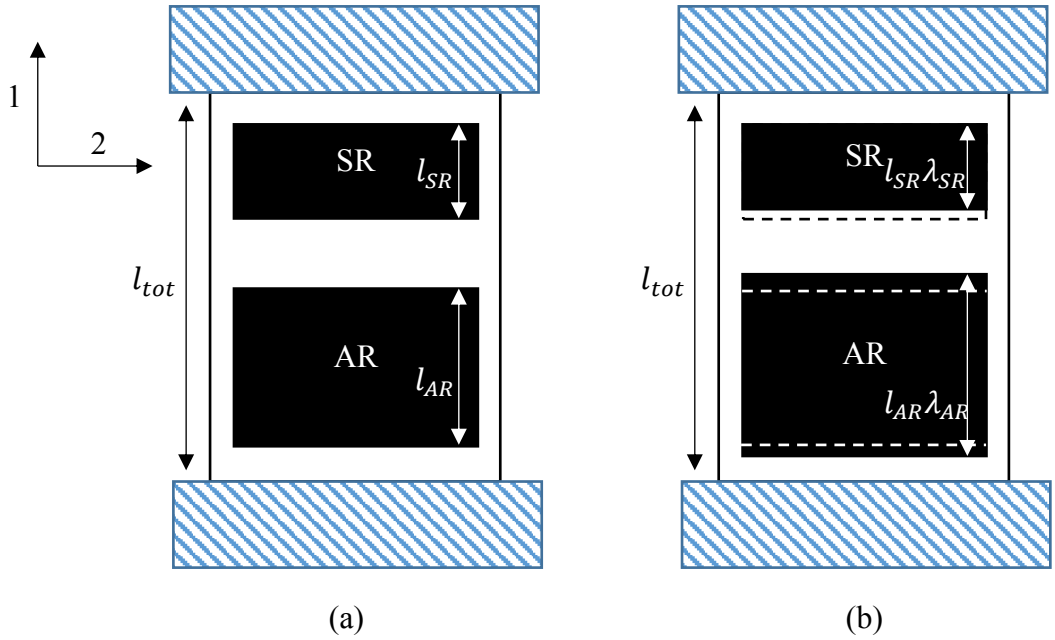

Figure 5-1: Geometric correlation of the DESA: (a) the undeformed state and (b) the actuated state.

(section 5.4.1, figure 5-5b) when a 15 mm gap was set between the electrode regions. Moreover, the overall length of the film in direction 1 is assumed to be constant as in the experiment the DESA was fixed on the top and clamped to a load cell on the bottom that was much stiffer than the DESA. When the voltage is applied, assuming the AR expands uniformly in the strain of λ_{AR} (Figure 1b), the corresponding strain in the SR, λ_{SR} is given by

$$\lambda_{SR} = \frac{l_{tot} - l_{AR}\lambda_{AR}}{l_{tot} - l_{AR}} \tag{5.1}$$

where l_{tot} is the total length of the film, l_{AR} is the length of the AR and λ_{AR} is the voltage-induced strain in l_{AR}. Taking the incompressibility of the elastomer, the volume associated with the SR implies that

$$\lambda_{SR}\lambda_h\lambda_w = 1 \tag{5.2}$$

where λ_w and λ_h are the resulting strains of the SR in direction 2 and the direction of thickness, respectively. Assuming that the elastomer is isochoric, the uniaxial loading condition gives

$$\lambda_w = \lambda_h = \frac{1}{\sqrt{\lambda_{SR}}} \tag{5.3}$$

The capacitance of the SR in the undeformed state is therefore given by

$$C_0 = \frac{\varepsilon_0 \varepsilon_r w l_{SR}}{h} \tag{5.4}$$

where ε_0 is the permittivity of free space, ε_r is the relative permittivity of the elastomer and w, h are the width and the thickness of the SR, respectively. Substituting equation (5.3) into (5.4) gives the resultant capacitance in the actuated state C_a as

$$C_a = C_0 \lambda_{SR} \tag{5.5}$$

Substituting equation (5.1) into (5.5) gives the strain in capacitance λ_{cap} that can be defined as

$$\lambda_{cap} = \frac{C_a}{C_0} = \frac{l_{tot} - l_{AR}\lambda_{AR}}{l_{tot} - l_{AR}} \tag{5.6}$$

Equation (5.6) shows that by applying voltage across the AR, the increase in the mechanical strain λ_{AR} causes a decrease in the capacitive strain λ_{cap} (i.e. decrease in measured capacitance). This equation also shows the linear relationship between the capacitive strain in the SR and mechanical strain in the AR, which is ideal for implementing linear controllers.

In order to understand fully the proposed sensing mechanism, one extreme case to consider would be that with the SR placed adjacent to the AR, in which the deformation of the SR is also affected by the lateral expansion of the AR. It is

assumed that in direction 1 the sensing strain remains as in equation (5.1), while in direction 2 the SR is stretched by the AR as

$$\lambda_{SR-L} = \lambda_{AR-L} \tag{5.7}$$

where λ_{AR-L} is the actuation strain of the AR in direction 2. As a result, recalling the incompressibility of the elastomer, the resulting strain in thickness becomes

$$\lambda_h = \frac{1}{\lambda_1 \lambda_2} = \frac{1}{\lambda_{SR} \lambda_{SR-L}} \tag{5.8}$$

Substituting equation (5.8) into (5.4), (5.5) and (5.6) yields

$$\lambda_{cap} = \frac{C_a}{C_0} = (\lambda_{SR} \lambda_{AR-L})^2 \tag{5.9}$$

Substituting equation (5.1) into (5.9) gives the new correlation between the capacitive strain λ_{cap} and the actuation strains λ_{AR} and λ_{AR-L} as

$$\lambda_{cap} = \frac{{l_{tot}}^2 {\lambda_{AR-L}}^2 - 2 l_{tot} l_{AR} \lambda_{AR} {\lambda_{AR-L}}^2 + {l_{AR}}^2 {\lambda_{AR}}^2 {\lambda_{AR-L}}^2}{{l_{tot}}^2 - 2 l_{tot} l_{AR} + {l_{AR}}^2} \tag{5.10}$$

When the uniaxial pre-strain is relatively low (< 1.5), it is expected that $\lambda_{AR} \approx \lambda_{AR-L}$, which yields

$$\lambda_{cap} = \frac{{l_{tot}}^2 {\lambda_{AR}}^2 - 2 l_{tot} l_{AR} {\lambda_{AR}}^3 + {l_{AR}}^2 {\lambda_{AR}}^4}{{l_{tot}}^2 - 2 l_{tot} l_{AR} + {l_{AR}}^2} \tag{5.11}$$

Figure 5-2 shows that when the SR is adjacent to the AR, the deformation-capacitance correlation becomes a 4-th order polynomial as in equation (5.11) and has a smaller overall capacitive variation. As the SR is located further away from the AR and is less affected by its lateral expansion, the curve shifts downwards and becomes linear as in equation (5.6). The inhomogeneous thickness

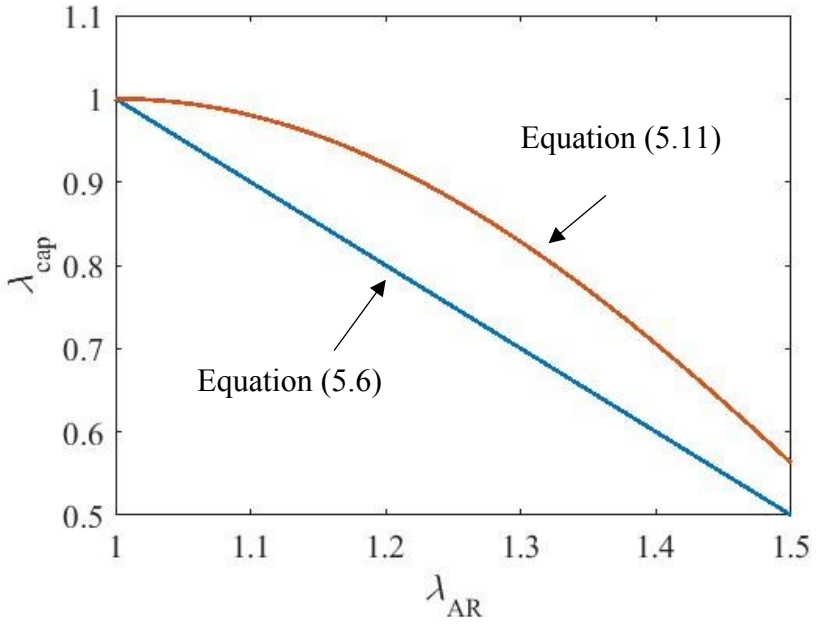

Figure 5-2: Comparison between the sensing mechanisms from equations (5.6) and (5.11).

is another factor that affects the sensing. Under actuation, the deformation of the AR increases locally the thickness of the surrounding region, which would further lower the capacitive change as in equation (5.11). Because the lateral expansion and the inhomogeneous thickness degrades the sensing performance of the SR, it is beneficial to locate the SR away from the AR.

For comparison, in a conventional self-sensing DEA the capacitive sensing and actuation share the same AR and the correlation between them is given as

$$C_a = C_0 \frac{\lambda_A}{\frac{1}{\lambda_A}} = C_0 {\lambda_A}^2 \tag{5.12}$$

where λ_A is the ratio of the area of the actuated AR to that of the pre-strained AR. In the case of a linear actuator with full constraint in the lateral direction, because the AR deforms only in one direction, the correlation between the actuation

stretch λ_{AR} and the capacitive change is derived to be quadratic as ([158])

$$C_a \propto {\lambda_{AR}}^2$$

In another case of a circular actuator, the correlation between the actuation strain in radial direction λ_r and the capacitive change holds as ([76])

$$C_a \propto {\lambda_r}^4$$

Such high-order correlations amplify noise in the associated capacitive measurement signals and limit the use of standard linear PID control action. More sophisticated control algorithms are therefore required to achieve optimal performance. Furthermore, because the SR in the DESA senses only the deformation in the single direction, the planar expansion of the AR is decoupled and can be measured separately for each direction. Such a sensing mechanism is more informative and beneficial in controlling more complex DEA-based systems. In the case when wrinkling of the elastomer occurs, the deformation of the AR is out-of-plane and it does not cause the consequential deformation of the rest of the structure. Then equation (5.6) is no longer applicable, and the SR does not sense the out-of-plane actuation, which also differs from the conventional self-sensing mechanism.

5.2.2 Force actuation in correlation to capacitive sensing

For the DESA as a force actuator, the equation of state in direction 1 is given by

$$\sigma_1 + \varepsilon E^2 = \frac{\lambda_1 \partial W(\lambda_1, \lambda_2)}{\partial \lambda_1} \tag{5.13}$$

where σ_1 is the stress due to the mechanical loading, εE^2 is the stress due to the electrical loading and $W(\lambda_1, \lambda_2)$ is the elastic free energy density function of the elastomer in terms of the in-plane strains λ_1 and λ_2. When the DE is pre-loaded only, σ_1 can be solved as the resultant mechanical stress by setting $E = 0$, The

stress differences between the actuated and pre-loaded states contributes to the force output of the DESA as

$$\Delta\sigma_1 = -\varepsilon E^2 \tag{5.14}$$

With the assumption of small voltage-induced deformation across the elastomer with strains up to 20%, the elastic modulus, Y_1, in direction 1 is assumed to remain constant throughout the operation. The net stress $\Delta\sigma_1$ can be correlated to λ_{AR} as

$$\Delta\sigma_1 = Y_1(\lambda_{AR} - 1) \tag{5.15}$$

Substituting equation (5.6) into (5.15) and taking the cross-sectional area of the elastomer into account, the force output of the DESA, Δ, can be expressed as

$$\Delta F = whY_1(\frac{l_{tot}}{l_{AR}} - 1)(1 - \lambda_{cap}) \tag{5.16}$$

Equation (5.16) shows that the force output is proportional to the capacitive strain. The linear correlation is also beneficial for the implementation of linear controllers.

5.3 Experimental Setup

The structure of the DESA is configured as shown in figure 5-3. The DE used in this work is the polyacrylate VHB^{TM} 4910 from 3M. The 1 mm thick tape was laser cut into the square of 50 mm $\times$ 50 mm (figure 5-3). After that the DE was pre-strained by $\lambda_{1,pre} = 50\%$, and the electrode was applied according to figures 5-3a and 5-3c. For the electrode regions, the SR was 15 mm $\times$ 30 mm and the AR was 20 mm $\times$30 mm. The applied electrode material was carbon black grease from MG, which was brushed onto the DE. The AR and the SR were aligned in direction 1 and the gap in between them was set to be 15 mm

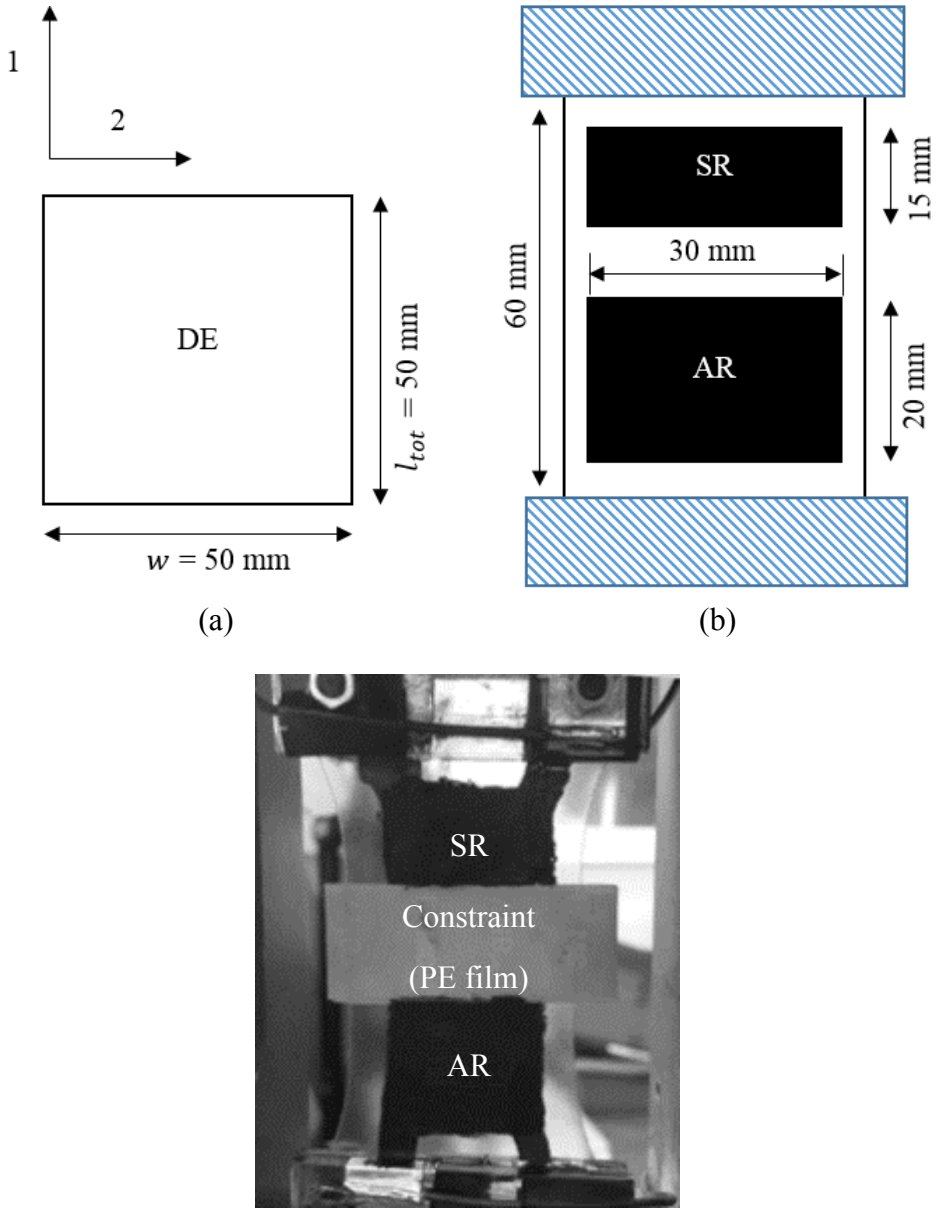

Figure 5-3: The configurations of the DESA: (a) the original DE film, (b) the pre-strained DE with electrode coating and (c) the actual DESA that is further enhanced with the motion-constrained layer.

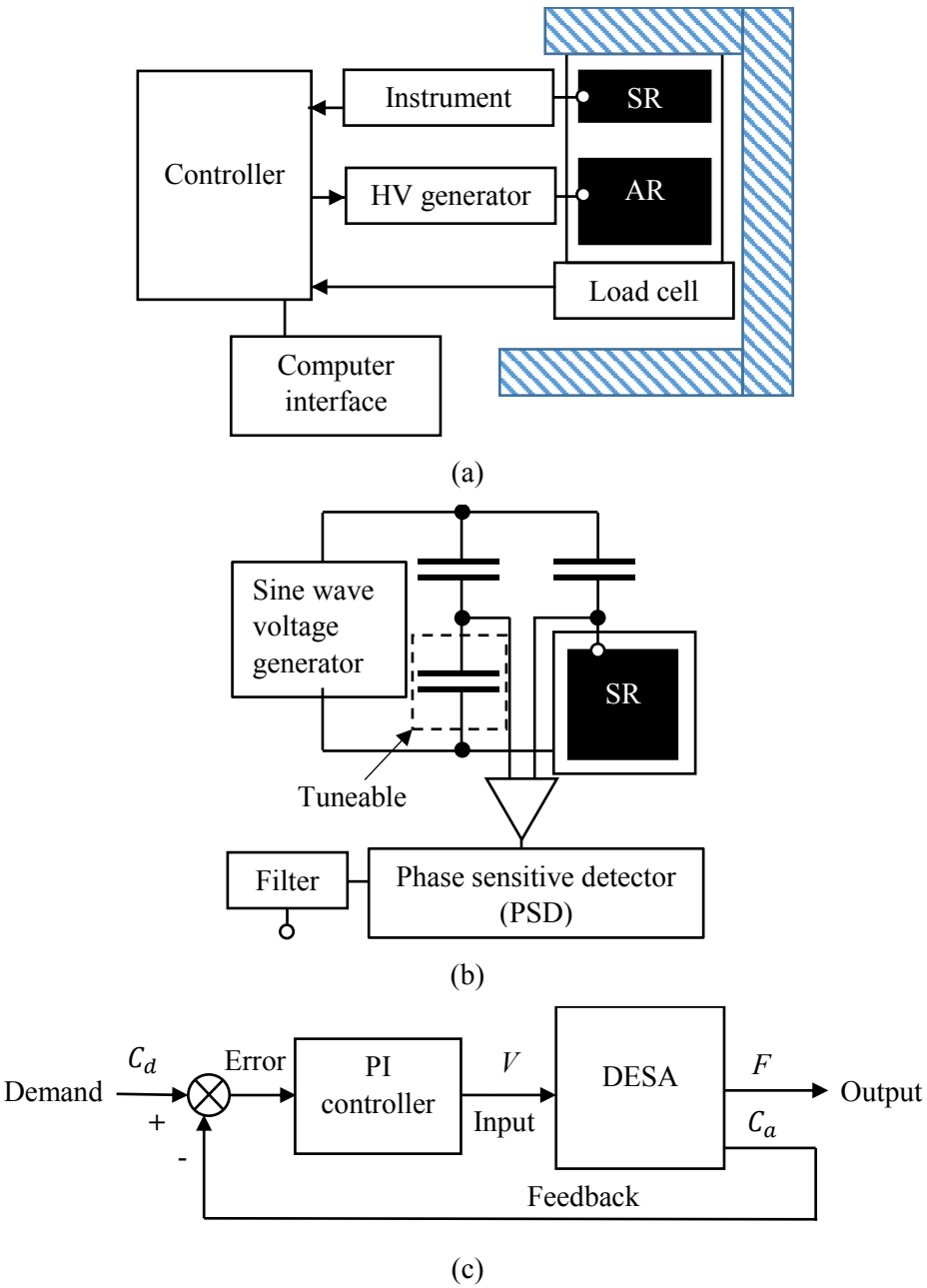

Figure 5-4: Schematic diagrams of (a) the experimental setup, (b) the capacitor-bridge-based instrument for capacitive measurement and (c) block diagram for closed loop operation.

to reduce any signal noise transmission due to the high electric field during the capacitive measurement. A layer of the PE film was also applied onto this gap to improve further the sensing and actuation conditions of the DESA.

The test rig setup is shown in figure 5-4a. The pre-strained DE was held by two clamps (figure 5-3c) that were made from acrylic material. Aluminium tape was wrapped around each clamp to provide the electrode contact. The top clamp connects the SR to the instrument for the capacitive sensing; the bottom clamp connects the AR to the HV generator for the actuation. On the bottom, the DE was mounted to a load cell for the force measurement up to 2 N. A HV generator was able to apply voltages up to 15 kV. With appropriate scaling, the actual voltage output was monitored in the range 0-10 V. An instrument was designed to measure the capacitance in pF with the resolution of 0.001 pF. The capacitive measurement was achieved by using the capacitor bridge arrangement shown in figure 5-4b. The instrument contained three capacitors, one of which was tuneable. Along with the SR in the DESA, they form a capacitor bridge. A sensing signal at 10 kHz was generated and inputted to the capacitor bridge. In operation, the SR deforms, and its capacitance changes. As a result, the voltage difference between two pairs of capacitors was measured via a differential amplifier and calibrated to represent the capacitive measure.

For the basic characterization of the DESA, the system was actuated with a sequence of step up/down voltages and the force and the capacitance measurements were monitored. To compare the open and closed loop operations of the DESA, the reference was set to be a step change in the capacitance between the two arbitrarily chosen values, 28.60 pF and 28.55 pF. Each test lasted for 23 s with the voltage applied from t = 3 s. In open-loop operation, the voltage was applied as a step input and its value was pre-determined from prior testing. The closed loop operation of the DESA is explained in figure 5-4c. It is intended to use the error, $E(s)$, between the demand capacitance, $C_d(s)$ and the actual capacitance state, $C(s)$, as the feedback to control the Laplace transformed force output, $F(s)$. The PI controller is defined as

$$G(s) = \frac{V(s)}{E(s)} = K_p + K_i \frac{1}{s} \tag{5.17}$$

where

$$E(s) = C_d(s) - C(s) \tag{5.18}$$

The gains, K_p (V/pF) and K_i (V/pF/s), were tuned iteratively so that when subjecting a step demand of $C_d(s)$, the response in $C(s)$ has a rise time less than 0.5 s and the overshoot is less than 10%. A standard PI controller (K_p = 10 V/pF and K_i = 2 V/pF/s) was used to vary the applied voltage according to the feedback of the capacitance signal. Noting that the control is applied to the capacitance output, for a viscoelastic DE such as polyacrylate, demanding a fast capacitive response also causes significant overshoot in the force output.

5.4 Results and discussion

5.4.1 Closed loop control in force operation

Figure 5-5a shows the step responses of the DESA. The test lasted for 200 s with the applied voltage switching between 0 kV and 8 kV, where the voltage is supplied for 10 s in each cycle of 20 s. It shows that the voltage application corresponds to a relaxation of the DE and decrease in the capacitance in both the long-term and the short-term responses. Over 200 s, the tension force of the pre-strained DE dropped by 0.015 N and the capacitance of the SR dropped by 0.2 pF. In each loading cycle of 10 s, the steady state outputs of the force and the capacitance were calculated between t = 9.5 s, just before the voltage application and at the end, t = 20 s. Figure 5-5a shows the step change force output of the DESA was 0.044 N, and the capacitive change ($\Delta C = C_a - C_0$) was 0.25 pF. For the dynamics of the response, an instant drop of 90% followed by a slow decrease was observed in the force; the corresponding drop was observed as 50% in the capacitance, indicating that the force status responds significantly faster than the capacitance status due to the strong viscoelasticity of the polyacrylate. Figure 5-5b summarizes the net force output of the DESA, F, and the corresponding capacitive strain, λ_{cap}, under the applied voltage of 3 kV to 11 kV. At 11 kV,

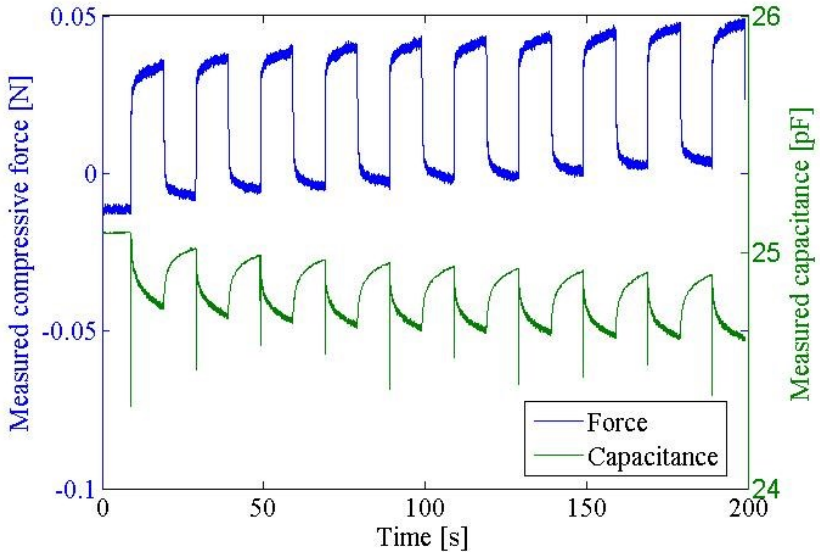

(a)

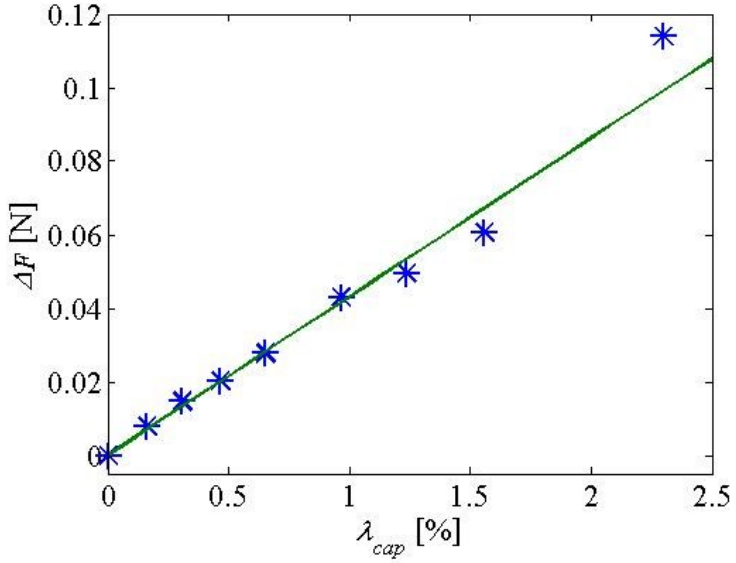

(b)

Figure 5-5: The system responses of the DESA: (a) The step responses of force and capacitance at 8 kV, the spikes in the capacitance are due to interference of the strong electrical field when switching on the HV DC-DC converter at the beginning of each cycle. (b) The net force output against the strain in capacitance with the applied voltage from 3 kV to 11 kV in increment of 1 kV. The linear correlation is in agreement with equation (5.16).

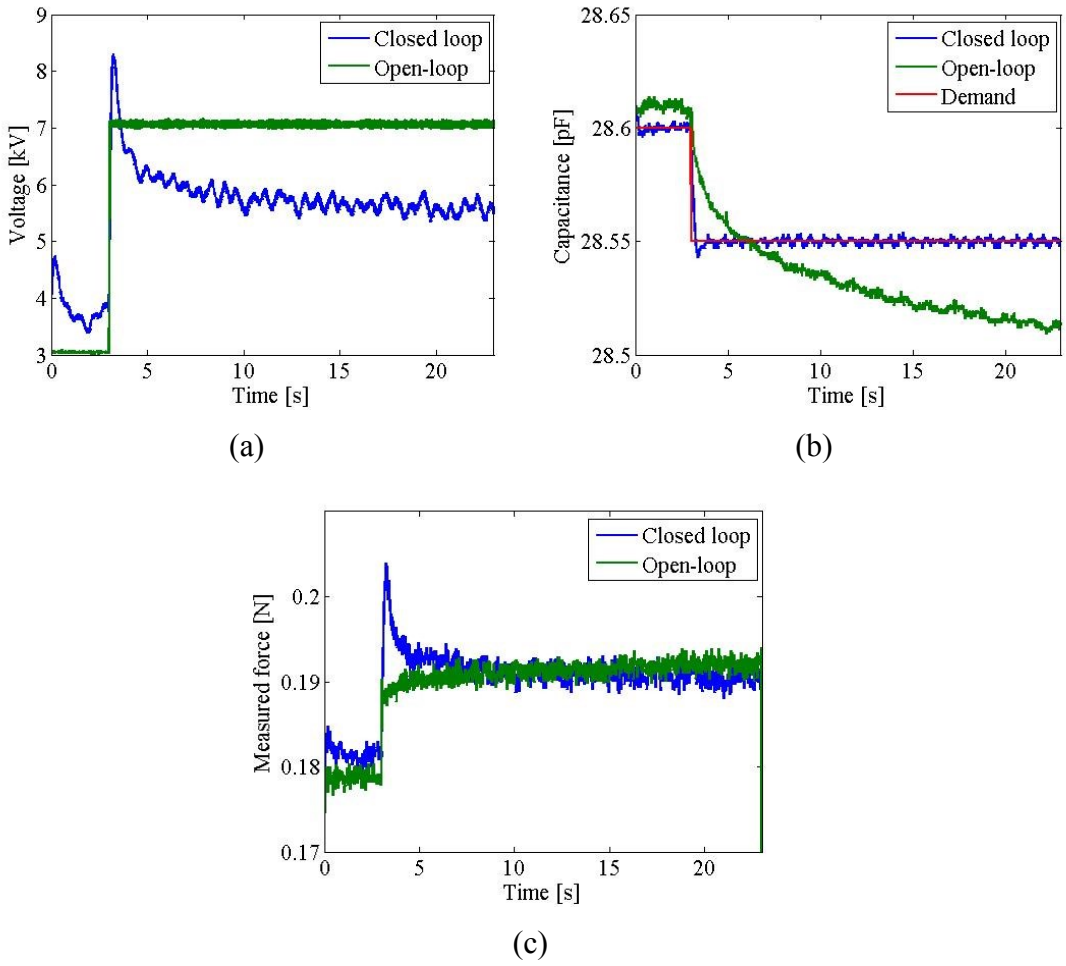

Figure 5-6: System responses in open-loop and closed loop operations (a) the voltage input, (b) the measured capacitance and (c) the measured force.

the actuation generates the force of 0.115 N and the capacitive strain of 2.4%. The relationship between these two outputs were found to be linear, which is in agreement with equation (5.16). Therefore it indicates that in such electrode arrangement, the capacitive change of the SR only correlates the actuation-induced deformation in a single direction.

Figure 5-6 compares the results of both operations. In closed loop operation, the applied voltage rises to 8.5 kV and then decreases slowly to 5.5 kV as in figure 5-6a. In open-loop operation, the applied voltage rises from 3 kV to 7 kV and remains constant. The measured capacitance in the case of closed loop opera-

tion decreases immediately from 28.6 pF to 28.55 pF within 0.5 s; in open-loop operation, it creeps from 28.6 pF towards 28.55 pF over 3 s and continues to decrease towards 28.5 pF as in figure 5-6b. The measured force in the case of the closed loop operation has an overshoot of 0.013 N at $t = 3$ s, it reaches the steady state of 0.19 N and holds in this value from $t = 5$ s. For the open-loop operation, the measured force has an initial rise of 0.01 N and reaches 0.19 N at $t = 10$ s, after which point it continues to increase throughout. The result shows that closed loop operation allows the DESA to react more quickly and suppresses the creeping effects in the capacitive and the force outputs. However, because the polyacrylate is strongly viscoelastic, in order to achieve rapid deformation (e.g. actuation strain), a higher initial voltage is required to deliver a large driving force. As a result, an overshoot of approximately 100% in the force output is observed in figure 5-6c. The force-capacitance correlation in equation (5.16) represents only the steady state of the actuation because equation (5.15) does not include rate-dependency. Therefore the overshoot and the dynamics of the actuation are not predicted by the derived correlation. In contrast, for elastomers such as silicone that behave elastically, because the rate-dependent effect is negligible, the overshoot in the actuation force in such closed loop operation becomes significantly smaller and equation (5.16) holds true for both the dynamic and steady states of the actuation.

5.4.2 Drifting effect in capacitance-strain correlation

Rosset et al. [158] reported that in the position control of the conventional self-sensing DEA, an unexpected drift in the capacitance-strain relationship was reported in the DEA that is made of polyacrylate. In this work, the self-sensing mechanism was applied in controlling a tuneable grating. A rectangular DE was pre-strained and clamped on a rigid frame with the two electrode regions and equipped with a soft grating in the centre. Both of the electrode regions were used for sensing and actuation; the capacitive sensing was used as a feedback for precise control in the deformation of the structure. Given that, the grating was controlled without requiring external sensors. The results showed promising performance in the grating control with standard linear PI controller, despite of

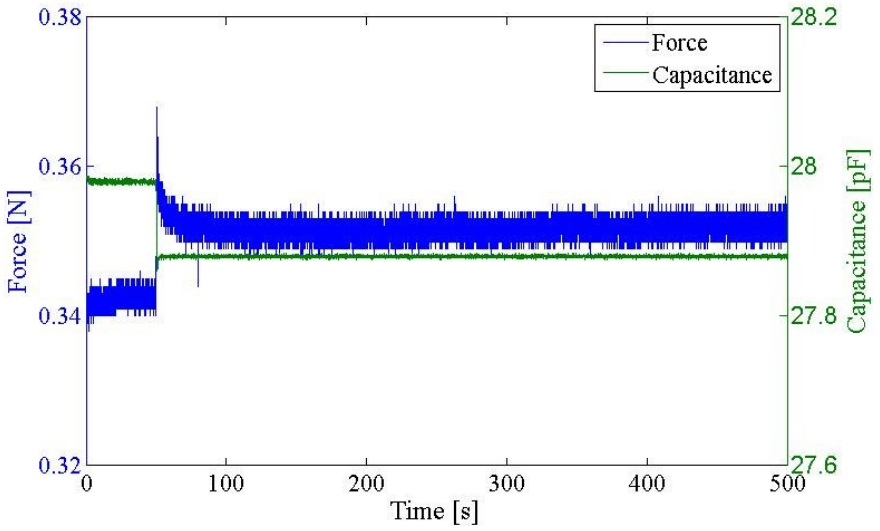

Figure 5-7: Closed loop operation on the DESA over 500 s for the inspection of the potential drifting in capacitance-strain relationship.

the nonlinear relationship between the diffraction angle in the grating and the capacitance of the electrode regions. Rosset et al. [158] also reported that in the polyacrylate-based DEA structure, while the capacitance was held by the closed loop operation, the diffraction angle continues to drop over 400 s. It indicates that the DE relaxes in the long-term and such relaxation is independent of the capacitance of the electrode regions. Further investigation in this work showed that such drift occurred only in the viscous elastomer as the polyacrylate compared with silicone. It was concluded that the drift in the capacitance-strain relationship was due to the rate-dependent behaviour of the permittivity of the polyacrylate when it is subjected to a high electric field.

The same investigation was carried out in the DESA. Figure 7 shows the results of the force and the capacitance over 500 seconds. From $t = 50$ s, the voltage was applied to the AR with the closed loop control. It shows that the capacitance reached the demand value instantly thanks to the PI controller.The force rose correspondingly with an overshoot and settled down within 20 s before reaching the steady state at $t = 70$ s. It shows no drift in the capacitance-strain relationship has occurred after this point. The duration of settlement is significantly shorter

than that of 400 s in [158], which arises since no high electric field is applied directly across the SR during operation. Therefore the rate-dependent behaviour in the permittivity did not occur. The result shows good agreement with the conclusion from [158] and highlights another benefit of the DESA compared with the conventional self-sensing DEA. Because separate electrode regions were used for the actuating and the sensing, the potential high-electric-field-induced dynamics in the material property would not interfere the measurement in capacitance; the DESA is more robust and consistent in the high-voltage DE actuation.

5.4.3 Effect of the electrode

In the AR, the electrode coverage affects the voltage-induced deformation. Since the hand-brushed grease electrode has good compliance with the deformation it tends to provide better actuation performance compared with the hand-painted powder type electrode. Similarly, the particle size of powder type electrode also has impact on the DEA actuation. A non-uniformly distributed electrode may cause concentration of charge and lead to the electric breakdown. The resultant deformation occurs in different levels correspondingly and the profile of the response remains the same throughout. Even when the electrode is poorly coated over the AR, the high operating voltage helps the charge to cross potential gaps and the DEA is still functional.

In contrast, the capacitive sensing was found to depend heavily on the quality of the electrode arrangement. Since controlling the thickness of the electrode is difficult, as indicated in [198], a study was undertaken to investigate the effect of electrode coverage in the capacitive measurement in the undeformed condition. All configurations of the DESA remained the same in this study, the electrodes were painted onto the SR accumulatively over many coating applications from barely covering the whole region to an excessively thick layer (above 1 mm). For each application, approximately the same amount of the additional electrode was added onto both sides of the SR. The applications of electrode addition were continued until the measured capacitance stopped varying significantly. Figure 5-8 shows the capacitance measurement over 25 applications. The measured

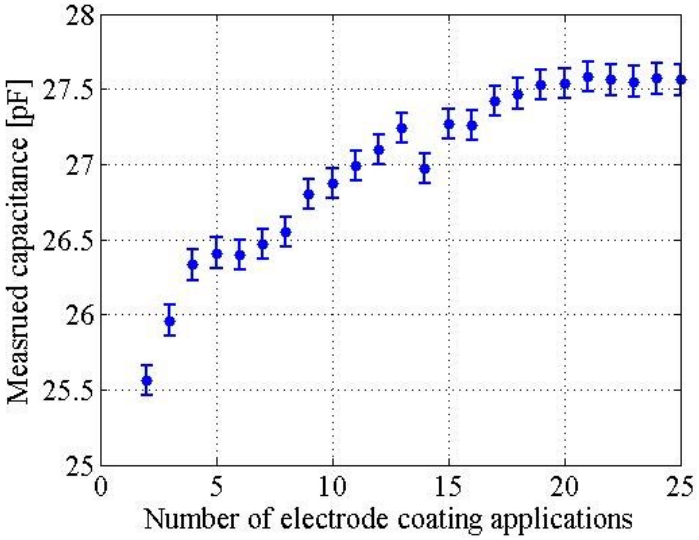

Figure 5-8: The statistics of the capacitive measurements under the electrode coverage that is accumulated over 25 applications.

capacitance was 24.4 pF at the first application. It then continued to rise as more electrode material was accumulated on the SR, and finally

Moreover, the work also found that the electrode migration changes the profile of the capacitive response. As the DE undergoes deformation over a period of time, the electrode was found to reveal that unexpected spots that contain less electrode material existed across the SR. These spots do not exist when the electrode is coated on the DE. It indicates the presence of defect propagation in electrode coating due to the particle migration in the SR. The study was done by performing sinusoidal loading on the DE and monitoring its capacitance throughout. The structure was simplified to have only the SR in the DE. The cyclic strain was set to strain the film from 50% pre-strained to 60%. The electrode coverage was done to assure the sinusoidal response at the beginning of the test. Figure 9 shows the degradation in the capacitive profile as the response no longer remains sinusoidal over cycles. The multiple troughs started to appear after 100 cycles of strain and continued to propagate thereafter. Such testing was done over multiple samples, the unexpected profiles in the capacitive responses were similar but not identical. Also, the occurrence of the degradations varied and depended on the

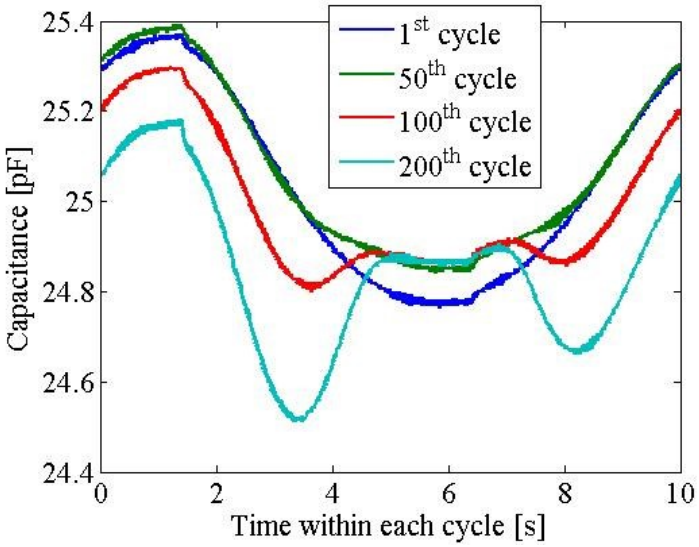

Figure 5-9: The capacitive responses of the DESA under cyclical strain, the profile deviates from the sinusoidal curve over cycles due to the defect propagation in the electrode coating.

configurations of the electrode (e.g. layer thickness and uniformity). It indicates that electrode migration occurs in the small deformation regions. Despite the full understanding of the electrode defect propagation requires further work, an effective solution was to make the electrode layer thicker. It was found experimentally that using a screen to provide the more consistent electrode coating and having the electrode layer of at least 0.3 mm thick ensures the consistent capacitive response over 800 cycles. It also gives the consistent capacitive measurement in the DESA.

5.4.4 Effect of AR-SR aspect ratio

The correlation between the sizes of the SR and the AR also affects the performance of the DESA. By keeping the shape and the width of electrode regions the same, the aspect ratio R of the SR and the AR is defined as

$$R = \frac{l_{SR}}{l_{AR}} \tag{5.19}$$

Hence the overall length of the film l_{tot} can be expressed as

$$l_{tot} = (1 + R + R_d) l_{AR} \tag{5.20}$$

where $R_d l_{AR}$ refers to the part of the film without electrode region in direction 1. Substituting equation (5.20) into (5-6) gives

$$\lambda_{cap}(\lambda_{AR}) = 1 + \frac{1}{R + R_d} - \frac{\lambda_{AR}}{R + R_d} \tag{5.21}$$

The sensing sensitivity of the DESA is defined as

$$S = \frac{\partial \lambda_{cap}}{\partial \lambda_{AR}} = -\frac{1}{R + R_d} \tag{5.22}$$

Equation (5.22) shows that the sensing sensitivity can be improved by decreasing both R and R_d (i.e. enlarge the AR in relative to the passive region and SR). It also benefits the actuation capability of the DESA since having the SR does not require to compromise the size of the AR.

Theoretically, the sensing sensitivity can be optimised by having a significantly high aspect ratio. However, the actual lower limit of R depends on the instrument for the capacitive measure as indicated in equation (5.4). As the area of the SR becomes smaller, the capacitance of the SR decreases and becomes more difficult to measure as it approaches the level of the noise. The capacitor bridge was developed for the capacitive measure in pF precisely. The trade-off is that it is also very sensitive to the noises from the environment. The actual lower limit of R_d depends on the spacing gap between the AR and the SR. When the DESA is in operation, electric breakdown is the primary concern in determining the gap distance. If breakdown occurs, the high voltage from the AR causes arcs onto the SR, which interferes with the capacitive measure and damages the instrument.

Therefore the breakdown strength of the environment (i.e. air in this case) must be considered. Moreover, the strong electrical field from the AR fluxes through both the elastomer and the environment. As the SR lays closer to the AR, such unexpected electrical field is received by the SR and interferes the capacitive measurement as shown in figure 5-5a. The noise level increases when the voltage is applied. In this work for DEA operating in the air, the gap distance of 15 mm was found to be safe for the applied voltage up to 15 kV.

5.4.5 Effect of motion constraining

While the passive region between the electroded regions arises from necessity, the constraints can be applied to further enhance the sensing sensitivity of the DESA. By constraining the deformation of the passive region, the voltage-induced expansion in the AR corresponds to the larger compression in the SR, therefore higher sensing sensitivity. Since this part of the DE no longer deforms during the operation, the effect of such motion-constraint can be expressed as a decrease in R_d in equation (5.22). The remaining passive region would be those between electrode regions and clamps, which could be constrained similarly. In the ideal case, all the passive regions in the DE are fixed in dimension as $R_d = 0$, substituting it into equation (5.22) gives

$$S = \frac{\lambda_{cap}}{\lambda_{AR}} = -\frac{1}{R} \tag{5.23}$$

Equation (5.23) indicates that the sensitivity S depends solely on R and becomes more sensitive to the change in R, correspondingly. Furthermore, applying such constraint to the DE also enhances actuation performance in the AR by constraining its expansion in direction 2 [199].

Figure 5-10 shows the actual DESA in the unconstrained and constrained conditions. Figures 5-11a and 5-11b show the force and capacitance responses of the DESA under the step voltage input from 6 kV to 10 kV. The improvement in the outputs due to the motion-constraint was by a factor of 3. In this work, a layer of the PE film was used to serve the purpose without compromising the

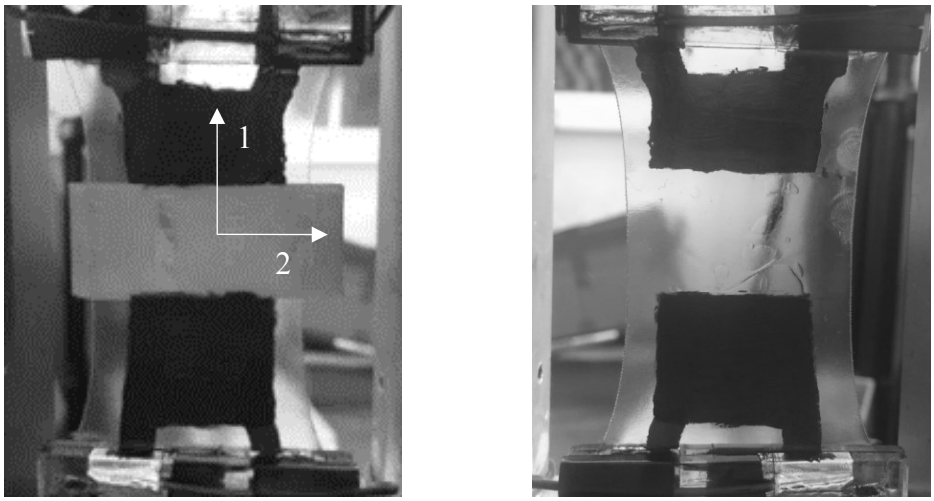

Figure 5-10: The actual DESAs (a) with constraint and (b) without constraint.

flexibility of the DESA. However, such a flexible constraint requires careful application so that the constrained passive region remains in-plane. The curvature and the misalignment vary the capacitance-strain relationship and cause errors in sensing. Finally, the employed constraint is required to be as light as possible so that the additional mass does not result in undesired resonance and interferes the system dynamics significantly.

5.4.6 Wrinkling detection of the DESA

The DESA shows the promising performance when the AR undergoes deformation strains up to 10%. Recalling the stress-strain relationship of a typical DE, the snap point in the stress-strain curve is delayed as the DE is pre-strained [97]. Such change in the material property allows the DE to deform significantly larger under the same applied voltage without the electric breakdown [111]. Because the resultant local strain in the AR becomes excessive, it causes out-of-plane deformation in the AR, namely wrinkling. The relationship between the capacitive strain in the SR and the mechanical strain in the AR as in equation (104) differs as the result.

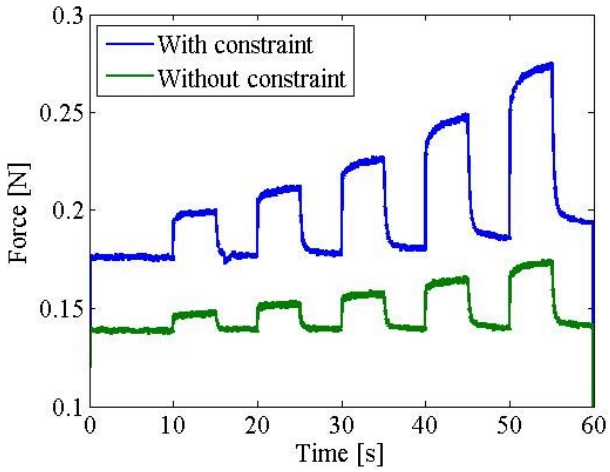

(a)

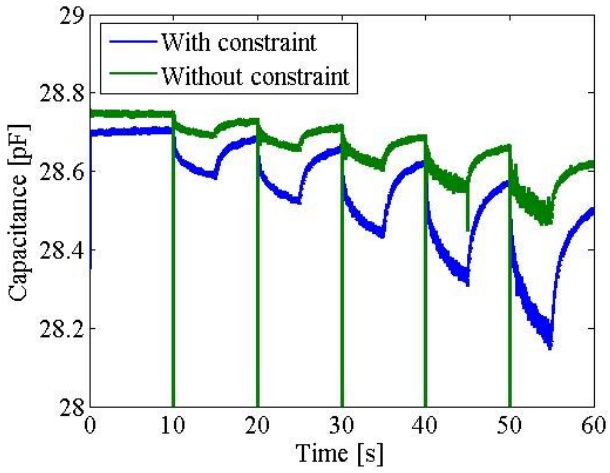

(b)

Figure 5-11: Comparison between the DESAs with and without constraint (a) force response and (b) capacitance response.

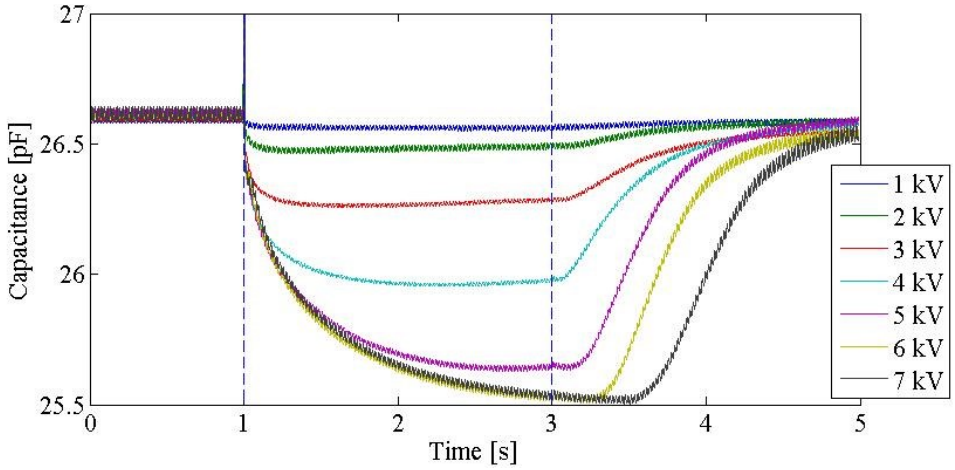

Figure 5-12: The step responses of the actuation in the largely pre-strained DESA that is associated with the occurrence of the out-of-plane deformation.

Regarding this, a study was done to investigate the sensing limitation of the DESA against the voltage-induced wrinkling. To do so, a DE was pre-strained bi-axially with $\lambda_{1,pre} = 2$, $\lambda_{2,pre} = 2$ and mounted on a rectangular rigid frame. The AR is 15 mm×50 mm and the SR is 10 mm × 10 mm. The SR was designed to be relatively small and aligned with the AR in direction 1 so that the SR senses the largest local deformation of the central AR. Copper foils were wrapped on the frame for the electrode contract. The voltages were applied to the DESA as step inputs for 2 s from $t = 1$ s, the capacitance was monitored for 5 s in each test. In order to cause wrinkling within the achievable input voltage, the DESA was pre-strained equally in both directions to lower further the thickness of the film. Changing the pre-loading condition varies only actuation strains in planar directions [96]. Equations (5.1), (5.3), (5.6) and (5.16) therefore still hold in the equal-biaxial loading condition.

Figure 5-12 shows the capacitive responses that are associated with wrinkled actuation at different voltages. At 1 kV, the capacitance reached the steady state within 0.1 s at $t = 1$ s. At $t = 3$ s, the capacitive response rises back over 0.5 s. At 4 kV, it took 0.5 s for the capacitance to reach the steady-state when activating the AR, and over 1 s to recover from the actuation from $t = 3$ s. It shows that as the voltage increases further, the capacitance takes longer to reach the steady

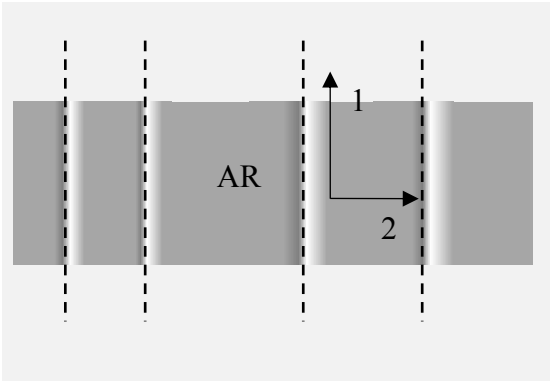

(a)

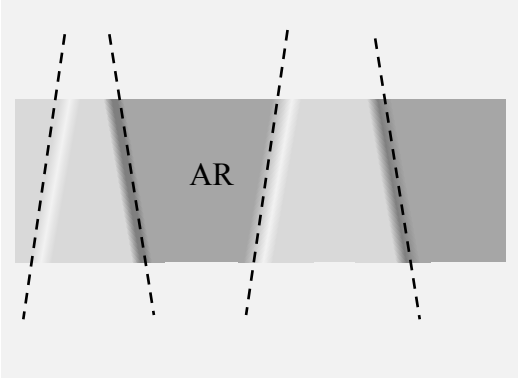

(b)

Figure 5-13: Illustration of the change in the wrinkling as the applied voltage increases: (a) Wrinkling occurs only in one direction and is aligned in direction 1 at 5 kV and (b) At higher applied voltage ($>$ 5 kV), the wrinkling occurs in both planar directions and forms prismatic sub-regions.

state and its static output approaches a saturation value. In the experiment, it was observed that the wrinkling occurred initially in direction 2 at 5 kV, indicating excessive strain only in direction 1. As the voltage increased further, the wrinkling became prismatic as it propagated in both planar directions as in figure 5-13. Either way, it causes additional lag in recovering from the wrinkled actuation. During the recovery, the geometry of the SR remains unaffected, in which case the large deformation in the AR can no longer be detected by the capacitive change in the SR. For example, the more significant wrinkling occurred at 7 kV and took over 2 s to recover; the measured capacitive change of 1 pF remains the same as that at 6 kV. Therefore, the two following features make the DESA provide informative feedback about wrinkling, which can be used for holding the actuation within the in-plane state to avoid the potential failure.

A1. Capacitive change stops increasing when increasing the applied voltage (e.g. the saturation in capacitance)

A2. Capacitive change decreases with a significant time delay when decreasing the applied voltage (e.g. significant time delay).

5.5 Conclusions

This chapter concludes that a robust and reliable capacitive self-sensing mechanism for DE actuation is feasible. In this work, the structure of a new DESA design is proposed that features a self-sensing mechanism. Compared with a conventional self-sensing DEA, the DESA consists of multiple electrode regions for sensing and actuation. In operation, the voltage is applied on the AR for actuation, and the capacitance of the SR is measured and used as feedback in the force control. Because of this, the sensing by the SR detects only the deformation of the structure in a single direction. An instrument based on a capacitor bridge was designed for the capacitive measurement. For a step input of voltage in kV, the resultant capacitive change was measured on the scale of 0.1 pF. In the polyacrylate-based DESA, the closed loop operation shows the promising performance in achieving the fast response and suppressing the relaxation. The

drawback in achieving rapid response in the capacitance is that it also causes an overshoot in force output due to the strong viscoelasticity of the polyacrylate.

For the electrode coating of the DESA, the capacitive measurement is very sensitive to the electrode coverage in the SR for the grease type electrode. Without the high electric field, good conductivity is necessary for the charges to spread across the entire SR. Poor electrode coverage and defects in electrode coating lead to the unexpected capacitive response. Increasing the thickness of the electrode layer is one option to improve the electrode coverage effectively. Also, it shows that the performance of the DESA can be further enhanced by:

B1. Varying the aspect ratio of the electrode regions

B2. Utilizing motion-constraint.

These factors benefit both the sensing and the actuation of the DESA. Furthermore, the study shows that the DESA structure does not suffer from the rate-dependent permittivity due to high electric field compared that was observed in the conventional self-sensing DEA. It makes the DESA operate more consistently over a broad range of operating voltage. Finally, the DESA shows distinct capacitance responses between linear and the nonlinear actuation, which can be exploited for detecting the excessive local strain in the AR.

Chapter 6

Conclusions and future work

Dielectric elastomers (DEs) are in a special class of electro-active polymers with excellent electromechanical properties. Dielectric elastomer actuators (DEAs) consist of thin DE films coated with electrodes and generate deformation under high voltages. They offer actuation capability that is similar to that of human muscle. However, the development of DEAs for commercial applications has been hindered due to the high voltage requirement, small force output, nonlinear material characteristics and lack of a reliable sensing mechanism for precise motion control. This thesis has focused on three specific areas of DE actuation: performance enhancement; accurate modelling; and self-sensing control.

A major conclusion in performance enhancement is that a combination of two enhancement techniques, pre-straining and motion constraining, improves significantly the actuation capability of a DEA. A rod-prestrained dielectric elastomer actuator (RP-DEA) was developed, utilising metallic rods to hold the pre-strained DE film in-plane and to constrain deformation in the lateral direction to actuation. The investigation was undertaken to study the effect of bi-axial pre-loading on force output of a conventional DEA, compared with that from a RP-DEA. The derived correlation between the pre-straining and the force output of the DEA was found to fit the experimental data well, covering pre-strain variations up to 200%. The study demonstrated that the actuation force output of the RP-DEA can be over ten times larger than that of a conventional DEA.

The first RP-DEA design was found to have a short operational time due to occurrence of premature failure. Two sources of failure were identified in this work. The primary failure source is the non-uniform deformation of the DE film in the RP-DEA. It creates weak regions having low thickness close to the rods, which are vulnerable locally to breakdown voltages. The secondary cause is the in-AR lead contact. The tips that contact the DE have better conductivity than the electrode material, which may concentrate charge and lead to excessive local electrical fields. The in-AR contact was found to have lower impact on the durability of the RP-DEA compared with the primary weak region. Finite element simulation in discrete steps was performed to simulate the large material deformation of the RP-DEA during the fabrication process, confirming the non-uniformity in thickness across the film and presence of the primary "weak" region.

Both sources of failure were suppressed by locating the AR outside the "weak" regions. The results show that this approach for AR optimisation stabilises the RP-DEA and improves its durability significantly. The results also show that the AR optimisation led to only a minor reduction in force output. Further work is suggested in the life assessment of the RP-DEA with non-conductive rods to assess fully the influence of rod conductivity. The simulation model could be improved further by performing a single continuous simulation, rather than the discrete steps reported in Chapter 3. A locally defined DE elastic modulus that varies with non-uniform deformation would also be more representative in the finite element model.

The study of dynamic characteristics shows that the essential influence of viscoelasticity in the functionality of the DE and DE-based actuator. The study demonstrates that compared with spring-like silicone, viscoelastic polyacrylate has increased stiffness and delay in deformation at high frequencies. In electrical actuation, polyacrylate requires more effort to deform at high frequencies and therefore generates smaller actuation force under the same driving voltage. The conventional Kelvin-Voigt model considers DE as one spring and one spring-damper combination in parallel. The study showed its deficiency in simulating polyacrylate. The use of higher order Maxwell-Wiechert material models that contain multiple spring-damper combinations leads to more accurate representation of the viscoelastic characteristics of dielectric polymers. Compared with

a conventional first-order model, the higher order representation allows the system dynamics to be shaped over frequency ranges. They offer more degrees of freedom in the parameter identification process, which leads to more accurate determination of the frequency response. An iterative procedure was devised to guide the parameter identification such that magnitude and phase error bounds are within specified tolerances.

To demonstrate the model identification, two dielectric polymers, silicone and polyacrylate, were used. They were configured in a single-layer sheet format for higher frequency testing during which the mechanical strain variations were less than 10%, thus avoiding buckling of the sheet during the cyclic loading. Lower frequency testing with strain variations above 10% were also performed using stacked layers of the polyacrylate, to eliminate the occurrence of buckling during the cyclic loading. The polymer cyclic forces were measured using load cells. The combination of low level forces and the low stiffness of the load cell used during the higher frequency testing led to resonance being experienced within the frequency range. A correction procedure was therefore implemented in which the inertia forces and load cell deflections were accounted for and eliminated from the dynamic frequency response measurements to reveal the characteristics of the polymer samples alone.

The experimental results and parameter identification for the silicone sample under mechanical loading indicated that a first-order model is appropriate, which is due to the spring-like behaviour of the polymer material. However, the polyacrylate samples required third-order models to achieve suitable accuracy to represent the viscoelastic characteristics. For the polyacrylate, third-order models improved the accuracy in dynamic modelling by 80% compared with the conventional first-order model. The proposed higher order modelling and parameter identification should prove useful in the model-based control for polymer-based soft robotic systems.

A novel self-sensing mechanism was proposed in a dielectric elastomer self-sensed actuator (DESA). Compared with a conventional self-sensing DEA, the DESA consists of multiple electrode regions for sensing and actuation. In operation, the voltage was applied on the AR for actuation, and the capacitance of the SR was

measured and used as feedback in force control. Because the AR and the SR are aligned in the direction of actuation and separated in the DESA, the sensing by the SR detects only the deformation of the structure in a single direction. An instrument circuit based on a capacitor bridge was designed for the capacitive measurement. For a step input of voltage of around 7 kV, the resultant capacitive change was measured on the scale of 0.1 pF. In the polyacrylate-based DESA, the closed loop operation shows promising performance in achieving the fast response and suppressing the relaxation. The drawback in achieving rapid response in the capacitance is that it also causes an overshoot in force output due to the strong viscoelasticity of the polyacrylate.

For the electrode coating of the DESA, the capacitive measurement was very sensitive to the electrode coverage in the SR for the grease type electrode. Without the high electric field, good conductivity is necessary for charge to spread across the entire SR. Poor electrode coverage and defects in electrode coating led to unexpected capacitive response. Increasing the thickness of the electrode layer is one option to improve the electrode coverage. Also, it shows that the performance of the DESA can be enhanced by varying the aspect ratio of the electrode regions and utilising motion-constraint. With the insight from Chapter 3, it shows that the enhancement techniques boost both sensing and actuation performance of DE devices.

The greatest advantage of the self-sensing mechanism, compared with the conventional one, is that it does not require the excitation signal to be superposed with the driving voltage for the estimation of capacitance. Therefore, it can be implemented at low cost with with any high voltage power supply. The study also showed that the DESA structure does not suffer from the rate-dependent permittivity due to high electric field compared that was observed in the conventional self-sensing DEA. It allows the DESA to operate more consistently over a broad range of operating voltage. Finally, the DESA features uniquely informative sensing, showing distinct capacitance responses between linear and the nonlinear actuation (e,g, wrinkling) which can be exploited for detecting excessive local strain in the AR.

This thesis demonstrates the promising performance and high potential of DE actuators. In order to advance even further, future research could be explored in the follow areas:

- Multi-axial DE actuators. With the established understanding in uni-axial DE actuation, it could be expanded to multiple axes to counter complex tremor motion.
- Model-based control of DE actuation. Following up the generated higher material model, model-based control could be implemented to demonstrate the effectiveness in compensating for vibration.
- Multi-layer DE actuators. Single-layer actuators are comparable with muscle fibres inside a muscle bundle. Adding more fibres would scale up the actuation capability, but also encounter new challenges such as voltage isolation and motion synchronisation between elements. Multi-layer DE actuators may, therefore, require different structures, electrode configurations and circuit designs.
- In-vitro and in-situ tremor suppression via DE actuation. As the DEA has been proven to be suitable for such application, the next step is to develop a wearable device.
- Self-powered DE actuators. As a DE actuator can be self-sensed, it may also be self-powered by harvesting energy from tremor or vibratory motion.
- DE actuation with reduced driving voltage. High voltage power supplies tend to exhibit current discharge, as demonstrated in Chapter 4. It limits the dynamics of driving voltage for operation at high frequencies, which may potentially limit DE actuation in tremor suppression. By making the DE film thinner, DE actuator could be driven by voltages up to 100 V.
- DE actuation with an optimal DE elastomer. One DE elastomer may exhibit a significant dielectric constant at the expense of high dielectric strength, or vice versa. The same contrast may occur with elastic modulus and viscoelasticity. A better balance between properties would benefit applications at high frequencies such as for tremor suppression.

List of publications

Journal articles

I Zhang, R., Huang, X., Li, T., Iravani, P., and Keogh, P., "Novel arrangements for high performance and durable dielectric elastomer actuation," *Actuators*, vol. 5, no. 3, 2016

II Zhang, R., Iravani, P., and Keogh, P., "Closed loop control of force operation in a novel self-sensing dielectric elastomer actuator," *Sensors and Actuators A: Physical*, vol. 264, no. Supplement C, pp. 123-132, 2017

III Zhang, R., Iravani, P., and Keogh, P., "Dielectric elastomer actuator modelling using higher order material characteristics," *Journal of Physics Communications*, Under revision

Conference paper

I Zhang, R., Iravani, P., and Keogh, P.,"Experimental characterization of dielectric elastomer actuator," 2017.

References

[1] Deuschl, G., Bain, P., and Brin, M., "Consensus statement of the movement disorder society on tremor," *Movement Disorders*, vol. 13, no. SUPPL. 3, pp. 2–23, 1998.

[2] Benito-Len, J. and Labiano-Fontcuberta, A., "Linking essential tremor to the cerebellum: Clinical evidence," *Cerebellum*, vol. 15, no. 3, pp. 253–262, 2016.

[3] Louis, E., Benito-Len, J., Vega-Quiroga, S., and Bermejo-Pareja, F., "Faster rate of cognitive decline in essential tremor cases than controls: A prospective study," *European Journal of Neurology*, vol. 17, no. 10, pp. 1291–1297, 2010.

[4] Ondo, W., Sutton, L., Dat Vuong, K., Lai, D., and Jankovic, J., "Hearing impairment in essential tremor," *Neurology*, vol. 61, no. 8, pp. 1093–1097, 2003.

[5] Jankovic, J., "Essential tremor: A heterogenous disorder," *Movement Disorders*, vol. 17, no. 4, pp. 638–644, 2002.

[6] Louis, E. and Ferreira, J., "How common is the most common adult movement disorder? update on the worldwide prevalence of essential tremor," *Movement Disorders*, vol. 25, no. 5, pp. 534–541, 2010.

[7] Elble, R., "What is essential tremor?," *Current neurology and neuroscience reports*, vol. 13, no. 6, p. 353, 2013.

[8] Bartels, A. and Leenders, K., *Imaging in Parkinson's Disease*, ch. Effects of Surgical Treatment. Oxford University Press, 2011.

[9] Akano, E., Zesiewicz, T., and Elble, R., "Fahntolosamarin scale, digitizing tablet and accelerometry have comparable minimum detectable change," *Movement Disorders*, vol. 30, no. Suppl 1, p. 4176, 2015.

[10] *C-leg power prosthetics*, Assessed October 7, 2015. `http://www.prostheticsinmotion.com/technology.html`.

[11] *Walk assist and mobility devices*, Assessed September 24, 2015. `http://corporate.honda.com/innovation/walk-assist/`.

[12] *XOS exoskeleton*, Assessed October 7, 2015. `http://www.army-technology.com/projects/raytheon-xos-2-exoskeletonus/`.

[13] *HULC exoskeleton*, Assessed October 7, 2015. `http://www.lockheedmartin.co.uk/us/products/hulc.html`.

[14] Shorter, K., Kogler, G., Loth, E., Durfee, W., and Hsiao-Wecksler, E., "A portable powered ankle-foot orthosis for rehabilitation," *Journal of Rehabilitation Research and Development*, vol. 48, no. 4, pp. 459–472, 2011.

[15] Calzetti, S., Baratti, M., Gresty, M., and Findley, L., "Frequency/amplitude characteristics of postural tremor of the hands in a population of patients with bilateral essential tremor: Implications for the classification and mechanism of essential tremor," *Journal of Neurology, Neurosurgery and Psychiatry*, vol. 50, no. 5, pp. 561–567, 1987.

[16] Daerden, F. and Lefeber, D., "Pneumatic artificial muscles: Actuators for robotics and automation," *European Journal of Mechanical and Environmental Engineering*, vol. 47, no. 1, pp. 11–21, 2002.

[17] Li, B., Chen, H., Qiang, J., Sheng, J., and Zhou, J., "Effect of viscoelastic relaxation on the electromechanical coupling of dielectric elastomer," *Proceedings of SPIE - The International Society for Optical Engineering*, vol. 8687, 2013.

[18] Pelrine, R., Larsen, P., Kornbluh, R., Heydt, R., Kofod, G., Pei, Q., and Gravesen, P., "Applications of dielectric elastomer actuators," *Proceedings of SPIE - The International Society for Optical Engineering*, vol. 4329, no. 1, pp. 335–349, 2001.

[19] Kornbluh, R., Pelrine, R., Pei, Q., Heydt, R., Stanford, S., Oh, S., and Eckerle, J., "Electroelastomers: Applications of dielectric elastomer transducers for actuation, generation and smart structures," *Proceedings of SPIE - The International Society for Optical Engineering*, vol. 4698, pp. 254–270, 2002.

[20] Pei, Q., Pelrine, R., Rosenthal, M., Stanford, S., and Prahlad, H., "Recent progress on electroelastomer artificial muscles and their application for biomimetic robots," *Proceedings of SPIE - The International Society for Optical Engineering*, vol. 5385, pp. 41–50, 2004.

[21] Plante, J. S., Dubowsky, S., Santer, M., and Pellegrino, S., "Compliant bistable dielectric elastomer actuators for binary mechatronic systems," *Proceedings of the ASME International Design Engineering Technical Conferences and Computers and Information in Engineering Conference - DETC2005*, vol. 7 A, pp. 121–126, 2005.

[22] Moscardo, M., Zhao, X., Suo, Z., and Lapusta, Y., "On designing dielectric elastomer actuators," *Journal of Applied Physics*, vol. 104, no. 9, 2008.

[23] Pei, Q., Pelrine, R., Stanford, S., Kornbluh, R., and Rosenthal, M., "Electroelastomer rolls and their application for biomimetic walking robots," *Synthetic Metals*, vol. 135-136, pp. 129–131, 2003.

[24] Zhang, R., Lochmatter, P., Kunz, A., and Kovacs, G., "Spring roll dielectric elastomer actuators for a portable force feedback glove," *Proceedings of SPIE - The International Society for Optical Engineering*, vol. 6168, 2006.

[25] Carpi, F., Salaris, C., and De Rossi, D., "Folded dielectric elastomer actuators," *Smart Materials and Structures*, vol. 16, no. 2, pp. S300–S305, 2007.

[26] Kovacs, G. and Dring, L., "Contractive tension force stack actuator based on soft dielectric eap," *Proceedings of SPIE - The International Society for Optical Engineering*, vol. 7287, 2009.

[27] Zhen, Z., Liwu, L., Gang, D., Shouhua, S., Yanju, L., and Jinsong, L., "Silicone dielectric elastomers filled with carbon nanotubes andactuator," *Proceedings of SPIE - The International Society for Optical Engineering*, vol. 7287, 2009.

[28] Pelrine, R., Kornbluh, R., and Joseph, J., "Electrostriction of polymer dielectrics with compliant electrodes as a means of actuation," *Sensors and Actuators, A: Physical*, vol. 64, no. 1, pp. 77–85, 1998.

[29] Schlaak, H., Jungmann, M., Matysek, M., and Lotz, P., "Novel multilayer electrostatic solid-state actuators with elastic dielectric," *Proceedings of SPIE - The International Society for Optical Engineering*, vol. 5759, pp. 121–133, 2005.

[30] Carpi, F., Migliore, A., Serra, G., and De Rossi, D., "Helical dielectric elastomer actuators," *Smart Materials and Structures*, vol. 14, no. 6, pp. 1210–1216, 2005.

[31] Pei, Q., Rosenthal, M., Stanford, S., Prahlad, H., and Pelrine, R., "Multiple-degrees-of-freedom electroelastomer roll actuators," *Smart Materials and Structures*, vol. 13, no. 5, 2004.

[32] Choi, H., Jung, K., Ryew, S., Nam, J.-D., Jeon, J., Koo, J., and Tanie, K., "Biomimetic soft actuator: Design, modeling, control, and applications," *IEEE/ASME Transactions on Mechatronics*, vol. 10, no. 5, pp. 581–593, 2005.

[33] Jung, K., Koo, J., Nam, J.-D., Lee, Y., and Choi, H., "Artificial annelid robot driven by soft actuators," *Bioinspiration and Biomimetics*, vol. 2, no. 2, 2007.

[34] Carpi, F., De Rossi, D., Kornbluh, R., and Pelrine, R., *Dielectric elastomers as electromechanical transducers*, ch. Electromechanical transduction effects

in dielectric elastomers: actuation, sensing, stiffness modulation and electric energy generation. Elsevier Ltd, 2008.

[35] Chouinard, P. and Plante, J. S., "Bistable antagonistic dielectric elastomer actuators for binary robotics and mechatronics," *IEEE/ASME Transactions on Mechatronics*, vol. 17, no. 5, pp. 857–865, 2012.

[36] Yu, Z., Yuan, W., Brochu, P., Chen, B., Liu, Z., and Pei, Q., "Large-strain, rigid-to-rigid deformation of bistable electroactive polymers," *Applied Physics Letters*, vol. 95, no. 19, 2009.

[37] Conn, A. and Rossiter, J., "Towards holonomic electro-elastomer actuators with six degrees of freedom," *Smart Materials and Structures*, vol. 21, no. 3, 2012.

[38] Jordi, C., Michel, S., and Fink, E., "Fish-like propulsion of an airship with planar membrane dielectric elastomer actuators," *Bioinspiration and Biomimetics*, vol. 5, no. 2, 2010.

[39] Kofod, G., Wirges, W., Paajanen, M., and Bauer, S., "Energy minimization for self-organized structure formation and actuation," *Applied Physics Letters*, vol. 90, no. 8, 2007.

[40] O'Brien, B., McKay, T., Calius, E., Xie, S., and Anderson, I., "Finite element modelling of dielectric elastomer minimum energy structures," *Applied Physics A: Materials Science and Processing*, vol. 94, no. 3, pp. 507–514, 2009.

[41] Chiba, S., Waki, M., Kornbluh, R., and Pelrine, R., "Extending applications of dielectric elastomer artificial muscle," *Proceedings of SPIE - The International Society for Optical Engineering*, vol. 6524, 2007.

[42] Hochradel, K., Rupitsch, S., Sutor, A., Lerch, R., Vu, D., and Steinmann, P., "Dynamic performance of dielectric elastomers utilized as acoustic actuators," *Applied Physics A: Materials Science and Processing*, vol. 107, no. 3, pp. 531–538, 2012.

[43] Aschwanden, M. and Stemmer, A., "Low voltage, highly tunable diffraction grating based on dielectric elastomer actuators," *Proceedings of SPIE - The International Society for Optical Engineering*, vol. 6524, 2007.

[44] Carpi, F., Frediani, G., Turco, S., and De, R., "Bioinspired tunable lens with muscle-like electroactive elastomers," *Advanced Functional Materials*, vol. 21, no. 21, pp. 4152–4158, 2011.

[45] Aschwanden, M., Niederer, D., and Stemmer, A., "Tunable transmission grating based on dielectric elastomer actuators," *Proceedings of SPIE - The International Society for Optical Engineering*, vol. 6927, 2008.

[46] Kollosche, M., Dring, S., Stumpe, J., and Kofod, G., "Voltage-controlled compression for period tuning of optical surface relief gratings," *Optics Letters*, vol. 36, no. 8, pp. 1389–1391, 2011.

[47] Beck, M., Fiolka, R., and Stemmer, A., "Variable phase retarder made of a dielectric elastomer actuator," *Optics Letters*, vol. 34, no. 6, pp. 803–805, 2009.

[48] Opris, D., Molberg, M., Walder, C., Ko, Y., Fischer, B., and Nesch, F., "New silicone composites for dielectric elastomer actuator applications in competition with acrylic foil," *Advanced Functional Materials*, vol. 21, no. 18, pp. 3531–3539, 2011.

[49] Carpi, F., Frediani, G., Tarantino, S., and De Rossi, D., "Millimetre-scale bubble-like dielectric elastomer actuators," *Polymer International*, vol. 59, no. 3, pp. 407–414, 2010.

[50] Lee, S., Jung, K., Koo, J., Lee, S., Choi, H., Jeon, J., Nam, J., and Choi, H., "Braille display device using soft actuator," *Proceedings of SPIE - The International Society for Optical Engineering*, vol. 5385, pp. 368–379, 2004.

[51] Wu, J., Zang, J., Rathmell, A., Zhao, X., and Wiley, B., "Reversible sliding in networks of nanowires," *Nano Letters*, vol. 13, no. 6, pp. 2381–2386, 2013.

[52] Giousouf, M. and Kovacs, G., "Dielectric elastomer actuators used for pneumatic valve technology," *Smart Materials and Structures*, vol. 22, no. 10,

2013.

[53] Herr, H. and Kornbluh, R., "New horizons for orthotic and prosthetic technology: Artificial muscle for ambulation," *Proceedings of SPIE - The International Society for Optical Engineering*, vol. 5385, pp. 1–9, 2004.

[54] Rajamani, A., Grissom, M., Rahn, C., and Zhang, Q., "Wound roll dielectric elastomer actuators: Fabrication, analysis, and experiments," *IEEE/ASME Transactions on Mechatronics*, vol. 13, no. 1, pp. 117–124, 2008.

[55] Carpi, F. and De Rossi, D., "Improvement of electromechanical actuating performances of a silicone dielectric elastomer by dispersion of titanium dioxide powder," *IEEE Transactions on Dielectrics and Electrical Insulation*, vol. 12, no. 4, pp. 835–843, 2005.

[56] Carpi, F., Migliore, A., and De Rossi, D., "A new contractile linear actuator made of dielectric elastomers," *Proceedings of SPIE - The International Society for Optical Engineering*, vol. 5759, pp. 64–74, 2005.

[57] Plante, J.-S., *Dielectric elastomer actuators for binary robotics and mechatronics*. PhD thesis, Massachusetts Institute of Technology, 2006.

[58] Biddiss, E. and Chau, T., "Dielectric elastomers as actuators for upper limb prosthetics: Challenges and opportunities," *Medical Engineering and Physics*, vol. 30, no. 4, pp. 403–418, 2008.

[59] Ha, S., Yuan, W., Pei, Q., Pelrine, R., and Stanford, S., "New high-performance electroelastomer based on interpenetrating polymer networks," *Proceedings of SPIE - The International Society for Optical Engineering*, vol. 6168, 2006.

[60] Kovacs, G., Lochmatter, P., and Wissler, M., "An arm wrestling robot driven by dielectric elastomer actuators," *Smart Materials and Structures*, vol. 16, no. 2, 2007.

[61] Bolzmacher, C., Biggs, J., and Srinivasan, M., "Flexible dielectric elastomer actuators for wearable human-machine interfaces," *Proceedings of SPIE -*

The International Society for Optical Engineering, vol. 6168, 2006.

[62] Zhang, R., Lochmatter, P., Kunz, A., and Kovacs, G., "Dielectric elastomer spring roll actuators for a portable force feedback device," *14th Symposium onHaptics Interfaces for Virtual Environment andTeleoperator Systems 2006 - Proceedings*, vol. 2006, pp. 347–353, 2006.

[63] Bauer, S. and Paajanen, M., "Electromechanical characterization and measurement protocol for dielectric elastomer actuators," *Proceedings of SPIE - The International Society for Optical Engineering*, vol. 6168, 2006.

[64] Ma, W. and Cross, L., "An experimental investigation of electromechanical response in a dielectric acrylic elastomer," *Applied Physics A: Materials Science and Processing*, vol. 78, no. 8, pp. 1201–1204, 2004.

[65] Wissler, M. and Mazza, E., "Modeling and simulation of dielectric elastomer actuators," *Smart Materials and Structures*, vol. 14, no. 6, pp. 1396–1402, 2005.

[66] Pelrine, R., Kornbluh, R., Eckerle, J., Jeuck, P., Oh, S., Pei, Q., and Stanford, S., "Dielectric elastomers: Generator mode fundamentals and applications," *Proceedings of SPIE - The International Society for Optical Engineering*, vol. 4329, pp. 148–156, 2001.

[67] Yurchenko, D., Val, D., Lai, Z., Gu, G., and Thomson, G., "Energy harvesting from a de-based dynamic vibro-impact system," *Smart Materials and Structures*, vol. 26, no. 10, 2017.

[68] Yurchenko, D., Lai, Z., Thomson, G., Val, D., and Bobryk, R., "Parametric study of a novel vibro-impact energy harvesting system with dielectric elastomer," *Applied Energy*, 2017.

[69] Jean-Mistral, C., Basrour, S., and Chaillout, J.-J., "Dielectric polymer: Scavenging energy from human motion," *Proceedings of SPIE - The International Society for Optical Engineering*, vol. 6927, 2008.

[70] Kang, G., Kim, K.-S., and Kim, S., "Note: Analysis of the efficiency of a dielectric elastomer generator for energy harvesting," *Review of Scientific*

Instruments, vol. 82, no. 4, 2011.

[71] Waki, M., Chiba, S., Kombluh, R., Pelrine, R., and Kunihiko, U., "Electric power from artificial muscles," *OCEANS'08 MTS/IEEE Kobe-Techno-Ocean'08 - Voyage toward the Future, OTO'08*, 2008.

[72] Anderson, I., Ieropoulos, I., McKay, T., O'Brien, B., and Melhuish, C., "Power for robotic artificial muscles," *IEEE/ASME Transactions on Mechatronics*, vol. 16, no. 1, pp. 107–111, 2011.

[73] Hiscock, T., Warner, M., and Palffy-Muhoray, P., "Solar to electrical conversion via liquid crystal elastomers," *Journal of Applied Physics*, vol. 109, no. 10, 2011.

[74] Chiba, S., Waki, M., Kornbluh, R., and Pelrine, R., "Innovative power generators for energy harvesting using electroactive polymer artificial muscles," *Proceedings of SPIE - The International Society for Optical Engineering*, vol. 6927, 2008.

[75] Mannsfeld, S., Tee, B.-K., Stoltenberg, R., Chen, C.-H., Barman, S., Muir, B., Sokolov, A., Reese, C., and Bao, Z., "Highly sensitive flexible pressure sensors with microstructured rubber dielectric layers," *Nature Materials*, vol. 9, no. 10, pp. 859–864, 2010.

[76] Jung, K., Kim, K., and Choi, H., "A self-sensing dielectric elastomer actuator," *Sensors and Actuators, A: Physical*, vol. 143, no. 2, pp. 343–351, 2008.

[77] Plante, J.-S. and Dubowsky, S., "Large-scale failure modes of dielectric elastomer actuators," *International Journal of Solids and Structures*, vol. 43, no. 25-26, pp. 7727–7751, 2006.

[78] Liu, Y., Liu, L., Zhang, Z., Shi, L., and Leng, J., "Comment on "method to analyze electromechanical stability of dielectric elastomers" [appl. phys. lett. 91, 061921 (2007)]," *Applied Physics Letters*, vol. 93, no. 10, 2008.

[79] O'Dwyer, J., *The theory of Electrical Conduction and Breakdown in Solid Dielectrics*. Clarendon Press, 1973.

[80] Gerson, R. and Marshall, T., "Dielectric breakdown of porous ceramics," *Journal of Applied Physics*, vol. 30, no. 11, pp. 1650–1653, 1959.

[81] Pelrine, R., Kornbluh, R., Pei, Q., and Joseph, J., "High-speed electrically actuated elastomers with strain greater than 100%," *Science*, vol. 287, no. 5454, pp. 836–839, 2000.

[82] Kofod, G., Sommer-Larsen, P., Kornbluh, R., and Pelrine, R., "Actuation response of polyacrylate dielectric elastomers," *Journal of Intelligent Material Systems and Structures*, vol. 14, no. 12, pp. 787–793, 2003.

[83] Koh, S., Li, T., Zhou, J., Zhao, X., Hong, W., Zhu, J., and Suo, Z., "Mechanisms of large actuation strain in dielectric elastomers," *Journal of Polymer Science, Part B: Polymer Physics*, vol. 49, no. 7, pp. 504–515, 2011.

[84] Sommer-Larsen, P. and Larsen, A., "Materials for dielectric elastomer actuators," *Proceedings of SPIE - The International Society for Optical Engineering*, vol. 5385, pp. 68–77, 2004.

[85] James, H. and Guth, E., "Theory of the increase in rigidity of rubber during cure," *The Journal of Chemical Physics*, vol. 15, no. 9, pp. 669–683, 1947.

[86] Langley, N. and Ferry, J., "Dynamic mechanical properties of cross-linked rubbers. vi. poly(dimethylsiloxane) networks," *Macromolecules*, vol. 1, no. 4, pp. 353–358, 1968.

[87] Dossin, L. and Graessley, W., "Rubber elasticity of well-characterized polybutadiene networks," *Macromolecules*, vol. 12, no. 1, pp. 123–130, 1979.

[88] Carpi, F., De Rossi, D., Kornbluh, R., and Pelrine, R., *Dielectric elastomers as electromechanical transducers*, ch. Physical and chemical properties of dielectric elastomers. Elsevier Ltd, 2008.

[89] Frisch, H. and Klempner, D., "Advances in interpenetrating polymer networks," *Pure and Applied Chemistry*, vol. 53, no. 8, pp. 1557–1566, 1981.

[90] Hourston, D. and Schfer, F.-U., "Poly(ether urethane)/poly(ethyl methacrylate) interpenetrating polymer networks: Morphology, phase con-

tinuity and mechanical properties as a function of composition," *Polymer*, vol. 37, no. 16, pp. 3521–3530, 1996.

[91] Larsen, A., Sommer-Larsen, P., and Hassager, O., "Some experimental results for the end-linked polydimethylsiloxane network system," *E-Polymers*, 2004.

[92] Chambon, F. and Winter, H., "Linear viscoelasticity at the gel point of a crosslinking pdms with imbalanced stoichiometry," *Journal of Rheology*, vol. 31, no. 8, pp. 683–697, 1987.

[93] Larsen, A., Sommer-Larsen, P., and Hassager, O., "How to tune rubber elasticity," *Proceedings of SPIE - The International Society for Optical Engineering*, vol. 5385, pp. 108–117, 2004.

[94] Milner, S. and McLeish, T., "Parameter-free theory for stress relaxation in star polymer melts," *Macromolecules*, vol. 30, no. 7, pp. 2159–2166, 1997.

[95] De Gennes, P.-G., "Conjectures on the transport of a melt through a gel," *Macromolecules*, vol. 19, no. 4, pp. 1245–1249, 1986.

[96] Lu, T., Huang, J., Jordi, C., Kovacs, G., Huang, R., Clarke, D., and Suo, Z., "Dielectric elastomer actuators under equal-biaxial forces, uniaxial forces, and uniaxial constraint of stiff fibers," *Soft Matter*, vol. 8, no. 22, pp. 6167–6173, 2012.

[97] Mao, G., Li, T., Zou, Z., Qu, S., and Shi, M., "Prestretch effect on snap-through instability of short-length tubular elastomeric balloons under inflation," *International Journal of Solids and Structures*, vol. 51, no. 11-12, pp. 2109–2115, 2014.

[98] Zhao, X. and Suo, Z., "Method to analyze electromechanical stability of dielectric elastomers," *Applied Physics Letters*, vol. 91, no. 6, 2007.

[99] Zhao, X., Hong, W., and Suo, Z., "Electromechanical hysteresis and coexistent states in dielectric elastomers," *Physical Review B - Condensed Matter and Materials Physics*, vol. 76, no. 13, 2007.

[100] Li, T., Qu, S., Keplinger, C., Kaltseis, R., Baumgartner, R., Bauer, S., Suo, Z., and Yang, W., "Modeling guided design of dielectric elastomer generators and actuators," *Proceedings of SPIE - The International Society for Optical Engineering*, vol. 8340, 2012.

[101] Godaba, H., Foo, C., Zhang, Z., Khoo, B., and Zhu, J., "Giant voltage-induced deformation of a dielectric elastomer under a constant pressure," *Applied Physics Letters*, vol. 105, no. 11, 2014.

[102] Zhou, J., Jiang, L., and Khayat, R., "Viscoelastic effects on frequency tuning of a dielectric elastomer membrane resonator," *Journal of Applied Physics*, vol. 115, no. 12, 2014. cited By 13.

[103] Lochmatter, P., Kovacs, G., and Wissler, M., "Characterization of dielectric elastomer actuators based on a visco-hyperelastic film model," *Smart Materials and Structures*, vol. 16, no. 2, pp. 477–486, 2007.

[104] Huang, J., Shian, S., Suo, Z., and Clarke, D., "Maximizing the energy density of dielectric elastomer generators using equi-biaxial loading," *Advanced Functional Materials*, vol. 23, no. 40, pp. 5056–5061, 2013.

[105] Wang, Y., Xue, H., Chen, H., and Qiang, J., "A dynamic visco-hyperelastic model of dielectric elastomers and their energy dissipation characteristics," *Applied Physics A: Materials Science and Processing*, vol. 112, no. 2, pp. 339–347, 2013.

[106] Qu, S. and Suo, Z., "A finite element method for dielectric elastomer transducers," *Acta Mechanica Solida Sinica*, vol. 25, no. 5, pp. 459–466, 2012.

[107] Wang, Y., Chen, B., Bai, Y., Wang, H., and Zhou, J., "Actuating dielectric elastomers in pure shear deformation by elastomeric conductors," *Applied Physics Letters*, vol. 104, no. 6, 2014.

[108] Zhou, J., Jiang, L., and Khayat, R., "Failure analysis of a dielectric elastomer plate actuator considering boundary constraints," *Journal of Intelligent Material Systems and Structures*, vol. 24, no. 14, pp. 1667–1674, 2013.

[109] Huang, J., Lu, T., Zhu, J., Clarke, D., and Suo, Z., "Large, uni-directional actuation in dielectric elastomers achieved by fiber stiffening," *Applied Physics Letters*, vol. 100, no. 21, 2012.

[110] Keplinger, C., Li, T., Baumgartner, R., Suo, Z., and Bauer, S., "Harnessing snap-through instability in soft dielectrics to achieve giant voltage-triggered deformation," *Soft Matter*, vol. 8, no. 2, pp. 285–288, 2012.

[111] Li, T., Keplinger, C., Baumgartner, R., Bauer, S., Yang, W., and Suo, Z., "Giant voltage-induced deformation in dielectric elastomers near the verge of snap-through instability," *Journal of the Mechanics and Physics of Solids*, vol. 61, no. 2, pp. 611–628, 2013.

[112] Subramani, K., Cakmak, E., Spontak, R., and Ghosh, T., "Enhanced electroactive response of unidirectional elastomeric composites with high-dielectric-constant fibers," *Advanced Materials*, vol. 26, no. 18, pp. 2949–2953, 2014.

[113] Cakmak, E., Fang, X., Yildiz, O., Bradford, P., and Ghosh, T., "Carbon nanotube sheet electrodes for anisotropic actuation of dielectric elastomers," *Carbon*, vol. 89, pp. 113–120, 2015.

[114] Ogden, R., "Large deformation isotropic elasticity - on the correlation of theory and experiment for incompressible rubberlike solids," *Rubber Chemistry and Technology*, vol. 46, no. 2, pp. 398–416, 1973.

[115] Gent, A., "A new constitutive relation for rubber," *Rubber Chemistry and Technology*, vol. 69, no. 1, pp. 59–61, 1996.

[116] Mooney, M., "A theory of large elastic deformation," *Journal of Applied Physics*, vol. 11, no. 9, pp. 582–592, 1940.

[117] Lazopoulos, K. and Ogden, R., "Nonlinear elasticity theory with discontinuous internal variables," *Mathematics and Mechanics of Solids*, vol. 3, no. 1, pp. 29–51, 1998.

[118] Kofod, G., *Dielectric Elastomer Actuator*. PhD thesis, University of Denmark, 2001.

[119] Goulbourne, N., "A constitutive model of polyacrylate interpenetrating polymer networks for dielectric elastomers," *International Journal of Solids and Structures*, vol. 48, no. 7-8, pp. 1085–1091, 2011.

[120] Lv, X., Liu, L., Liu, Y., and Leng, J., "Dielectric elastomer energy harvesting: Maximal converted energy, viscoelastic dissipation and a wave power generator," *Smart Materials and Structures*, vol. 24, no. 11, 2015.

[121] Li, T., Qu, S., and Yang, W., "Energy harvesting of dielectric elastomer generators concerning inhomogeneous fields and viscoelastic deformation," *Journal of Applied Physics*, vol. 112, no. 3, 2012.

[122] Goulbourne, N., Mockensturm, E., and Frecker, M., "A nonlinear model for dielectric elastomer membranes," *Journal of Applied Mechanics, Transactions ASME*, vol. 72, no. 6, pp. 899–906, 2005.

[123] Zhou, J., Jiang, L., and Khayat, R., "Dynamic analysis of a tunable viscoelastic dielectric elastomer oscillator under external excitation," *Smart Materials and Structures*, vol. 25, no. 2, 2016.

[124] Zhu, J., Cai, S., and Suo, Z., "Resonant behavior of a membrane of a dielectric elastomer," *International Journal of Solids and Structures*, vol. 47, no. 24, pp. 3254–3262, 2010.

[125] Berselli, G., Vertechy, R., Babi, M., and Parenti Castelli, V., "Dynamic modeling and experimental evaluation of a constant-force dielectric elastomer actuator," *Journal of Intelligent Material Systems and Structures*, vol. 24, no. 6, pp. 779–791, 2013.

[126] Yang, E., Frecker, M., and Mockensturm, E., "Viscoelastic model of dielectric elastomer membranes," *Proceedings of SPIE - The International Society for Optical Engineering*, vol. 5759, pp. 82–93, 2005.

[127] Hong, W., "Modeling viscoelastic dielectrics," *Journal of the Mechanics and Physics of Solids*, vol. 59, no. 3, pp. 637–650, 2011.

[128] Chiang Foo, C., Cai, S., Jin Adrian Koh, S., Bauer, S., and Suo, Z., "Model of dissipative dielectric elastomers," *Journal of Applied Physics*, vol. 111,

no. 3, 2012.

[129] Hossain, M., Vu, D., and Steinmann, P., "Experimental study and numerical modelling of vhb 4910 polymer," *Computational Materials Science*, vol. 59, pp. 65–74, 2012.

[130] Arruda, E. and Boyce, M., "A three-dimensional constitutive model for the large stretch behavior of rubber elastic materials," *Journal of the Mechanics and Physics of Solids*, vol. 41, no. 2, pp. 389–412, 1993.

[131] Linder, C., Tkachuk, M., and Miehe, C., "A micromechanically motivated diffusion-based transient network model and its incorporation into finite rubber viscoelasticity," *Journal of the Mechanics and Physics of Solids*, vol. 59, no. 10, pp. 2134–2156, 2011.

[132] Wissler, M. and Mazza, E., "Mechanical behavior of an acrylic elastomer used in dielectric elastomer actuators," *Sensors and Actuators, A: Physical*, vol. 134, no. 2, pp. 494–504, 2007.

[133] Wang, S., Decker, M., Henann, D., and Chester, S., "Modeling of dielectric viscoelastomers with application to electromechanical instabilities," *Journal of the Mechanics and Physics of Solids*, vol. 95, pp. 213–229, 2016.

[134] Kornbluh, R., Pelrine, R., Joseph, J., Heydt, R., Pei, Q., and Chiba, S., "High-field electrostriction of elastomeric polymer dielectrics for actuation," *Proceedings of SPIE - The International Society for Optical Engineering*, vol. 3669, pp. 149–161, 1999.

[135] Sommer-Larsen, P., Hooker, J., Kofod, G., West, K., Benslimane, M., and Gravesen, P., "Response of dielectric elastomer actuators," *Proceedings of SPIE - The International Society for Optical Engineering*, vol. 4329, no. 1, pp. 157–163, 2001.

[136] Pei, Q., Rosenthal, M., Pelrine, R., Stanford, S., and Kornbluh, R., "Multifunctional electroelastomer roll actuators and their application for biomimetic walking robots," *Proceedings of SPIE - The International Society for Optical Engineering*, vol. 5051, pp. 281–290, 2003.

[137] Chen, A. and Bergbreiter, S., "A comparison of critical shear force in low-voltage, all-polymer electroadhesives to a basic friction model," *Smart Materials and Structures*, vol. 26, no. 2, 2017.

[138] Zhao, X., Hong, W., and Suo, Z., "Stretching and polarizing a dielectric gel immersed in a solvent," *International Journal of Solids and Structures*, vol. 45, no. 14-15, pp. 4021–4031, 2008.

[139] Zhou, J., Jiang, L., and Khayat, R., "Electromechanical response and failure modes of a dielectric elastomer tube actuator with boundary constraints," *Smart Materials and Structures*, vol. 23, no. 4, 2014.

[140] Koh, S., Keplinger, C., Li, T., Bauer, S., and Suo, Z., "Dielectric elastomer generators: How much energy can be converted?," *IEEE/ASME Transactions on Mechatronics*, vol. 16, no. 1, pp. 33–41, 2011.

[141] Liu, Y., Liu, L., Zhang, Z., Jiao, Y., Sun, S., and Leng, J., "Analysis and manufacture of an energy harvester based on a mooney-rivlin-type dielectric elastomer," *EPL*, vol. 90, no. 3, 2010.

[142] Sarbana, R., Oubaeka, J., and Jones, R., "Closed-loop control of a core free rolled eap actuator," *Proceedings of SPIE - The International Society for Optical Engineering*, vol. 7287, 2009.

[143] Sarban, R. and Jones, R., "Physical model-based internal model control of a de actuator," *Proceedings of SPIE - The International Society for Optical Engineering*, vol. 7976, 2011.

[144] Randazzo, M., Fumagalli, M., Metta, G., and Sandini, G., "Closed loop control of a rotational joint driven by two antagonistic dielectric elastomer actuators," *Proceedings of SPIE - The International Society for Optical Engineering*, vol. 7642, 2010.

[145] Kaal, W. and Herold, S., "Electroactive polymer actuators in dynamic applications," *IEEE/ASME Transactions on Mechatronics*, vol. 16, no. 1, pp. 24–32, 2011.

[146] Xie, S., Ramson, P., Graaf, D., Calius, E., and Anderson, I., "An adaptive control system for dielectric elastomers," *Proceedings of the IEEE International Conference on Industrial Technology*, vol. 2005, pp. 335–340, 2005.

[147] Babi, M., Vertechy, R., Berselli, G., Lenari, J., Parenti Castelli, V., and Vassura, G., "An electronic driver for improving the open and closed loop electro-mechanical response of dielectric elastomer actuators," *Mechatronics*, vol. 20, no. 2, pp. 201–212, 2010.

[148] Gisby, T., Calius, E., Xie, S., and Anderson, I., "An adaptive control method for dielectric elastomer devices," *Proceedings of SPIE - The International Society for Optical Engineering*, vol. 6927, 2008.

[149] Hodgins, M., Rizzello, G., York, A., Naso, D., and Seelecke, S., "A smart experimental technique for the optimization of dielectric elastomer actuator (dea) systems," *Smart Materials and Structures*, vol. 24, no. 9, 2015.

[150] Jones, R. and Sarban, R., "Model validation and feedback controller design for a dielectric elastomer actuator," *Journal of Intelligent Material Systems and Structures*, vol. 27, no. 15, pp. 2078–2090, 2016.

[151] Sarban, R. and Jones, R., "Physical model-based active vibration control using a dielectric elastomer actuator," *Journal of Intelligent Material Systems and Structures*, vol. 23, no. 4, pp. 473–483, 2012.

[152] Huu Chuc, N., Thuy, D., Park, J., Kim, D., Koo, J., Lee, Y., Nam, J.-D., and Choi, H., "A dielectric elastomer actuator with self-sensing capability," *Proceedings of SPIE - The International Society for Optical Engineering*, vol. 6927, 2008.

[153] Matysek, M., Haus, H., Moessinger, H., Brokken, D., Lotz, P., and Schlaak, H., "Combined driving and sensing circuitry for dielectric elastomer actuators in mobile applications," *Proceedings of SPIE - The International Society for Optical Engineering*, vol. 7976, 2011.

[154] Rizzello, G., Ferrante, F., Naso, D., and Seelecke, S., "Robust interaction control of a dielectric elastomer actuator with variable stiffness,"

IEEE/ASME Transactions on Mechatronics, vol. 22, no. 4, pp. 1705–1716, 2017.

[155] Rizzello, G., Naso, D., York, A., and Seelecke, S., "A self-sensing approach for dielectric elastomer actuators based on online estimation algorithms," *IEEE/ASME Transactions on Mechatronics*, vol. 22, no. 2, pp. 728–738, 2017.

[156] Hoffstadt, T. and Maas, J., "Self-sensing algorithms for dielectric elastomer multilayer stack-transducers," *IFAC-PapersOnLine*, vol. 49, no. 21, pp. 373–379, 2016.

[157] Ye, Z. and Chen, Z., "Self-sensing of dielectric elastomer actuator enhanced by artificial neural network," *Smart Materials and Structures*, vol. 26, no. 9, 2017.

[158] Rosset, S., O'Brien, B., Gisby, T., Xu, D., Shea, H., and Anderson, I., "Self-sensing dielectric elastomer actuators in closed-loop operation," *Smart Materials and Structures*, vol. 22, no. 10, 2013.

[159] Gisby, T., Xie, S., Calius, E., and Anderson, I., "Integrated sensing and actuation of muscle-like actuators," *Proceedings of SPIE - The International Society for Optical Engineering*, vol. 7287, 2009.

[160] Gisby, T., O'Brien, B., and Anderson, I., "How far and how hard: Tactile feedback for robotic manipulators," *Proceedings of SPIE - The International Society for Optical Engineering*, vol. 8340, 2012.

[161] Shintake, J., Rosset, S., Schubert, B., Floreano, D., and Shea, H., "Versatile soft grippers with intrinsic electroadhesion based on multifunctional polymer actuators," *Advanced Materials*, vol. 28, no. 2, pp. 231–238, 2016.

[162] Branz, F., Antonello, A., Carron, A., Carli, R., and Francesconi, A., "Kinematics and control of redundant robotic arm based on dielectric elastomer actuators," *Proceedings of SPIE - The International Society for Optical Engineering*, vol. 9430, no. January, 2015.

[163] Toth, L. and Goldenberg, A., "Control system design for a dielectric elastomer actuator: The sensory subsystem," *Proceedings of SPIE - The International Society for Optical Engineering*, vol. 4695, pp. 323–334, 2002.

[164] Kujawski, M., Pearse, J., and Smela, E., "Elastomers filled with exfoliated graphite as compliant electrodes," *Carbon*, vol. 48, no. 9, pp. 2409–2417, 2010.

[165] Rosset, S. and Shea, H., "Flexible and stretchable electrodes for dielectric elastomer actuators," *Applied Physics A: Materials Science and Processing*, vol. 110, no. 2, pp. 281–307, 2013.

[166] O'Brien, B., Thode, J., Anderson, I., Calius, E., Haemmerle, E., and Xie, S., "Integrated extension sensor based on resistance and voltage measurement for a dielectric elastomer," *Proceedings of SPIE - The International Society for Optical Engineering*, vol. 6524, 2007.

[167] Li, T., Zou, Z., Mao, G., and Qu, S., "Electromechanical bistable behavior of a novel dielectric elastomer actuator," *Journal of Applied Mechanics, Transactions ASME*, vol. 81, no. 4, 2014.

[168] Li, T., Li, C., Mao, G., Zou, Z., Xie, Y., and Qu, S., "Novel dielectric elastomer structures with electromechanical instability," *Proceedings of SPIE - The International Society for Optical Engineering*, vol. 9056, 2014.

[169] Li, T., Li, W., Zou, Z., Hong, Z., and Qu, S., "Effects of stretching rate and size on the rupture of acrylic dielectric elastomer," *International Journal of Applied Mechanics*, vol. 6, no. 3, 2014.

[170] Zou, Z., Li, T., Qu, S., and Yu, H., "Active shape control and phase coexistence of dielectric elastomer membrane with patterned electrodes," *Journal of Applied Mechanics, Transactions ASME*, vol. 81, no. 3, 2014.

[171] Li, T., Qu, S., and Yang, W., "Electromechanical and dynamic analyses of tunable dielectric elastomer resonator," *International Journal of Solids and Structures*, vol. 49, no. 26, pp. 3754–3761, 2012.

[172] Li, T., Qu, S., Li, Z., Tao, W., and Wang, M., "Investigation of the mechanical properties of the ni-p-cnts coated copper composite materials: Experiments and modeling," *Materials Science and Engineering A*, vol. 500, no. 1-2, pp. 182–187, 2009.

[173] Shepherd, R., Ilievski, F., Choi, W., Morin, S., Stokes, A., Mazzeo, A., Chen, X., Wang, M., and Whitesides, G., "Multigait soft robot," *Proceedings of the National Academy of Sciences of the United States of America*, vol. 108, no. 51, pp. 20400–20403, 2011.

[174] Morin, S., Shepherd, R., Kwok, S., Stokes, A., Nemiroski, A., and Whitesides, G., "Camouflage and display for soft machines," *Science*, vol. 337, no. 6096, pp. 828–832, 2012.

[175] Stokes, A., Shepherd, R., Morin, S., Ilievski, F., and Whitesides, G., "A hybrid combining hard and soft robots," *Soft Robotics*, vol. 1, no. 1, pp. 70–74, 2014.

[176] Martinez, R., Branch, J., Fish, C., Jin, L., Shepherd, R., Nunes, R., Suo, Z., and Whitesides, G., "Robotic tentacles with three-dimensional mobility based on flexible elastomers," *Advanced Materials*, vol. 25, no. 2, pp. 205–212, 2013.

[177] Lin, H.-T., Leisk, G., and Trimmer, B., "Goqbot: A caterpillar-inspired soft-bodied rolling robot," *Bioinspiration and Biomimetics*, vol. 6, no. 2, 2011.

[178] Ma, K., Chirarattananon, P., Fuller, S., and Wood, R., "Controlled flight of a biologically inspired, insect-scale robot," *Science*, vol. 340, no. 6132, pp. 603–607, 2013.

[179] Anderson, I., Gisby, T., McKay, T., O'Brien, B., and Calius, E., "Multi-functional dielectric elastomer artificial muscles for soft and smart machines," *Journal of Applied Physics*, vol. 112, no. 4, 2012.

[180] Anderson, I., Hale, T., Gisby, T., Inamura, T., McKay, T., O'Brien, B., Walbran, S., and Calius, E., "A thin membrane artificial muscle rotary

motor," *Applied Physics A: Materials Science and Processing*, vol. 98, no. 1, pp. 75–83, 2010.

[181] Brochu, P. and Pei, Q., "Advances in dielectric elastomers for actuators and artificial muscles," *Macromolecular Rapid Communications*, vol. 31, no. 1, pp. 10–36, 2010.

[182] Liu, L., Luo, X., Liu, Y., and Leng, J., "Dielectric elastomer energy harvesting undergoing polarization saturation," *Proceedings of SPIE - The International Society for Optical Engineering*, vol. 8340, 2012.

[183] Lucking Bigu, J., Chouinard, P., Proulx, S., Miron, G., and Plante, J., "Preliminary assessment of manufacturing impacts on dielectric elastomer actuators reliability," tech. rep., 2009.

[184] Yuan, W., Lam, T., and Pei, Q., "Durable dielectric elastomer actuators via self-clearable compliant electrode materials," *Materials Research Society Symposium Proceedings*, vol. 1129, pp. 183–190, 2009.

[185] Ahmadi, S., Gooyers, M., Soleimani, M., and Menon, C., "Fabrication and electromechanical examination of a spherical dielectric elastomer actuator," *Smart Materials and Structures*, vol. 22, no. 11, 2013.

[186] Heydt, R., Pelrine, R., Joseph, J., Eckerle, J., and Kornbluh, R., "Acoustical performance of an electrostrictive polymer film loudspeaker," *Journal of the Acoustical Society of America*, vol. 107, no. 2, pp. 833–839, 2000.

[187] Carpi, F. and Gei, M., "Predictive stress-stretch models of elastomers up to the characteristic flex," *Smart Materials and Structures*, vol. 22, no. 10, 2013.

[188] Hackl, C., Tang, H.-Y., Lorenz, R., Turng, L.-S., and Schrder, D., "A multidomain model of planar electro-active polymer actuators," *IEEE Transactions on Industry Applications*, vol. 41, no. 5, pp. 1142–1148, 2005.

[189] Zhang, J., Wang, Y., McCoul, D., Pei, Q., and Chen, H., "Viscoelastic creep elimination in dielectric elastomer actuation by preprogrammed voltage," *Applied Physics Letters*, vol. 105, no. 21, 2014.

[190] Schroeder, M., "Synthesis of low-peak-factor signals and binary sequences with low autocorrelation," *IEEE Transactions on Information Theory*, vol. 16, no. 1, pp. 85–89, 1970.

[191] Choi, H., Jung, K., Kwak, J., Lee, S., Kim, H., Jeon, J., and Nam, J., "Multiple degree-of-freedom digital soft actuator for robotic applications," *Proceedings of SPIE - The International Society for Optical Engineering*, vol. 5051, pp. 262–271, 2003.

[192] Bar-Cohen, Y., "Biomimetic actuators using electroactive polymers (eap) as artificial muscles," *International SAMPE Symposium and Exhibition (Proceedings)*, vol. 51, 2006.

[193] Jung, K., Nam, J., Lee, Y., and Choi, H., "Micro inchworm robot actuated by artificial muscle actuator based on non-prestrained dielectric elastomer," *Proceedings of SPIE - The International Society for Optical Engineering*, vol. 5385, pp. 357–367, 2004.

[194] Pelrine, R., Kornbluh, R., Pei, Q., Stanford, S., Oh, S., Eckerle, J., Full, R., Rosentha, M., and Meijer, K., "Dielectric elastomer artificial muscle actuators: Toward biomimetic motion," *Proceedings of SPIE-The International Society for Optical Engineering*, vol. 4695, pp. 126–137, 2002.

[195] Jordi, C., Michel, S., Kovacs, G., and Ermanni, P., "Scaling of planar dielectric elastomer actuators in an agonist-antagonist configuration," *Sensors and Actuators, A: Physical*, vol. 161, no. 1-2, pp. 182–190, 2010.

[196] Hoffstadt, T., Griese, M., and Maas, J., "Online identification algorithms for integrated dielectric electroactive polymer sensors and self-sensing concepts," *Smart Materials and Structures*, vol. 23, no. 10, 2014.

[197] Gisby, T., *Smart artificial muscles*. PhD thesis, The University of Auckland, 2011.

[198] Carpi, F., Anderson, I., Bauer, S., Frediani, G., Gallone, G., Gei, M., Graaf, C., Jean-Mistral, C., Kaal, W., Kofod, G., Kollosche, M., Kornbluh, R., Lassen, B., Matysek, M., Michel, S., Nowak, S., O'Brien, B., Pei, Q., Pelrine, R., Rechenbach, B., Rosset, S., and Shea, H., "Standards for di-

electric elastomer transducers," *Smart Materials and Structures*, vol. 24, no. 10, 2015.

[199] Li, C., Xie, Y., Li, G., Yang, X., Jin, Y., and Li, T., "Electromechanical behavior of fiber-reinforced dielectric elastomer membrane," *International Journal of Smart and Nano Materials*, vol. 6, no. 2, pp. 124–134, 2015.